FATIGUE CRACK INITIATION IN RAIL STEELS

by

Sterling St. Lawrence

A thesis presented to the
University of Manitoba
in partial fulfilment of the
requirements for the degree of
Master of Science
in
Mechanical Engineering

Metallurgical Science Laboratories
Winnipeg, Manitoba
1992

ISBN 0-315-77865-2

Canada

FATIGUE CRACK INITIATION

IN RAIL STEELS

BY

STERLING ST. LAWRENCE

A Thesis submitted to the Faculty of Graduate Studies of the University of Manitoba in partial fulfillment of the requirements for the degree of

MASTER OF SCIENCE

ABSTRACT

The effect of nonmetallic inclusions in accelerating the initiation of fatigue cracks in rail steels was studied. Specimens were machined from the rail heads transverse to the rolling direction. The specimens were tested in the as received condition and in a condition with a shot peened surface. The shot peening was done to duplicate the cold working of the rail which occurs during service. The specimens were fatigued in a four point bending configuration using two different loading programs until crack initiation occurred. Crack initiation was detected using acoustic emission techniques. Following mechanical testing, the specimens were examined using optical and scanning electron microscopy to determine the crack initiation mechanism.

The fatigue performance of each steel was determined by the nature of the elongated inclusions. The crack initiation mechanism was found to be a function of these inclusions. Differences in the initiation mechanism determined the fatigue resistance of each steel. Three different crack initiation mechanisms were observed. The presence of brittle, easily damaged, inclusions was most detrimental to the fatigue performance of the rails. Inclusions which were ductile and resisted becoming fatigue damaged were less harmful. The cohesive strength between the matrix and the inclusion also determined the fatigue performance of the steels. Elongated inclusions that were ductile and had a strong cohesive strength were the least damaging to the fatigue performance.

The microstructural influence on the fatigue performance of the steels was minimal. Of far greater importance were differences in the elongated inclusions. A head hardened steel with the finest pearlitic microstructure had the poorest fatigue performance because of the brittle inclusions present. By contrast the steel with the coarsest pearlitic microstructure and the largest inclusion content had the best overall fatigue performance. The inclusions in this steel resisted becoming fatigue damaged due to their ductility and high cohesive strength.

After shot peening the fatigue performance of all the steels is closely matched, except for the head hardened rail. At high stress levels close to the yield strength the beneficial effect of shop peening was not evident, the greatest increase in the fatigue performance occurs at low stress levels close to the endurance limit.

The acoustic emission technique proved to be extremely sensitive to crack initiation. Cracks were detected at the earliest stages. Therefore, the influence of the inclusions were quantified in the metallographic investigation.

This study has provided a greater understanding of the role of nonmetallic inclusions in initiation fatigue cracks in steels.

ACKNOWLEDGEMENTS

The author would like to thank Dr. M.N. Bassim for the suggestion of this thesis topic and for his supervision and encouragement throughout the course of the research work.

A special thank you to Dr. C.D. Liu for all his suggestions and assistance. Thank you to Ray Hartle and Lincoln Oree for all their technical assistance and thanks to Canadian National Railways for suppling the materials and for their financial support.

TABLE OF CONTENTS

LIST OF TABLES

LIST OF FIGURES

Figures page#

Chapter I

Introduction

The life of a rail is effected by one or a combination of the following mechanisms: wear and contact fatigue of the outer surface layers or deeper subsurface fatigue failures. Wear and contact fatigue compete to damage the surface and immediate subsurface layers. Fatigue failures which include deep shells, transverse and detail fractures, affect deeper sections of the rail head.

Lubricating the rail head has reduced conventional adhesion wear of the rail surface. As the wear rate recedes beyond a certain value, the fatigue limit of the surface layer is reached before it can be worn away. Fatigue cracks will appear on the contact surface and within the immediate surface layers. Unlike the deeper subsurface fatigue cracks which propagate by a tensile stress field (mode I) the surface cracks are a result of contact fatigue and propagate by shear stress (mode II).

In the immediate surface layers the rail attempts to accommodate the wheel's overload stresses by extensive plastic deformation. A crack surface within this zone of plastic deformation is subjected to a biaxial stress field mode of two main components; a compressive stress perpendicular to the crack surface and a shear stress component parallel to the plane of the crack surface. The second component acts as the driving force for the cyclic crack growth and is thus predominantly mode II in character.

Fatigue cracks in the contact zone can be initiated by two different mechanisms. Cracks initiate as a result of ductility exhaustion of the immediate surface layer due to the incremental accumulation of surface plastic deformation or as a result of interactions between repetitive contact stresses and inclusions. The plastic deformation capability of rail steel or any other material is limited by the presence of inclusions in the shear zone. However, there has been no systematic study to relate the inclusion morphology within a

steel to the crack initiation mechanism operating during compressive-shear deformation or during simple tension-tension deformation.

Although the influence of non-metallic inclusions in initiating fatigue failures in steels has received considerable attention there has been no quantitative investigation to relate the specifics of the inclusion's morphology to the fatigue performance of rail steels. Such a study should characterize all the parameters of the inclusions, including their composition, the size and shape of the inclusions, the inclusion density within the steel and the inter-inclusion spacing.

The objective of this thesis is therefore to correlate the inclusion morphology to the fatigue performance of a variety of rail steels. The investigation is concerned with the inclusions influence on the fatigue resistance of steels in both the received condition and in a condition with a prior designated level of cold working. To cold work the steel the fatigue specimens are subjected to a uniform shot blast. This is done to better understand the interactive effects of cold work that is naturally induced in the rail during service, on the crack initiation process.

Due to the inherent complexities of a true compression-shear deformation system the specimens are tested in a simpler tension-tension four point bending configuration. The general overloading response of rail surfaces to wheels is to compression shear deform the rail steel perpendicular to the rail direction. As well, most early fatigue cracks in rail surfaces are aligned in the direction of the rail. Therefore, the tension direction of the fatigue specimens is horizontal and perpendicular to the rail direction. With this orientation the specimens are transverse to the rail direction and the elongated inclusions.

In order to relate the inclusion morphology to the fatigue performance of each rail steel tested, the inclusion parameters must be quantified prior to fatigue testing. All the components that characterize the inclusion are measured. This includes their composition, the inclusion dispersion and the size and shape of the inclusions.

To characterize the fatigue behaviour of each rail steel tested two different fatigue loading programs are used. For the initial fatigue testing program the stress level is increased in a stepped pattern after a specific increment of cycles. Cycling is continued and the stress level is increased until an active fatigue crack is detected within the specimen. This testing program is designed to evaluate the fatigue performance of each rail steel quickly and to provide a rapid comparison technique. To more fully characterize the fatigue performance of the steels samples are also cyclically loaded at a constant mean stress level until crack initiation occurs or until the fatigue limit is reached. A range of mean stress levels are used.

Crack initiation is detected by monitoring the acoustic emission activity occurring within the specimen during cyclic loading. Acoustic emission parameters have been used to characterize crack growth during fatigue testing. This technique has been used effectively to detect the onset of crack initiation.

For these experiments the acoustic emission system must only detect crack initiation. To locate the source of the fatigue crack and to determine the crack initiation mechanism the specimens are examined using both optical and scanning electron microscopy. It is hoped that the acoustic emission technique will capture crack initiation in the earliest stages of development. Therefore, the details of the crack initiation site and the initiation mechanism will be revealed and the precise role of the inclusions determined.

Chapter II

LITERATURE REVIEW

2.1 Introduction

To improve the fatigue performance of rail and thereby reduce the frequency of failures there have been a variety of studies to characterize the causes and mechanisms of fatigue failure of rail. Due to the complexities of the problem there has been no single investigation that can address all of the causes of crack initiation and subsequent rail failure. The range of variables that effect the fatigue performance of rails include variations in the microstructure of the rail, the complexities of the loading condition and changes in the operating circumstances. As well, the selection of a rail steel cannot be based solely on the materials fatigue resistance. The rail must also display an acceptable resistance to wear and have suitable strength and flow properties. Often the metallurgical factors that affect these different mechanical properties compete so the selection of the rail material is based on compromises in order to obtain a steel with the best overall performance.

The objective of this review is to examine certain aspects of the fatigue failure of rail. Specifically the role of non-metallic inclusions in initiating fatigue cracks in rail steels. Before discussing the specific role of inclusions the general loading condition of the rail and the resulting fatigue failure mechanisms are described. There is also a discussion of the effects of inclusions in initiating fatigue cracks in steels in general. Last of all a brief overview of the application of monitoring acoustic emission to detect crack initiation is presented. Special attention is given to its application to steel structures due to its significance in the present work.

2.2 Fatigue of Metals

The purpose of this section is to define some fundamentals of the fatigue of metals. That is, to introduce and describe certain aspects of the fatigue failure mechanisms which pertain to this specific investigation.

Fatigue is defined as the failure of a material that is subjected to a repeated or fluctuating stress at a level much below the tensile strength of the material. Therefore, fatigue failures occur during dynamic loading. The cyclic stresses, resulting from the dynamic loading, cause the formation of cracks which propagate and eventually lead to failure. The point of crack initiation is usually at a local stress concentrator resulting from section changes and notches or metallurgical stress concentrators such as inclusions.

Three conditions must be present to cause fatigue failure [1]. They are: (1) a maximum tensile stress of sufficiently high value; (2) a large enough variation or fluctuation in the applied stress and (3) a sufficiently large number of cycles of the applied stress. In addition, there is a variety of other factors that contribute to the fatigue failure process. They include the presence of stress concentrators, environmental considerations such as the presence of a corrosive atmosphere and the temperature, the material's metallurgical structure, the presence of residual stresses and the complexity of the applied stresses. All of these factors influence the fatigue process.

The development of a fatigue crack and its subsequent propagation can be divided into three stages. The earliest stage involves crack initiation and deepening on planes of high shear stress. The next stage involves the growth of a well defined crack in a direction normal to the maximum tensile stress. The final stage is characterized by rapid crack growth and the eventual rupture of the structure.

The position of crack initiation is at some point where the local stresses exceed the local strength. Stress concentrators, such as notches or inclusions raise the local stress level above the material's strength and thereby form sites for crack initiation. A model for crack initiation based on slip band intrusions and extrusions has been proposed by Wood [2]. If the alternating stress amplitude is sufficiently high slip bands are formed by the systematic buildup of fine slip movements. These lead to slip steps on a free surface, intrusions, extrusions, hills, valleys, ridges or groves which in turn lead to initiation of small

mircocracks [3]. The Stage I crack propagates along the persistent slip bands at an extremely low rate, generally on the order of angstroms per cycle.

During stage II the direction of the crack changes from parallel to the shear stress direction to a perpendicular direction. The stage II crack propagation process is by crack blunting. Under a tensile load notches form at the ends of the crack tip which concentrate the slip along planes at 45^{o} to the plane of the crack. As the crack grows by plastic shearing its tip becomes blunter. When the tension load is reduced or possibly reversed the slip direction in the end notches is also reduced or reversed. If the tensile load becomes compressive the crack faces will be crushed together and the new crack surface will then be sharpened to form a new crack tip and the whole process is repeated again during the next stress cycle.

During stage II crack propagation the crack growth rate, da/dN can be related to the stress intensity factor range, ΔK, by an essentially linear relationship

$$da/dN = a(\Delta K)^{P} \qquad (2.1)$$

where:

N - is the number of cycles and

2a - is the crack length.

This is the Paris' law. The values for P and A maybe determined from a plot of crack growth versus the stress intensity factor, as shown in Figure 2.1. The value of P is the linear portion of the curve and A is found by extending the straight line to $\Delta K = 1$ MPa $(m)^{1/2}$. Figure 2.1 also shows the characteristic threshold stress intensity factor, below which the crack will not propagate.

Stage III is characterized by accelerated crack growth leading to final rupture. During this stage the crack has grown to a size at which it significantly reduces the load-carrying capacity of the specimen.

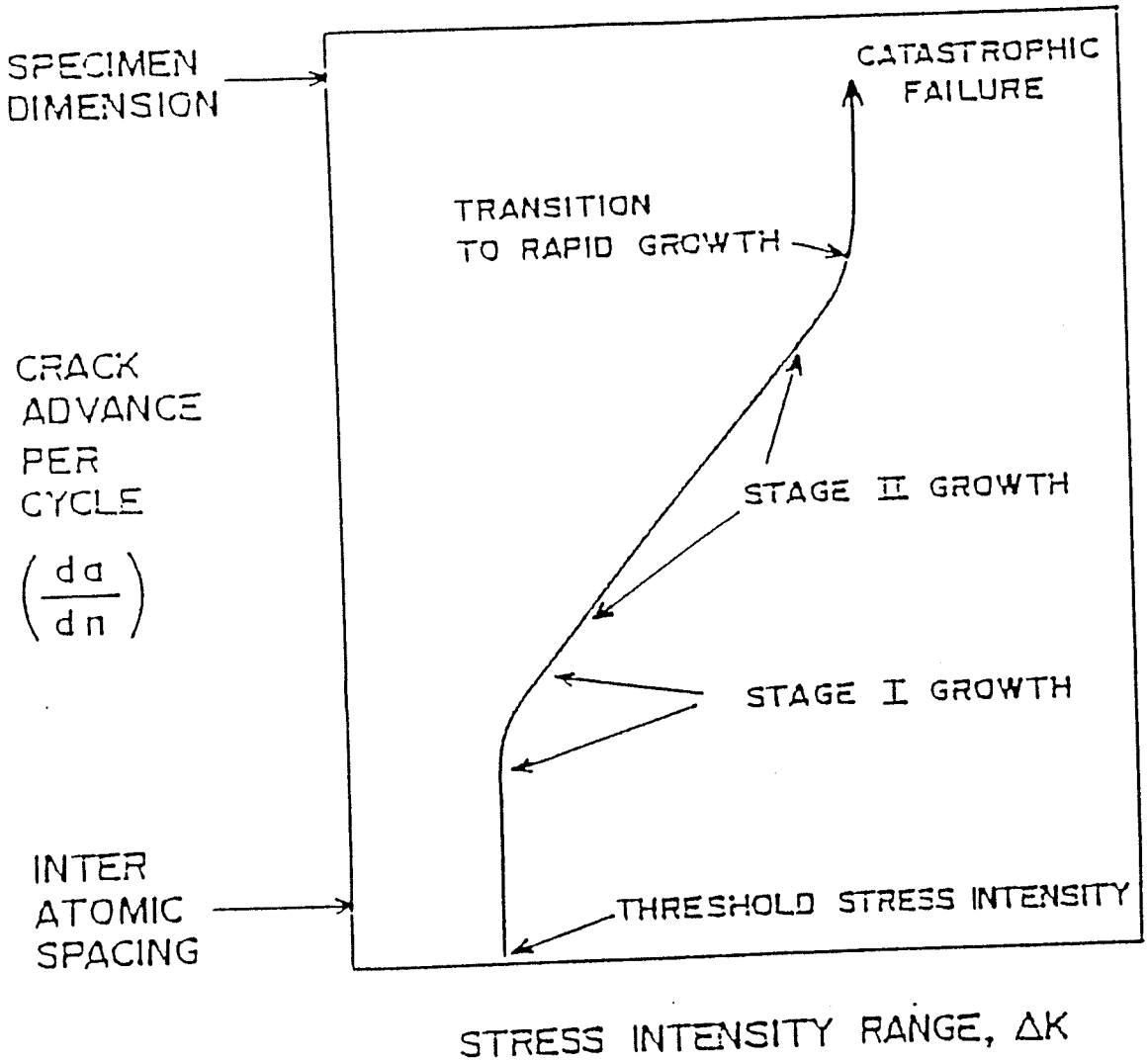

Figure 2.1. Schematic representation of crack-growth rate as a function of stress-intensity range.

2.3 Fatigue of Pearlitic Steels

The purpose of this section is to discuss the influence of the microstructure on both the initiation and propagation of fatigue cracks. The discussion is primarily limited to fully pearlitic structures because all the steels tested in this investigation have this structure.

Fatigue cracks have been observed to initiate along slip bands, at grain boundaries, at second phase particles and at inclusion-second phase interfaces [5]. The initiation site depends upon which occurs most easily. However, the inclusion content has an overriding effect which obscures the effect of other metallurgical variables [6]. The effect of inclusions in initiating fatigue cracks is described in a latter section of this review. The purpose of this section is to discuss the unique influence of the pearlite's lamellar microstructure in the initiation and propagation of fatigue cracks.

The influence of interlamellar spacing, pearlite colony size and prior austenite grain size on fatigue crack initiation has been investigated by Gray et. al. [5]. The results conclude that the interlamellar spacing has a controlling influence of the fatigue performance of pearlitic steels. The interlamellar spacing was observed to influence both the endurance limit and the number of cycles to failure at higher stresses. A finer spacing results in an improvement to the steel's fatigue crack resistance because the ferrite-cementite boundary is the dominant obstacle to dislocation motion. Colony and grain boundaries also present obstacles to dislocation motion but their influence is thought to be minimal in comparison.

During cyclic plastic deformation dislocations that are formed can either escape to a free surface or pile up against obstacles. The mechanism which causes dislocation pile ups and eventually slip band formation depends on the slip length. A smaller mean free slip path results in a reduction in the amount of local plastic strain which inhibits the formation of short stage I cracks. By reducing the interlamellar spacing the possibility of cracking the brittle cementite layers is reduced because of a reduction in the stress concentration of the slip bands. This explanation of the influence of interlamellar spacing on the fatigue

resistance is in agreement with the theory of crack initiation which requires a stress buildup at the ferrite-cementite interface which is large enough to cleave the cementite plate [6].

The influence of the microstructure on the fatigue crack propagation (FCP) rate was also investigated by Gray et. al. [7], who were able to make the following conclusions. The controlling microstructure influence on the FCP rate is the pearlite colony size and orientation. There is also a small but real effect due to the interlamellar spacing and an appreciable influence due to the prior austenite grain size. The influence of the microstructure on the FCP rate is thought to be due to a combination of the following interrelated events: (1) The ease with which the cementite is cracked; (2) the colony orientation and (3) slip reversibility and cyclic work hardening of the ferrite.

The effect of the colony orientation on FCP rate is caused by a variation in their effective yield strengths. The yield strength depends on whether the crack must propagate by fracturing the cementite lamellar or propagate by passing through the interlamellar ferrite. The ease with which a crack will propagate through the pearlite depends on its work hardening rate. A lower work hardening rate in a coarser pearlite would allow for more slip reversibility which in turn retards crack advancement. However, it has been determined that the work hardening behaviour of pearlite is largely determined by the dislocation density in ferrite and is independent of the interlamellar spacing. Most pearlitic steels cyclically soften at lower strains and cyclically harden at higher strains [8].

The differing microstructural requirements of initiation and propagation resistance in pearlitic structures presents a conflict in the steel's overall fatigue resistance. The eventual microstructural design will be dictated by the relative importance of crack initiation and propagation. Due to their overall brittleness fatigue crack propagation seems inevitable in high strength steels. Therefore, to improve their overall fatigue resistance it seems best to design against crack initiation.

2.4 The Influence of Inclusions in Initiating Fatigue Cracks

2.4.1 Introduction

The importance of inclusions on the fatigue performance of metals has received considerable attention over the past forty years [9-21]. The complexity of the problem hinders the development of a reliable quantitative treatment which may be used to access their influence. The factors which govern the relationship include the inclusions shape and size, their physical and chemical properties and their distribution and orientation with respect to the applied stress [9]. The influence of the inclusions in affecting the fatigue performance of a material is also dependent on the material's ultimate strength [10,11] and microstructure [12]. The purpose of this section is to discuss the role of inclusions in initiating fatigue cracks.

2.4.2 Stress Raising Influence of Inclusions

Many early studies were conducted to directly relate the steel's cleanliness and fatigue performance [13,14]. However, the results have been inconclusive. In an attempt to improve the inclusion evaluation techniques, Atkinson [9] introduced the Fairey inclusion counts, which takes into account the size, shape and corresponding stress-concentration factor of the nonmetallic inclusions. This technique treats the inclusion as a cavity and the stress concentration in the surrounding matrix may be evaluated solely on the cavities shape and size. Atkinson was able to correlate the Fairey inclusion count number to the endurance ratio for a variety of differing high strength steels. Another result of this investigation was the observation of an inclusion of critical size which causes crack initiation.

The importance of the inclusion size, and the existence of a minimum diameter of length below which the inclusions are not effective stress raisers have been demonstrated by Uhrus [14] for ball bearings, shown in Figure 2. This figure shows that only oxide

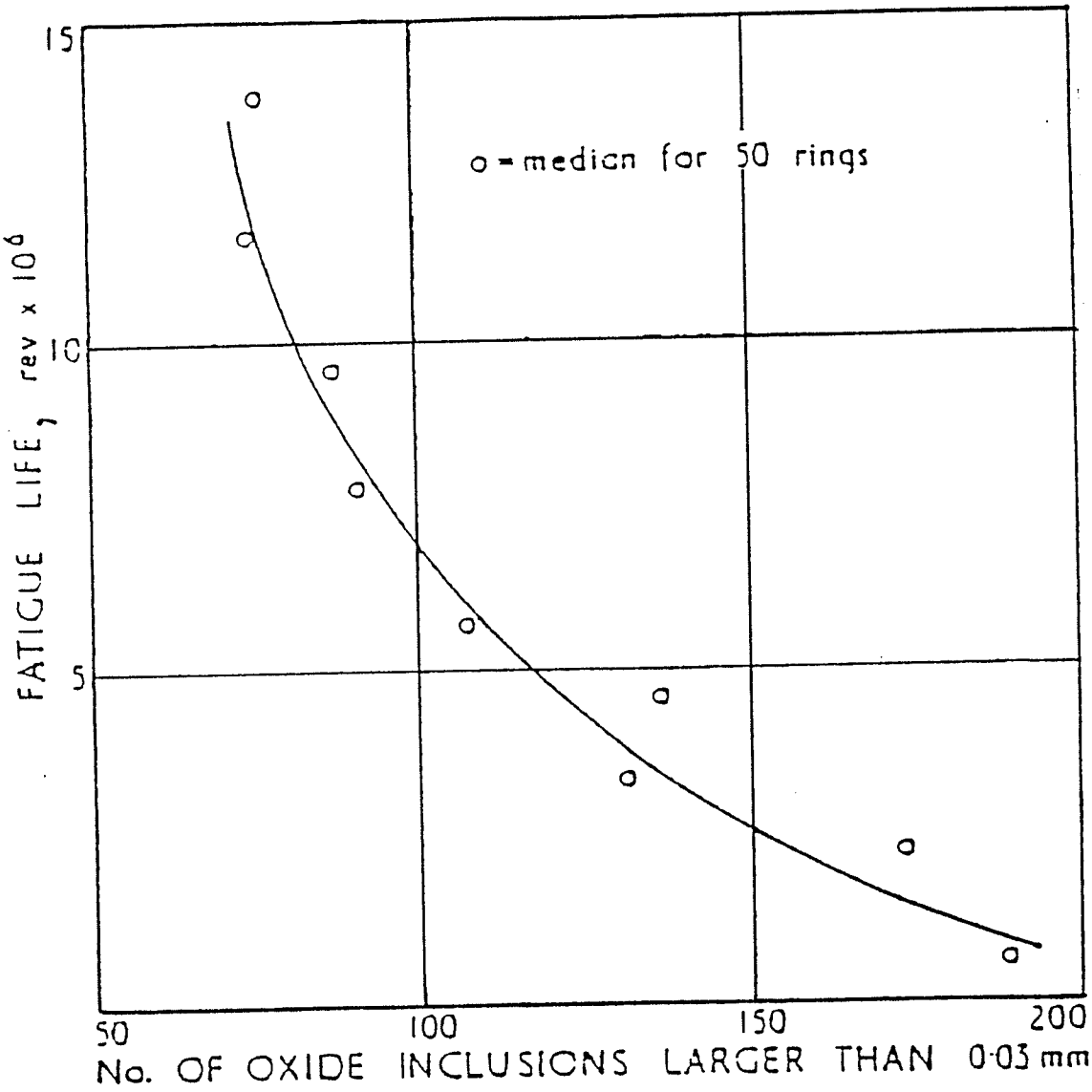

Figure 2.2. Effect of oxide inclusions on the flaking of rig-tested bearings; 1309 outer rings.

inclusions above 30μm in diameter need to be considered. Similar observations were also reported by Duckworth and Ineson [15] and by DeKazinczy [16].

Cummings et. al. [11] were able to indirectly relate the size of the inclusions to the steels fatigue life. The elimination of large inclusions should greatly increase the fatigue life at low over stress conditions, but the life for high over stress would be improved little. At high stresses more and smaller inclusions become sites for crack initiation.

The work of Ineson et. al. [13] shows a reduction in the fatigue endurance limit with increasing ultimate tensile strength for a material with the same inclusion content. Thorton [17] also observed an increase in the notch effect of inclusions as the matrix's tensile strength increases. Ineson's work suggests that there exists a minimum tensile strength below which the inclusions will not be effective crack initiators. Other investigators have also considered the existence of a critical tensile strength [10,11,15].

In addition to the importance of the size of the inclusions, their orientation with respect to the applied stress is also an important influence on the fatigue performance of the steel [17,18]. From an investigation of two commercial heats of 4340 steels, Ransom [18] discovered that elongated inclusions would initiate cracks whenever the long axis of the inclusions was parallel to a direction of maximum shear stress or perpendicular to a direction of principal tensile stress.

The principal effect of inclusions is to increase stress magnitude in local areas of stress concentration and to alter the uniaxiality of the stress field [19]. The resulting stress concentration factor depend on the shape and orientation of the inclusion, the adhesion of the inclusion to the matrix and on the relative elastic constraints of the inclusion and the matrix. A theoretical analysis for the stress field around two dimensional inclusions of arbitrary elliptical shapes has been derived by Donnell [20]. Stress concentrations around three dimensional spherical and cylindrical inclusions have been determined by Edwards [21] and Goodier [22].

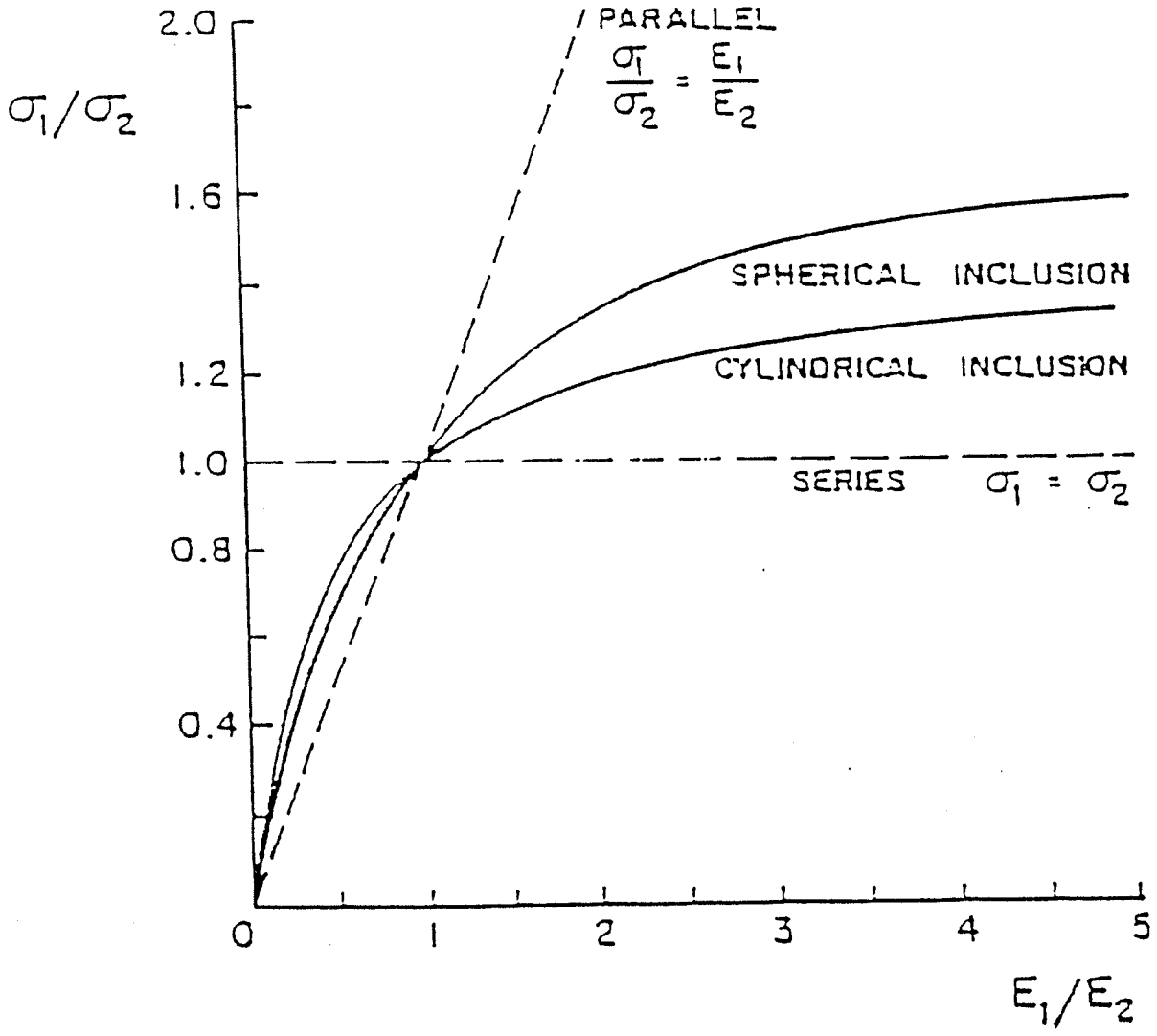

Figure 2.3 Stress concentration at inclusion in infinite body subjected to uniaxial tension at infinity [21].

A comparison of the stress concentration around three dimensional inclusions as a function of the inclusion plasticity relative to the matrix is shown in Figure 2.3. The subscripts 1 and 2 refer to the inclusion and the matrix respectively. The maximum stress concentration occurs at a spherical inclusion which is perfectly rigid, ie. $E_1/E_2 = \infty$. Unfortunately, this analysis is for inclusions which are completely bonded to the matrix. However, adhesion of the inclusion to the matrix is usually not perfect and often there are gaps [10]. The gaps may be considered intrinsic cracks in the material and therefore the stress concentration factors are useless in this case.

The magnitude and location of the maximum stresses are determined by the shape of the inclusion and by the ratio of the elastic modulus of the two materials. For example, the stress concentration factor for a rigid circular inclusion gives an intensified tensile stress at the polar points on the inclusion/matrix boundary [23]. This may explain the debonding observed at the poles of rigid spherical inclusions [24]. However, a common misunderstanding is to assume the stress concentration factor is less than unity when the inclusion and matrix have perfect adhesion [25]. This is correct at the end of the principal axis of an elongated inclusion which is perpendicular to the loading direction but at the pole in the loading direction the stress concentration factor is greater than unity and a fatigue crack could initiate here.

A shortcoming of using stress concentration factors to estimate the fatigue strength of steels is their lack of sensitivity. Murakami et. al.[25] performed a series of fatigue tests on specimens with artificial stress raisers, specifically small holes of differing sizes. Because the holes were so small and geometrically similar the stress concentration factors are essentially equal. However, there results clearly indicate that the fatigue life depends on the hole size, see Figure 2.4. This demonstrates a shortcoming of using the stress intensity factor alone to predict the fatigue strength of steels.

Another problem with the stress concentration factor analysis is that it is derived using perfectly spherical and elliptical forms for the inclusions. Any slight variation in the

inclusions shape or any small protrusions should greatly affect the inclusions actual stress concentration factor. However, the calculated values based on a rigid form will not reflect these variations in shape, and should only be considered as estimates.

2.4.3 Fatigue Crack Initiation Mechanisms

The crack initiation mechanism and the correlated nucleation site depend on the stress concentration resulting from the nonmetallic inclusions present in the steel. The crack will nucleate at a region of high stress concentration and relatively low plasticity. This can be either within the inclusion, at the interface or within the matrix near the inclusion [19]. The nucleation site will be determined by a combination of mechanical and chemical factors. The mechanical factors provide the required stress concentration and triaxiality and the chemical contributions are due to the cohesive strength of the inclusion/matrix interface.

In addition to the specific influences due to the nature of the inclusion the crack initiation mechanism also depends on the loading condition. Specifically, the presence or absence of plastic zones resulting from the cyclic loading, which depends on the magnitude of the applied stress, on the matrix strength and on the plasticity of the inclusion relative to the matrix.

The different loading conditions can be described as either low cycle fatigue ($n<10^4$ cycles), high cycle fatigue ($n>10^6$ cycles) or as intermediate fatigue ($10^4<n<10^6$ cycles), where n is the fatigue life of the specimen under consideration, ie. the number of cycles to crack initiation or failure.

Low cycle fatigue is characterized by relatively high stresses and a corresponding low number of cycles to failure. The specimen or structure is subjected to large cyclic plastic deformation which leads to the formation of intense slip bands. These slip bands intersect with obstacles such as nonmetallic inclusions to produce fatigue crack nuclei [26].

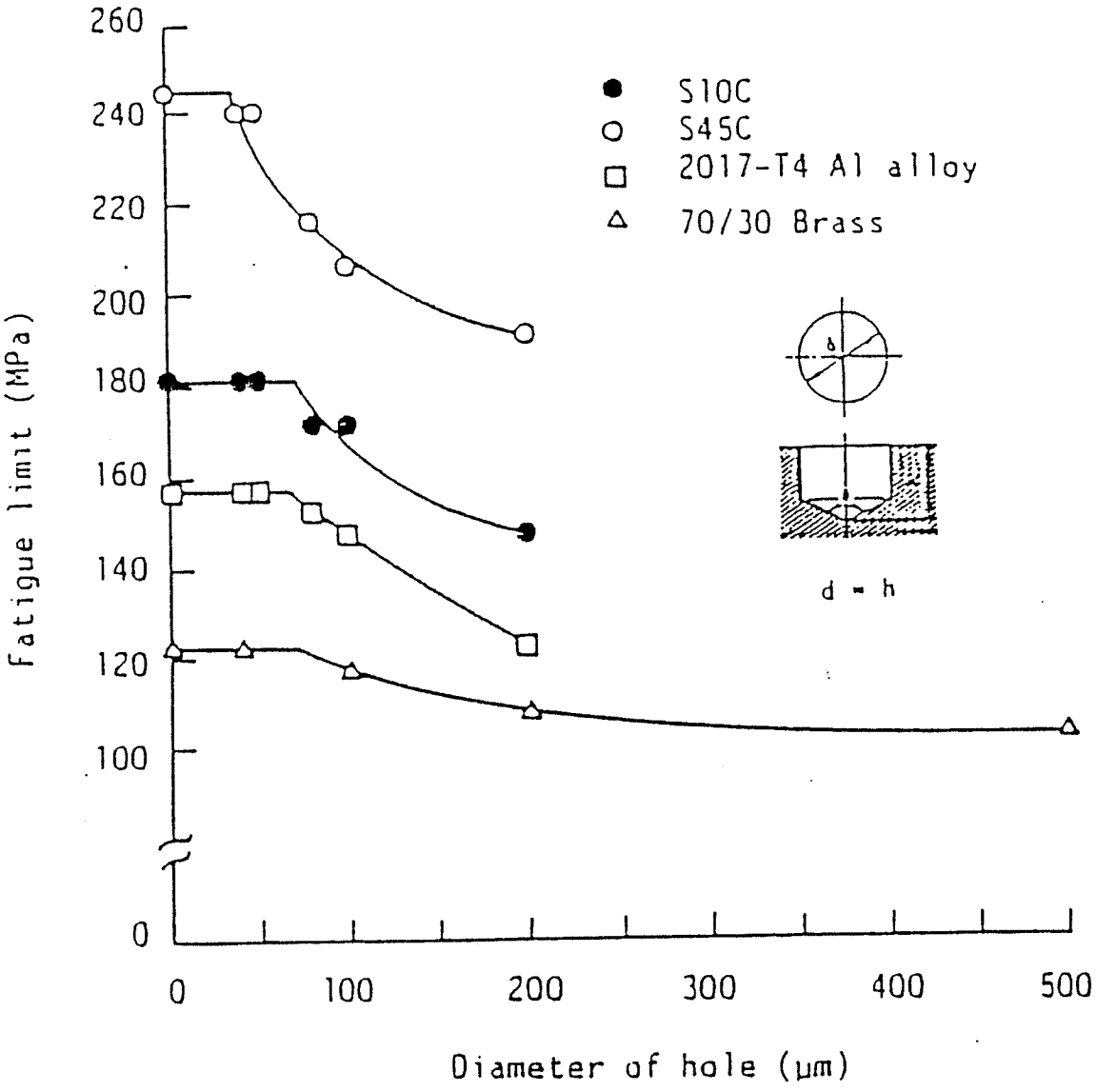

Figure 2.4. Effect of a small drilled hole on fatigue strength[25].

In the intermediate range (10^4<n<10^6) the crack nucleation mechanism changes from the lower end of the range to the upper end. At the lower end (10^4-10^5) crack nucleation occurs by plastically induced surface discontinuities. At the upper end of the intermediate range crack nucleation occurs by local cyclic-plastic strains which are confined to small regions of local stress concentration at inclusions [27]. With the latter conditions debonding at the inclusion/matrix interface appears to be the principal mechanism leading to the nucleation of fatigue cracks [24,28].

The influence of debonding at the inclusion/matrix interface has been investigated by Lankford [24]. Although, debonding at the inclusion/matrix interface is not the cause of crack nucleation it must be present if a short stage I crack is to propagate to form a stable stage II fatigue crack. Surprisingly the actual crack initiation site occurs several microns from the inclusion. The separation of the crack initiation site from the inclusion maybe caused by the compressive stresses at the inclusion boundary which hinders yielding. Lankford's investigation involves two differing strengths of 4340 steels. In the samples with a higher strength the crack nucleation is by a point intrusion/extrusion mechanism. A microcrack is formed when the pores or point intrusions coalesce. Crack nucleation for the more ductile steel is accompanied by extensive surface slip which indicates earlier plastic zone development about the inclusions. Regardless of the mode of initiation Lankford concludes that the crack must be associated with a debonded inclusion to propagate and form a stable stage II crack.

Under the conditions of true high cycle fatigue (n>10^6 cycles) the matrix yield stress exceeds the applied cyclic stress to such an extent that cyclic plastic strains are unlikely to initially develop even in regions of high stress concentration around inclusions. This is in marked contrast to the cyclic plastic zones that develop at inclusions of high rigidity after the first load cycle during intermediate-cycle fatigue [27]. The lack of a cyclic-plastic zone results in very different mechanisms of fatigue crack nucleation for true high-cycle fatigue conditions than for the intermediate cyclic fatigue conditions.

Eid and Thomason [23] conclude that for high cycle fatigue the inclusions must be either damaged or debonded from the matrix to initiate a fatigue crack. Following either, the subsequent fatigue cycling is accompanied by the formation of cyclic plastic zones at the inclusion which lead to the nucleation of fatigue cracks. It is important to note that the debonding of the inclusion/matrix interface is not essential to the nucleation of fatigue cracks. If the inclusion remains firmly bonded to the matrix but is damaged by the fatigue process the development of cyclic plasticity in the matrix and eventual fatigue crack initiation can still result. Either by debonding or by the fatigue failure of the inclusion itself a surface hole is formed which is responsible for the fatigue crack nucleation.

Regardless of the crack initiation mechanism it is important to define what is considered to be an active fatigue crack which can eventually propagate to cause failure. Lankford [24] observed periods of dormant growth for short stage I fatigue cracks. To become a stable stage II crack the accompanying inclusion must be debonded. This suggests that there exists a critical length below which the cracks do not propagate. This critical dimension is equal to the crack length plus the radius of the debond seam. A similar conclusion has also been reached by Murakami [25] who relates the fatigue limit of a steel to the presence of a critical crack length. The fatigue threshold is defined as the stress at which fatigue cracks will be initiated and propagate beyond a critical size.

2.5 Fatigue of Rail Steels

2.5.1 Introduction

The causes and mechanisms of fatigue failure of rails has received considerable attention [29-40]. The type of failure is a result of the fatigue crack initiation and subsequent growth mechanisms, which are a function of the characteristics of the rail steel and the operating and loading conditions. The purpose of this section is to discuss the different fatigue failure mechanisms of rail steel and the influence of nonmetallic inclusions.

2.5.2 Stress Distribution and Plastic Flow in the Rail Head

The stress distribution within the rail head due to in track service has been the subject of considerable research [29-33]. Common to any rail in service is the existence of a thin surface layer which experiences plastic flow [32,33]. The depth of the plastically deformed zone depends on the rail type and the loading conditions. For carbon rail Chipperfield [29] found that the plastically deformed zone extends to a depth of approximately 10mm, which is within the range given by Ravitskaya [34] (8-15mm). For alloyed and harder rail steels the plastically deformed zone only extends to a depth of (3-6mm) [35].

In the immediate surface layer the stress components are the parallel-to-flow shear and the normal-to-contact compressive stress components [30]. The distribution of these stresses has been calculated according to Hamilton's [36] closed form solution and is shown in Figure 2.5. Where z is the depth of penetration, a is the contact zone radius, τ_{yz} is the linear super position of the shear components due to the normal force and a lateral creep force and σ_z is the compressive stress component. Within a shallow layer at the top of the rail, a surface element will experience a repeated biaxial compression-shear loading, as shown in Figure 5(a). As the contact zone moves the values of τ_{yz} and σ_z reach their respective maximums at different points. The maximum shear stress occurs at the boundary of the contact zone. The shear stress increases with depth until reaching its maximum because it is a function of the contact forces and the internal constraints of the material. This is reflected in the flow of the subsurface layers which are highly constrained in relation to the surface layer [35].

Beneath the plastically deformed layer of the outer rail surface is a layer of residual tensile stresses [37]. The distribution of the tensile stresses depends on the cyclic loading

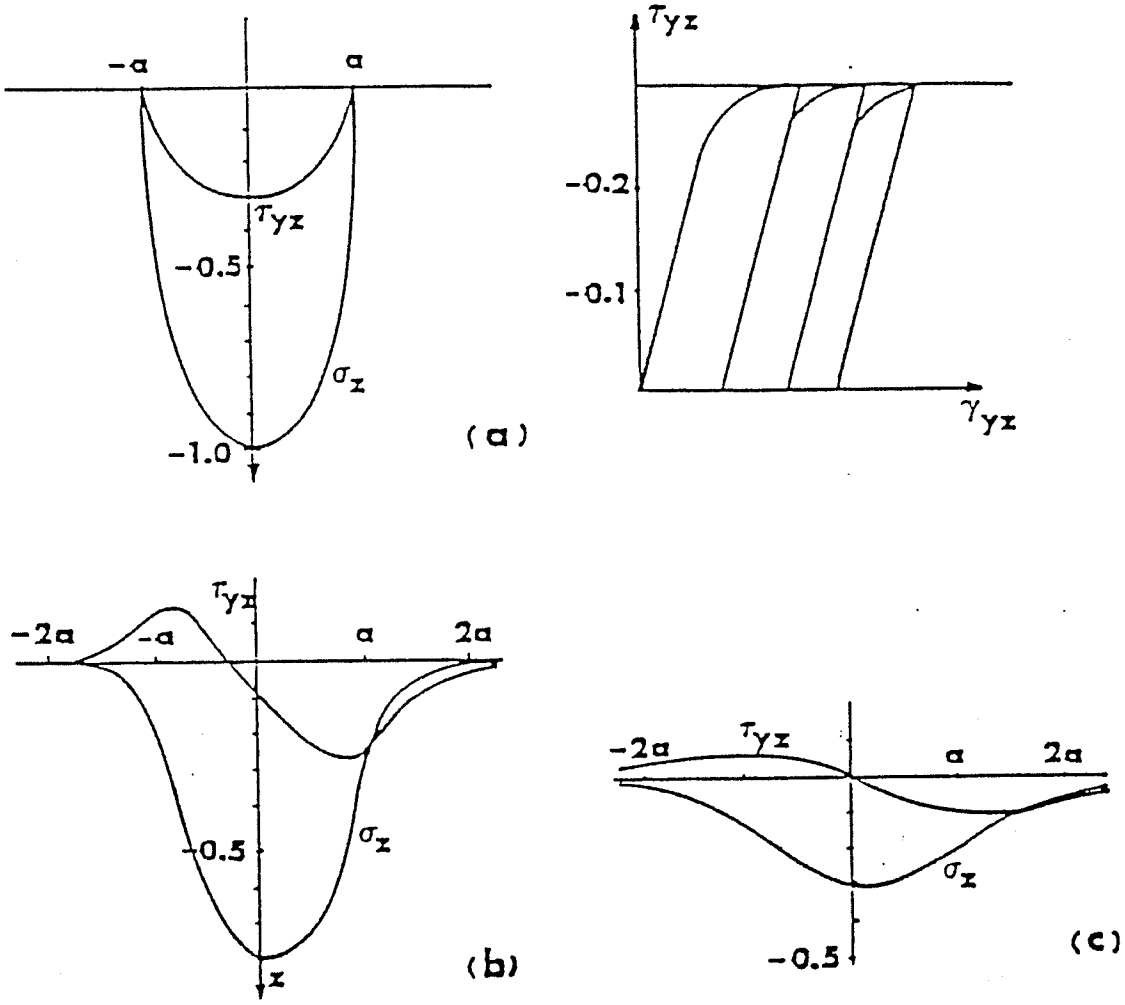

Figure 2.5. Compressive σ_z and shear τ_{yz} stress distributions at the depth, (a) z=0, (b) z=0.5a and (c) z=1.5a [36].

history and as a result there is no distinct pattern in the location of the maximum tensile residual stress across the rail head. This transition region between the plastically deformed region and the bulk elastic material is characterized by cyclic work softening [35,38]. In comparison the plastically deformed zone is accompanied by work hardening [35,37,38]. The cyclic deformation characteristics of four different rail steels has been investigated by Park and Fletcher [39], who concluded that all of the rail steels cyclically soften at low strains and harden at higher strains.

Drastic changes in the microstructure accompany the plastic flow of the immediate surface and subsurface layers. At the surface layer the pearlite is heavily deformed and consists of broken short lamellae [35]. The deeper subsurface layer has an alternating or zigzag pattern resulting from the action of the alternating shear. The cementite plates are either kinked in a wave like pattern and cracked or have thinned out. In the work softened zone the cementite is either straight with some cracking or slightly deformed in a sinusoidal pattern [38]. Even deeper in the rail the pearlite will remain undeformed.

2.5.3 Crack Initiation Mechanisms

Due to the transition from a plastically deformed region at the outer surface to a constrained elastic region at the inner core of the rail head there are several possible fatigue mechanism in the rail head. Within the plastically deformed layers Ghonem and Kalousek [30] conclude that surface cracks occur by ductile fracture of the immediate surface layer. Another failure mechanism of the immediate surface layers may result from the initiation of voids at subsurface defects [40]. Cracks originating from deeper subsurface layers result from the interaction between repetitive contact stresses and inclusions [29,40,41]. Ghonem et. al. [35] have proposed an additional mechanism for fatigue cracking at subsurface layers which is due to the formation of intrusions on the gauge face. The intrusions form as a result of the interaction between the plastically deformed zone and the

elastic bulk of the rail head. The resulting fatigue cracks propagate in a zone of high residual tensile stresses for the second two mechanisms.

In the shallow plastically deformed zone at the rail surface an incremental accumulation of plastic flow results from the shear stress, τ_{yz}, continually exceeding the rail steels elastic limit. This phenomenon is known as ratcheting or incremental collapse [32] and is depicted in the right hand side of Figure 5(a). As the ratcheting process continues the ductility limit of the surface layers, in the y direction (perpendicular to the rail direction) will eventually be reached and fracture takes place in the form of a surface crack. The driving force for the cyclic crack growth is predominantly Mode II in character because of the shear stresses present. Although this initiation mechanism is confined to the contact zone this zone will move laterally across the rail head due to the wheel and rail geometry constraints [41]. Therefore, the location of these surface cracks is random.

In contrast to the work of Ghonem and Kalousek, others [45] have predicted that the presence of large compressive residual stresses will inhibit crack initiation in the immediate surface layers of the rail. This theory is substantiated by the occurrence of transverse defects and other fractures which occur deeper in the rail head.

As an alternative to the failure process resulting from progressive shear deformation of the immediate surface layer Suh [40] has proposed a mechanism which considers voids and microcracks to nucleate at defects within the plastically deformed layer. As deformation continues microcracks grow and link up until a wear flake is formed at the surface or a fatigue crack is initiated. The microcracks may propagate by a low cycle fatigue mechanism, driven by the plastic strains [31].

Rail failures resulting from deeper subsurface defects include shell and transverse defects. These are the principal forms of fatigue cracking in heavy haul rail lines [44]. The effect of nonmetallic inclusions in initiating fatigue cracks has been investigated by Fowler and Tetelman [42]. A detailed investigation into the precise role of inclusions in initiating heavy haul fatigue cracks has been conducted by Chipperfield and Skinner [44]

and by Chipperfield et. al. [29]. These investigations involved a post-mortem metallographic examination of defective rails to locate and identify the causes of rail failure. The defects result from fatigue cracks which initiate below the gauge corners and grow within the interface between the work hardened layer and the core of the head [37]. The cyclic driving force provided by the wheel passage is coupled with large inplane tensile residual stresses. These tensile stresses below the work hardened layer provide the crack with a Mode I opening condition. Chipperfield et. al. [29] conclude that initiation at this location is associated with nonmetallic inclusions. Initiation occurs by matrix separation at inclusion edges followed by coalescence of the cracks from closely spaced neighboring inclusions until the crack reaches a critical size.

Individual large inclusions would provide the most effective crack initiators. Chipperfield and Skinner determined that the critical size of the inclusions was 80 μm in diameter. This is based on observations of actual initiation sites. The possibility of such a large inclusion being present in the critical location of the rail is rare. However, they did find clusters of inclusions in the critical region which have an effective combined diameter greater then the critical dimensions.

The effective stress raisers were inclusions of complex compositions containing aluminum, silicon, manganese and iron. Smaller amounts of titanium and calcium were also detected. These inclusions are either silicates or aluminates. Manganese sulfide inclusions were never found to be effective stress concentrators and therefore crack initiators. However, Fowler and Tetelman[42] determined that sulfide stringer inclusions were effective crack initiators. With the inclusions aligned approximately perpendicular to the specimen axis and the loading direction, sulfide stringer inclusions were found to initiate cracks. A similar loading orientation is present in the rail head for inclusions in the zone of tensile residual stresses. This difference in the type of inclusion which initiates cracks can be accounted for by the types of inclusions present in each steel. In the steels

investigated by Fowler and Tetelman, the usually more detrimental oxide and silicate inclusions are often surrounded by sulfur creating a less harmful duplex inclusion.

A different mechanism for crack initiation from subsurface layers has been proposed by Ghonem et. al. [35]. This new explanation is required to explain the continual problem of rail head failures from longitudinal cracks even with a continued improvement in rail steel cleanliness. Longitudinal cracks have even been observed to initiate at regions of the rail head with no trace of inclusions present. The similarity between the two mechanisms is that both provide a free surface which is required for internal crack initiation.

Instead of the free surface being formed by void coalescence at the inclusion/matrix interface it is formed by intrusions resulting from the incremental unidirectional plastic flow of the immediate surface layers. As the metal flow advances along the gage corner of the rail, it terminates in the form of displaced layers accumulating along the corner. The edge of each layer will interact with previously displaced layers or with the elastic matrix. These interactions were observed to generate surface intrusions [35].

As discussed before the crack will propagate along a plane of uniform hardening with residual tensile stresses present. Ghonem et. al. consider the crack to propagate by two modes; Mode I governed by the residual tensile stresses and Mode II due to the shear stress component of the applied load. This intrusion mechanism eliminates the need for large inclusions to be present in the critical region of the rail head in order to cause crack initiation.

An investigation of the fatigue behaviour of different rail steels has been performed by Fletcher and Park [42]. The four steels tested include a head hardened steel, two alloyed rail steels and a standard carbon rail. All fatigue testing was performed using strain control with the specimens axis aligned with the loading direction. With this configuration the elongated axis of the inclusion is also parallel to the loading direction. Their results conclude that both alloyed rails and the head hardened rail have superior fatigue resistance

compared to the standard carbon rail. That is, all the other rail steels have a longer fatigue live then the carbon rail at all stress levels tested.

2.6 Acoustic Emission and Applications to Fatigue Testing

2.6.1 Introduction

Acoustic emission (AE) is the transient elastic energy that is spontaneously released when materials undergo deformation, fracture or both [46]. Possible sources of the elastic waves has been discussed by Wadley et. al. [47], they include the rapid collective motion of a large number of dislocations, inclusion and precipitate fracture or pullout from the matrix, Luders band propagation in iron alloys, and rapid brittle crack extension. Because many of these processes occur during subcritical crack growth in materials, AE has the potential to be a monitor of crack initiation and propagation in engineering components [48].

Acoustic emission examination differs from most other nondestructive methods in two significant respects [49]. First, the energy that is detected is released from within the test object rather than being supplied by the nondestructive testing method. Second, the acoustic emission method is capable of detecting the dynamic processes associated with the degradation of structural integrity. Crack growth and plastic deformation are major sources of acoustic emission. The region near a crack tip may undergo plastic deformation as a result of high local stresses. In this case the crack tip acts as a source of stress waves and becomes an active acoustic emission source.

The acoustic emission method has the following advantages over other nondestructive testing methods; First, AE is a dynamic inspection method that provides a response to discontinuity growth. Second, AE can detect and evaluate the significance of the

discontinuity throughout an entire structure. Third, discontinuities that are inaccessible to other nondestructive methods may be detected since only limited access is required.

2.6.2 Acoustic Emission Signal Characterization

There are two distinct characteristic types of acoustic signals, they are burst signals or continuous emissions. Burst signals are characteristic of flaw or crack growth and continuous emissions have been attributed to dislocation movement in materials during microdeformation. Discrete or burst signals are thought to be generated by the elastic energy released by fractured material, by reorientation of the crack leading edge and by the dislocation movement (avalanching) created in the plastic zone associated with the leading edge of a crack or the rubbing of discontinuity surfaces [50].

Burst type acoustic emission can be described by relatively simply parameters. The signal amplitude is much higher then the background and is of relatively short duration. The signals are also well separated in time. Although they are rarely simple waveforms they usually rise rapidly to a maximum amplitude and then decay nearly exponentially to the background level.

Acoustic emission monitoring is usually carried out in the presence of continuous background noise. A reference or threshold voltage is normally set slightly above the background level. The burst signal can then be described by a number of waveform parameters which includes the count (ringdown count), event energy, signal amplitude, signal duration and signal rise time.

Counting the number of times the signal amplitude exceeds the threshold (the cumulative ringdown count) or its time derivative (the ringdown count rate) is the most common method of displaying an acoustic emission result [47]. The number of ringdown counts for an event detected by a transducer is given by [49]:

$$N = \frac{W V_o}{2 B V_t} \quad (2.2)$$

where:

V_0- initial signal amplitude

V_t - threshold voltage

B - decay constant (greater than 0)

W - angular frequency.

The limitations of using the ringdown count rate is this technique is strongly influenced by the operating conditions. Specifically the specimen geometry, the properties of the sensor, the bond between the sensor and the specimen, the sensor's threshold and the performance of amplifiers and filters. These combine to introduce a introduce a degree of irreproducibility to the results [47]. However, even given this limitation this technique has received considerable significance in describing the characteristics of fatigue crack growth [48,50-54].

2.6.3 Sources and Mechanisms of Acoustic Emission

The source of acoustic emission can be classified as either macroscopic or microscopic depending on how large a volume of the test material is contributing to the acoustic emission. Macroscopic sources include cracks, inclusions and voids while microscopic sources are dislocation motion through grains and across grain boundaries [52]. Due to the inherent interrelations microscopic sources are always present in macroscopic sources. However, only macroscopic sources will be discussed here because the microscopic sources were not relevant in this technique.

Plastic deformation is the primary source of acoustic emission in stressed metallic materials. The initiation of plasticity contribute to the highest level of acoustic activity observed on a stress-strain curve [52]. Correspondingly, most acoustic emission occurs at the yield stress of a material. Local yielding at a stress concentrator can also be a

source of acoustic emission. In addition to plastic deformation crack growth is also a major source of acoustic emission. This explains why acoustic emission methods have been used to characterize fatigue and fracture of metallic materials.

2.6.4 Applications of Acoustic Emission to Fracture Mechanics

Acoustic emission has been used to characterize the plastic zone ahead of a crack tip in notched specimens [55]. This in turn has lead to a correlation between acoustic emission and the parameters that characterize the state of stress at crack tip. In addition to the plastic zone size these parameters include the crack length, the stress intensity factor K and the fracture strain at the crack tip.

Dunegan et. al. [56] suggested that the total emission count is proportional to the plastic volume ahead of the crack. This model is based on the fact that acoustic emission is associated with plastic deformation processes. Several assumptions were necessary to formulate this model. First, the materials highest rate of acoustic emission occurs when it is loaded to the yield strain. Second, the size and shape of the plastic zone ahead of the crack may be determined from linear elastic fracture mechanics. Third, the strains at the crack tip vary as $r^{1/2}$, where r is the radial distance from the crack tip. Fourth, the acoustic emission count rate, $\dot{N}$, is proportional to the rate of increase for the volume of the material, V_p, strained between the yield strain E_y and the uniform strain E_u, or:

$$\dot{N} \propto \dot{V}_p \tag{2.3}$$

The volume of this strained zone is found to be proportional to the stress intensity factor raised to the power of four, or:

$$V_p \propto K^4 \tag{2.4}$$

This proportionality is derived from the radius of the plastic zone, which is calculated using linear elastic fracture mechanics. Combining equation (2.3) and equation (2.4) yields

$$N \quad \alpha K^4 \tag{2.5}$$

Experiments to confirm the theoretical exponent of 4 have constantly produced higher values. Generally ranging from 6 to 11 [52]. The importance of this model lies in correlating the acoustic emission due to the plastic deformation at the crack tip with the stress state ahead of the crack.

In order to extend the analysis of the plastic deformation model to ductile materials which exhibit contraction at the crack tip the exponent of equation (2.5) has been increased [57], to be within a range from 7 to 11 [58].

Another model relating acoustic emission activity to the state of stress at the crack tip of a loaded notched specimen was developed by Palmer and Heald [55]. This model also uses the concepts of linear elastic fracture mechanics. In contrast, this model suggests that the total acoustic emission count rate is proportional to the area of the elastic plastic boundary ahead of the crack instead of being related to the plastic volume ahead of the crack. The acoustic emission activity can be related to either the discontinuity or to the applied stress at fracture, by

$$N = Ds \tag{2.6}$$

where:

N - total acoustic emission count rate

s - size of the plastic zone ahead of the crack

D - constant of proportionality.

The value of D depends on the strain rate, temperature, specimen thickness and microstructure. The plastic zone size is a function of the crack and specimen geometry, the applied stress and the yield stress and is given by:

$$s = c\{\sec(\pi \sigma/2 \sigma_1) - 1\} \qquad (2.7)$$

where:

c - half the crack length

σ_1 - characteristic strength of the material.

The total emission count rate is then given by:

$$N = Dc\{\sec(\pi \sigma/2\sigma_1) - 1\} \qquad (2.8)$$

From the results of their investigation Palmer and Heald concluded that the plastic zone must be expressed by equation (2.7) or an equivalent equation. A simple fracture mechanics expression and the resulting proportionality of equation (2.5), is inadequate for situations involving appreciable yielding. Another conclusion is that the source of acoustic activity for the steel tested was the immediate vicinity of the elastic-plastic boundary and the total emission count was directly proportional to the plastic zone size.

2.6.5 Acoustic Emission from Fatigue

It is well known that acoustic emission are generated during the growth of fatigue cracks [51]. Acoustic emission monitoring during cyclic loading of a specimen or structure presents a method for detecting the initiation and propagation of fatigue cracks. It can also be used to monitor low cycle fatigue [52].

In order for acoustic emission monitoring to be a viable technique for detecting crack initiation the emission activity resulting from a crack must be separated from the background noise. There are several proposals for discriminating actual signals from the noise. One involves an electronic window which is used to segregate measurements on valid signals during selected parts of the loading away from the background noise. Another uses two transducers which are mounted at equal distances from the source. Only signals that reach both sensors simultaneously are considered valid. A third approach is to use a fatigue analyzer to show the acoustic events as a function of time and of the loading cycles.

The relationship between the acoustic emission count rate N' and the stress intensity factor ΔK has been described by Bassim [53] and has the form:

$$N' = A(\Delta K)^n \tag{2.9}$$

where A and n are constants. This equation has a strong similarity with the Paris law for crack propagation in fatigue, namely

$$\frac{da}{dN} = C(\Delta K)^m \tag{2.10}$$

This suggests that the mechanisms for crack growth are also directly responsible for the acoustic emission activity.

Attempts have been made to relate the exponent n of equation (2.9) to the exponent m of equation (2.10). The value of n has been reported to equal 5 [58] or in another case n=m [59] and n=m+2. The mechanisms of acoustic emission are due to either an energy release during crack extension or the deformation and fracture within the plastic zone. In some cases both mechanisms will be operational and n assumes a higher value. This depends on

the materials ductility and on the loading condition. If both conditions are operational the overall count rate will be [52]:

$$N'.= N'_p + N'_c \tag{2.11}$$

The individual mechanisms can be described as:

$$N'_p = C_p\Delta K^m\Delta K^2/(1-R)^2 \tag{2.12}$$

and

$$N'_c = C_s\Delta K^m/(1-R)^m \tag{2.13}$$

From these relationships fatigue life curves based on acoustic emission can be derived for a material.

The dependance of the acoustic emission count rate on the material's ductility is reflected in the differing behaviour for ductile and brittle steels. In lower strength steels the majority of acoustic emission occurs during the period of plastic-zone expansion, while the increments of crack growth appear quiet [47]. For high strength steels the processes associated with plastic-zone expansion no longer dominates the total emission. Many high strength steels generate appreciable emission during crack growth [47,54].

In low cycle fatigue the curve of acoustic emission total counts versus number of cycles to failure is characterized by three stages which corresponds closely with the stress state in a material [53]. This is shown in Figure 2.6 for 4340 steel.

The three stages can be described as follows. first a period of high acoustic emission activity which corresponds to the initial softening or hardening of the material. This is followed by a decrease in activity as the material enters a quasi-stable state and finally a

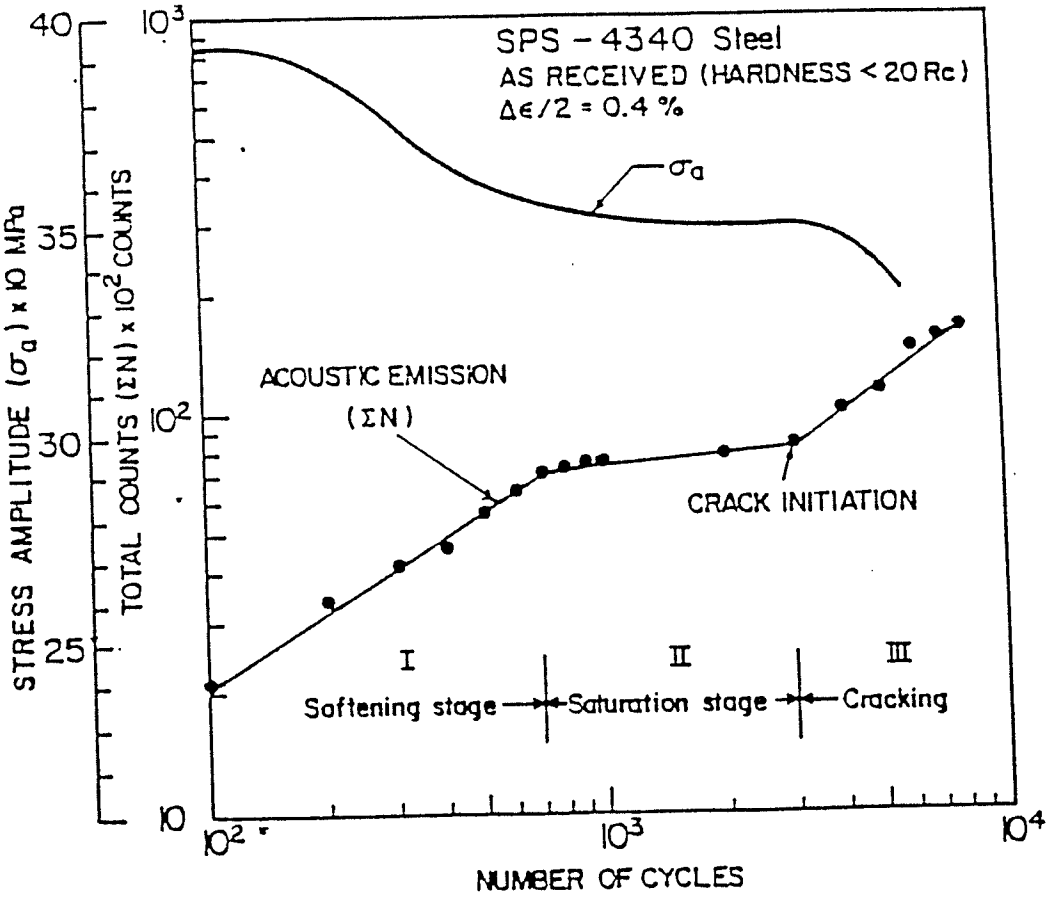

Figure 2.6: Acoustic emission and stress amplitude as a function of number of cycles to failure in low cycle fatigue, from ref [53]

further increase in activity which corresponds to crack initiation and propagation to failure. If the extent of damage is taken as the ratio of the number of cycles N_b to the total number N_f of cycles to failure, then the following equation applies.

$$\Sigma N = B(N_b/N_f)^{m'} \qquad (2.14)$$

Where B and m' are constants for the material. This equation relates acoustic emission test data to the fatigue life of a material and can be used to evaluate the extent of fatigue damage.

2.6.5 Conclusions

This review discusses the sources and mechanisms of acoustic emission. Only macroscopic sources were considered due to their relevance in the present investigation. The relationship between acoustic emission activity and the mechanisms of fatigue and fracture of metallic materials are also discussed. Several models relating acoustic activity to the failure mechanism were presented. Specifically these models relate fracture mechanics parameters and the fatigue parameter ΔK to the acoustic emission activity.

Chapter III

Experimental Procedure

3.1 Materials Tested.

The materials used in this investigation were four pearlitic rail steels supplied by the CN Technical Rail Research Centre in the form of as-rolled rail sections. None of the rails were ever in service. The types of rail steels tested is shown in Table 3.1. The weight percentage of the alloying elements of each rail steel is given in Table 3.2.

All four steels are fully pearlitic but differ in terms of their inclusion content and pearlite spacing. Characteristic to all the rail steels are MnS inclusions which are elongated in the rolling direction of the rail and tend to be clustered into streaks. Also common to all the steels are circular oxide inclusions which have a more random distribution. The inclusion distribution in the longitudinal direction with respect to the axis of rolling, is shown in Figure 3.1. The plane of observation is parallel to the rail head's upper surface.

All of the real steels were tested in their received condition, no additional heat treatment was performed.

3.2 Sample Preparation.

3.2.1 Bending Specimens Location.

The specimen blanks for the four point bending samples were cut from the rail head at the location shown in Figure 3.2. The distance from the rail head surface to the specimen was just deep enough to ensure that the specimens had the required length. The specimens were cut so their length was transverse to the rail direction. Each specimen was machined from the rail head at the same depth.

Table 3.1 Rail steels tested

Reference Letter	Types of steel tested
A	electric furnace steel
B	136 lbs, 300 BHN
C	136 lbs, 1985, 276 BHN
D	fully head hardened

Table 3.2 Rail Steel's Alloying composition

Steel Type	%C	%Mn	%P	%S	%Si	%Cr	%Al
A*	0.814	1.04	0.018	0.009	0.417	0.37	0.0016
B*	0.810	0.98	0.017	0.013	0.410	0.31	0.0100
C*	0.770	0.84	0.020	0.021	0.290	-	0.004
D	0.780	0.79	0.026	0.008	0.87	0.54	0.002

* Composition supplied by Canadian National Railways

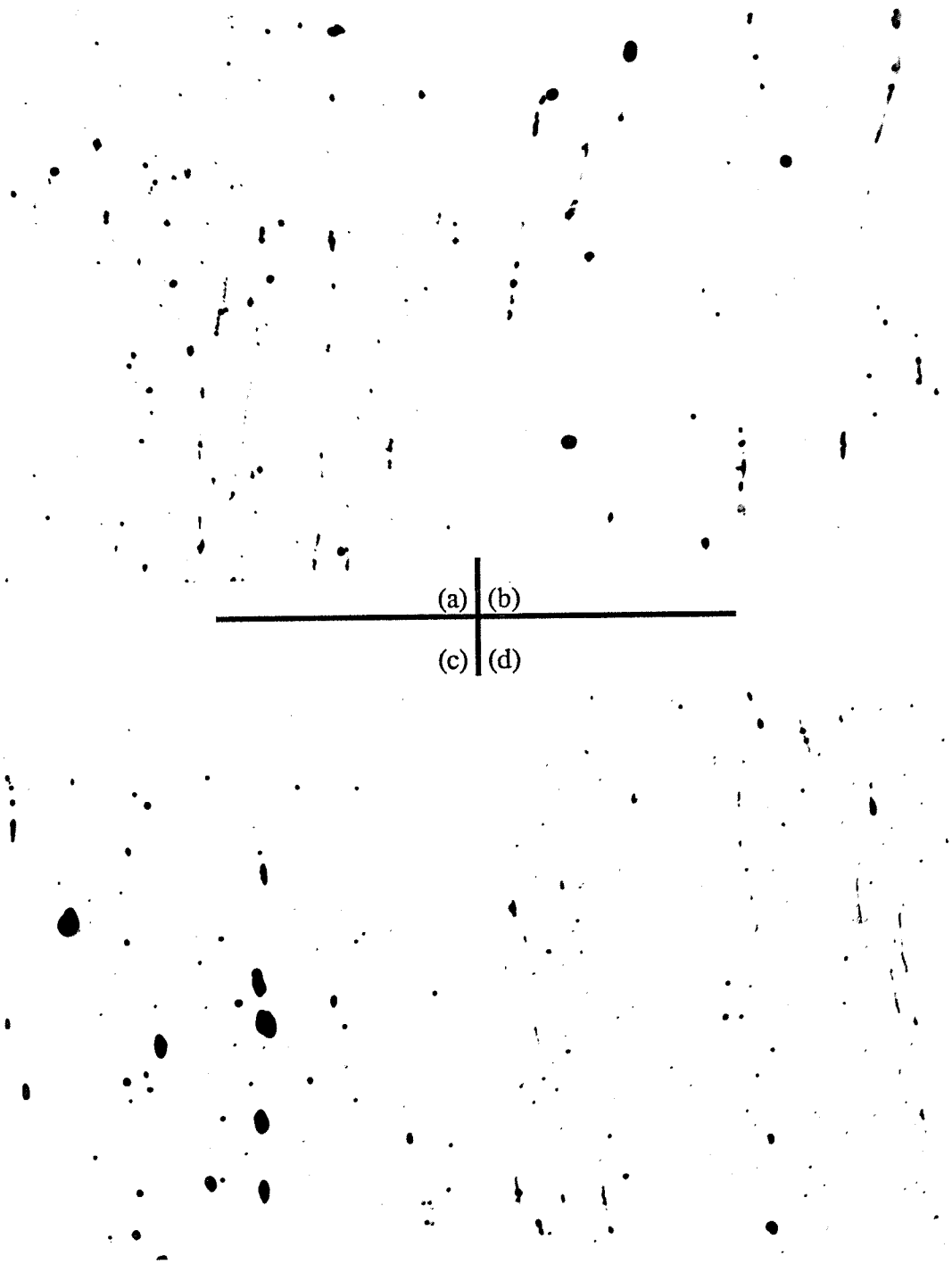

Figure 3.1 Inclusion distribution in the four steels,50X:
(a) steel A, (b) steel B, (c) steel C, (d) steel D.

3.2.2 Bending Specimens Geometry and Dimensions.

The specimens were cut from the blanks shown in Figure 3.2. The specimens for the fatigue tests were cut to the geometry shown in Figure 3.3 and had dimensions of 70mm in length, 25.4mm (1.0") in width and had a thickness of 5mm at the ends and 3mm at the reduced section in the middle. The length of the reduced section was 18.0 mm.

The purpose of the reduced section was to ensure that the fatigue cracks would not initiate at the points of contact between the pins and the specimen. Instead the fatigue cracks would initiate on the tensile surface within the reduced section. The length of the reduced section was large enough to ensure that the piezoelectric transducer would sit flat against the specimen's surface.

For the strength tests simple constant thickness coupons were used. This was done to avoid introducing any errors into the strength calculations due to the reduction in the thickness. They were 70mm in length, 25.4mm in width and had a constant thickness of 3.0mm.

3.2.3 Surface Condition of the Reduced Section.

The entire fatigue testing procedure, outlined in section 3.3 was performed using both unpeened specimens and shot peened specimens. The purpose of the shot peening was to introduce compressive stresses into the specimens to duplicate the work hardening of the rail head that occurs in service.

For the unpeened specimens the tensile surface at the reduced section was ground and polished to a 1μm finish. The reduced section was polished by hand using SiC paper, the final paper was 600 grit. Following sanding the surface was polished with field metallographic polishing wheels using diamond paste to a final surface roughness of 1mm. The surface was polished to a 1mm finish to avoid any effects on the fatigue performance of the samples due to surface stress concentrators and to aid in the observation of cracks following testing.

To introduce compressive stresses the specimens were sent to Griffin Canada Inc. for shot peening. The specimens were subjected to a shot blast for 29 seconds. The shot used was 660 grit steel with 90%-94% new shot. The peening intensity resulted in a 0.01" deflection of an Almen test strip. The entire tension side of the specimen was covered by the shot blast.

3.2.4 Optical Metallography Specimens.

For metallographic observations sections were cut from the untested specimen blanks, shown in Figure 3.4 (a) The surface for observation of the inclusion morphology was parallel to the rail's upper surface. The specimens were mounted in bakelite and polished mechanically using SiC paper and diamond paste with nylon clothes to a surface roughness of approximately 0.25μm. A final polish to a 0.05μm finish followed using micro metallurgical Linde B polishing powder. Both etched and unetched samples were prepared for observation. The etchant was a 2% nital solution, 2 parts nitric acid in 98 parts ethanol.

For the shot peened specimens samples were also cut to observe the depth of penetration of the shot peening and to observe its effects on the pearlitic structure. The plane of observation for these specimens was transverse to the rail direction and perpendicular to the rail head's upper surface, as seen in Figure 3.4 (b). These specimens were also mounted in bakelite and polished to a 0.05μm finish. The specimens were etched to reveal the pearlitic structure after shot peening.

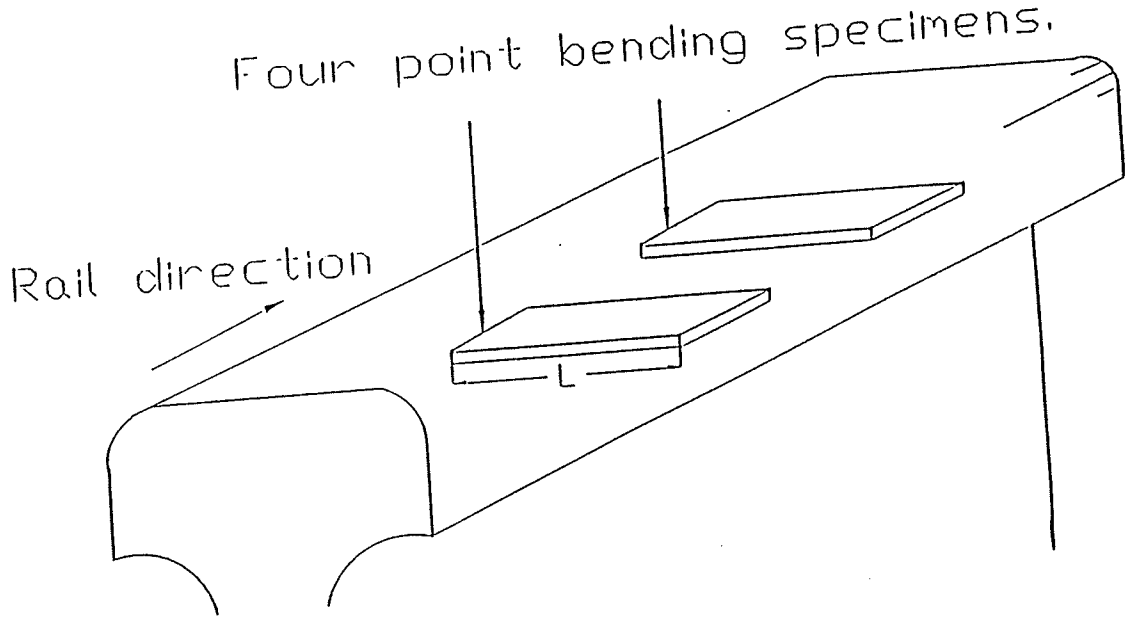

Figure 3.2 Location of Specimen blanks

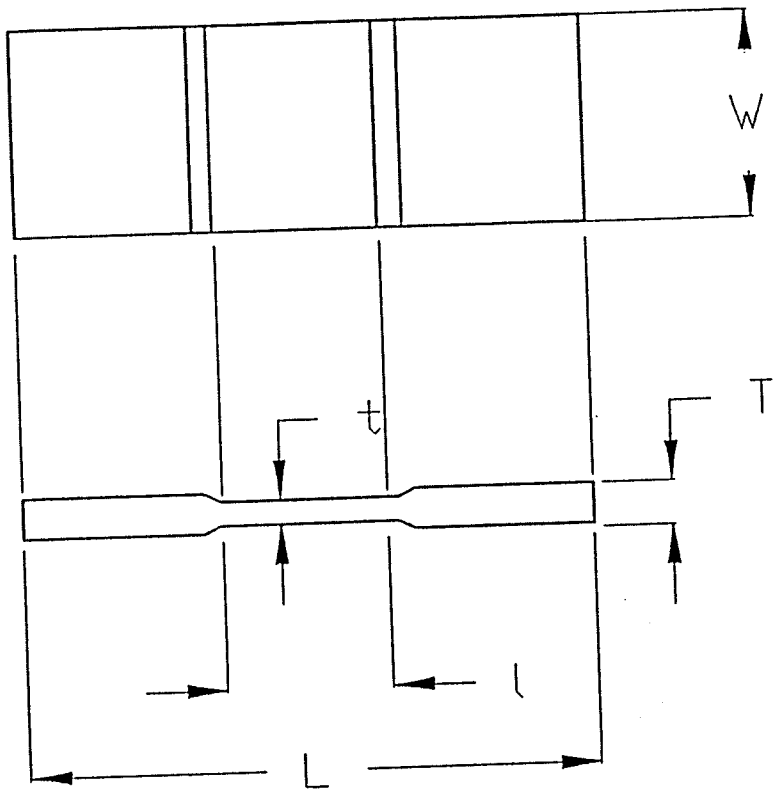

W=25.4
T=5.0
t=3.0 +/- .05
L=70.0
l=18.0

All measurements
are in mm.

Figure 3.3 Geometry and dimensions of the four point bending samples.

3.3 Mechanical Testing.

3.3.1 Material's Strength and Hardness.

Before performing either of the fatigue tests the strength and deformation characteristics of each steel was determined. A bending sample of constant geometry was subjected to a continually increasing load until the ultimate strength was reached. The bending configuration is shown in Figure 3.5.

The offset yield strength in bending was determined from the bending load-deformation curve using the following calculation.

$$\sigma_p = \frac{3P_p a}{bh^2} \qquad (3.1)$$

where:

σ_p - bending proof strength, (pa)

P_p - the load which produces a permanent set,(N)

a - the distance from the support to the load applicator, (m)

b - specimen width,(m)

h - specimen thickness, (m)

The permanent deflection, δ_p,which produces a permanent strain in the outer fiber of 0.01% is given by

$$\delta_p = \frac{(3L^2-4a^2)E}{12h} \qquad (3.2)$$

where:

L - span between supports,(m)

E - strain

Hardness measurements were performed on polished flat specimens using a Rockwell hardness tester. All measurements were taken using the Rockwell C scale.

3.3.2 Fatigue Testing Programs.

To characterize the fatigue behaviour of the four rail steels samples of each were subjected to two different fatigue testing programs. For the first testing procedure the specimen was subjected to a designated schedule of tensile stresses which increases in a stepped pattern. For the second testing program the samples were tested at a constant mean stress level. For both testing programs the specimen was tested in a four point bending configuration.

3.3.3 Stepped loading testing program.

This testing procedure was performed on 3 specimens per steel type for both the unpeened and the peened surface condition. All testing was done using a servohydraulic testing frame, Instron model number 1332 with a digital controller, model number 8500. All tests were conducted in air at room temperature.

The loading program that was followed for these tests is shown in Figure 3.6. The mean load was increased in increments of 20% of the bending strength, σ_y for the C steel. The values for the loading program are shown in Table 3.3. For all the mean stress levels the ration of the minimum stress to the maximum stress R was 0.3 and the frequency of testing, f, was 30 hz.

The values of the minimum and maximum stress change at each mean stress level. These were calculated using the following equations.

$$R = \frac{\sigma_{min}}{\sigma_{max}} \qquad (3.4)$$

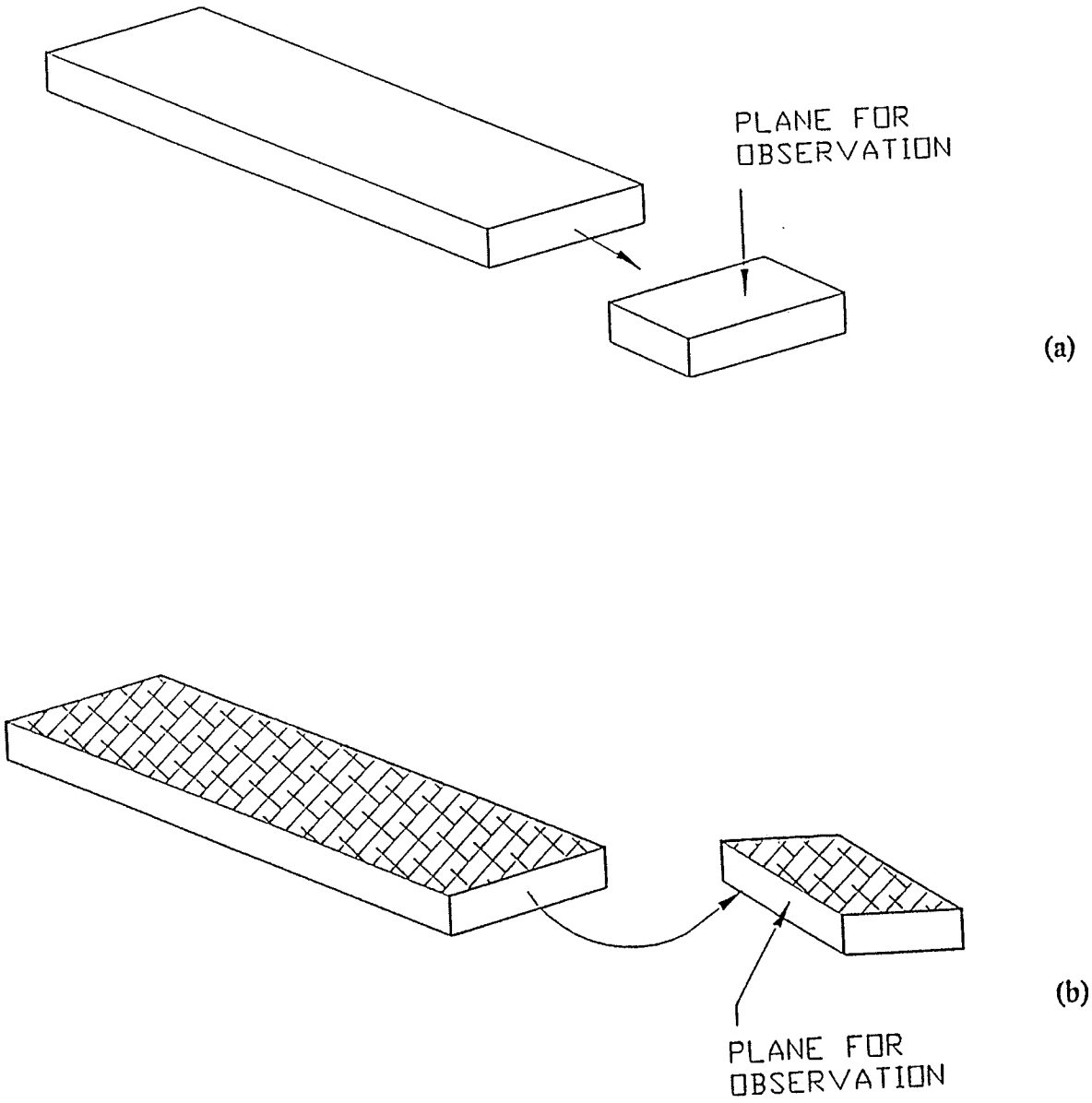

Figure 3.4. Samples for metallographic observation.
(a) The observation plane is parallel to the upper surface of the rail.
(b) Shot peened samples, observation plane is perpendicular to the rail direction.

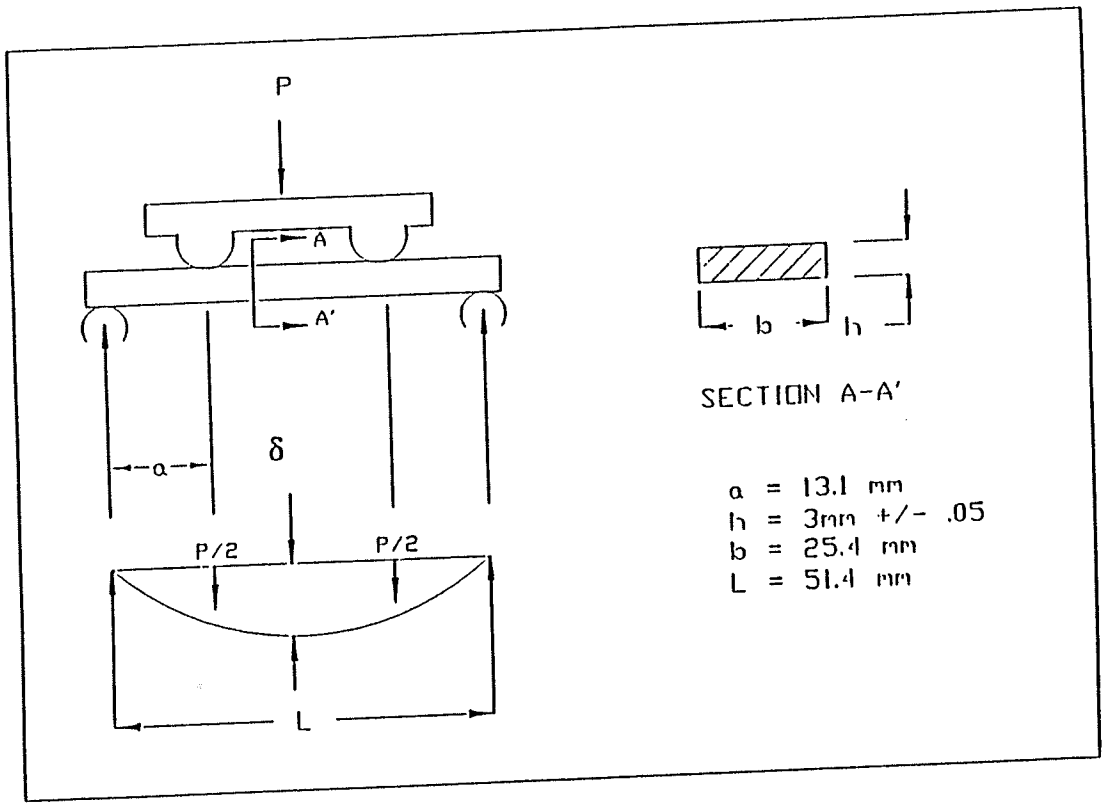

Figure 3.5. Loading configuration for the four point bending strength tests.

$$\sigma_m = \frac{\sigma_{max} + \sigma_{min}}{2} \qquad (3.5)$$

where:

σ_m is the mean load stress.

In these two equations there are two unknowns which can be solved for by substituting equation (3.5) into (3.4) and then solving for the remaining unknowns. The resulting equation is

$$\sigma_{max} = \frac{2\sigma_m}{1 + R} \qquad (3.6)$$

and σ_{min} can be found from (3.4).

$$\sigma_{min} = R\,\sigma_{max}$$

At each stress level the testing was continued for 100 000 cycles or until crack initiation was detected. Crack initiation was detected by monitoring the acoustic signals generated within the specimen. At the earliest indication of a fatigue crack the test was stopped.

3.3.4 Fatigue Testing at a Constant Mean Stress Level.

To more fully characterize the fatigue behaviour of the rail steels specimens of each steel were tested at a constant mean stress until crack initiation occurred. These tests were performed using the same servo-hydralic testing machine. The stress levels used were the same as for the stepped testing programs. The testing parameters were also the same, R=0.3 and F=30 hz.

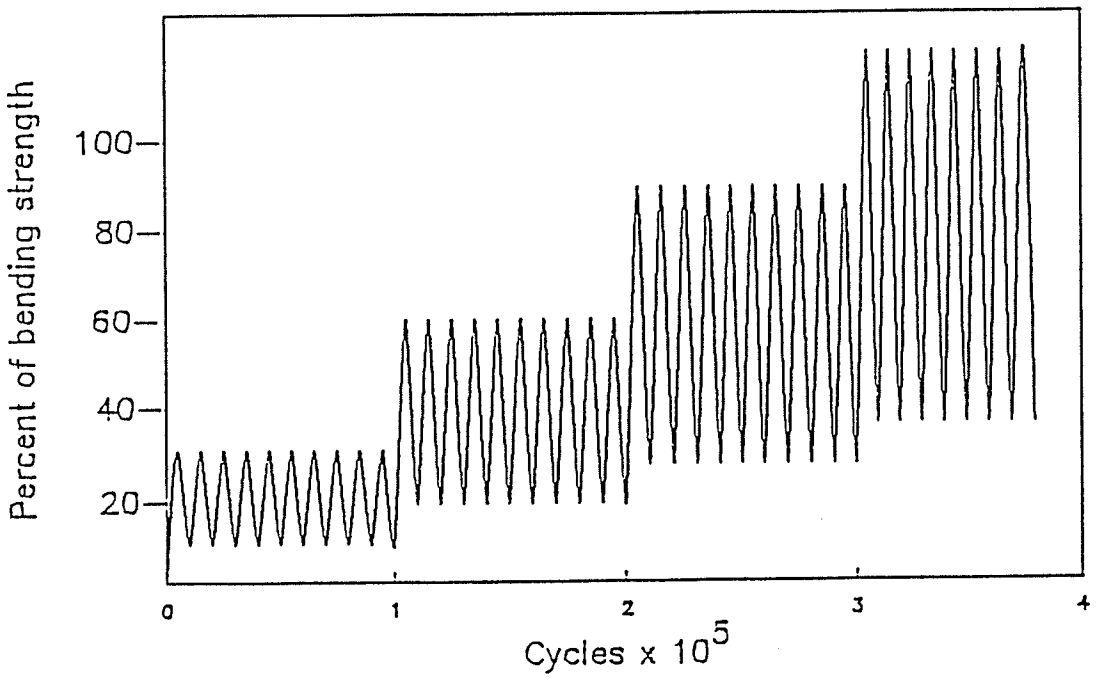

Figure 3.6 Stepped loading program. The mean stress was increased by increments of 20% of σ_y for steel C.

3.4 Acoustic Emission Monitoring.

3.4.1 Experimental Setup.

A surveillance unit supplied by Monac International Corporation was used to monitor the acoustic emission during all the fatigue testing. This system has been designed to detect the onset of crack initiation and to analysis the fatigue crack growth in steels.

The experimental setup is shown in Figure 3.7. A piezoelectric transducer was held to the reduced section's tensile surface by rubber bands and a silicon grease. The transducer's output was fed through a signal preamplifier to the surveillance unit. The acoustic emission signals were analyzed using Monac software run simultaneously during testing on a controlling computer which communicated with the surveillance unit. The amplified and filtered acoustic emission signals were also fed to a digital storage oscilloscope for calibration purposes.

3.4.2 Calibration Procedures.

Before beginning the acoustic emission monitoring the system was calibrated to insure accurate results. A consistent signal was generated by breaking a pencil lead on the surface of a specimen [60]. The output was captured by both the Monac surveillance unit and a storage oscilloscope. The peak energy and duration of the two captured signals were then compared.

Table 3.3 Loads used at each testing stage.

	Stage 1	Stage 2	Stage 3	Stage 4	Stage 5	Stage 6*	Stage 7*
	20%	40%	60%	80%	100%	120%	140%
σ_{min}	47	94	142	188	235	282	330
σ_a	55	110	164	220	275	330	384
σ_m	102	204	306	408	510	612	714
σ_{max}	157	314	470	628	785	942	1098

All stresses are in MPa.

*For the high strength steels only.

All the loads below and to the right of the double hatched line are above the yield strength of C steel and therefore, the calculated stresses are incorrect because they are based on elastic conditions.

Prior to testing the signal from the transducer was filtered to eliminate background noise. The transducer was mounted on a specimen which was held at a steady load, with no cyclic waveform applied. The window settings, which filter the transducer signal, were tailored to reduce as much background noise as possible while maximizing the capture of true acoustic events. Figure 3.8 shows an idealized acoustic emission event and the background noise. The five signal parameter windows which can be adjusted are given in Table 3.4.

The procedure followed for signal processing was as follows. First, the threshold level was set above the background noise level seen on the oscilloscope. Then the interval time was set at 1 minute. Now a cyclic waveform was applied to the specimen and the gain was adjusted so that the signal peaks were above the threshold. Now the acoustic emission analysis program was run to capture the signals. The energy, peak energy, duration and risetime of the captured signals were noted and all of the window settings were adjusted to maximize the effectiveness of the Monac Surveillance unit.

After the windows were set the gain, threshold level and interval time were adjusted to optimize the system's responsiveness. With an interval time of 30 seconds and with a testing frequency of 30 hz, they were 900 cycles per interval. This was a constant for all the tests. the gain was set large enough to insure that crack initiation was detected but not so large as to fill the burst (event) storage RAM with signals from the background noise.

3.4.3 Signals Monitored During Testing.

For the purposes of detecting the onset of crack initiation in steels the count rate is an effective and commonly used technique. The Count parameter measured by the Monac unit represents the number of positive threshold crossing in an event, see Figure 3.8. For these tests an increase in the number of counts per interval corresponds to the initiation of a fatigue crack in the specimen. With the onset of crack initiation the test was terminated.

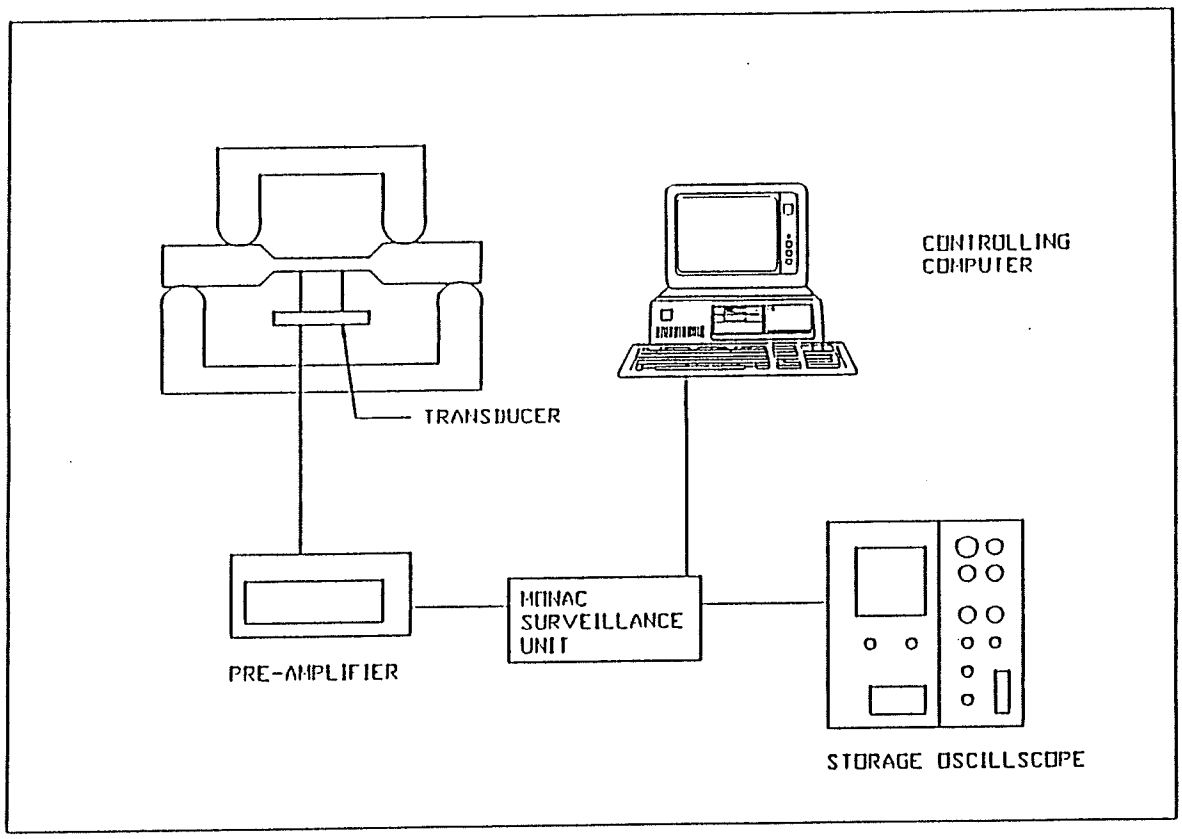

Figure 3.7. Acoustic emission surveillance equipment.

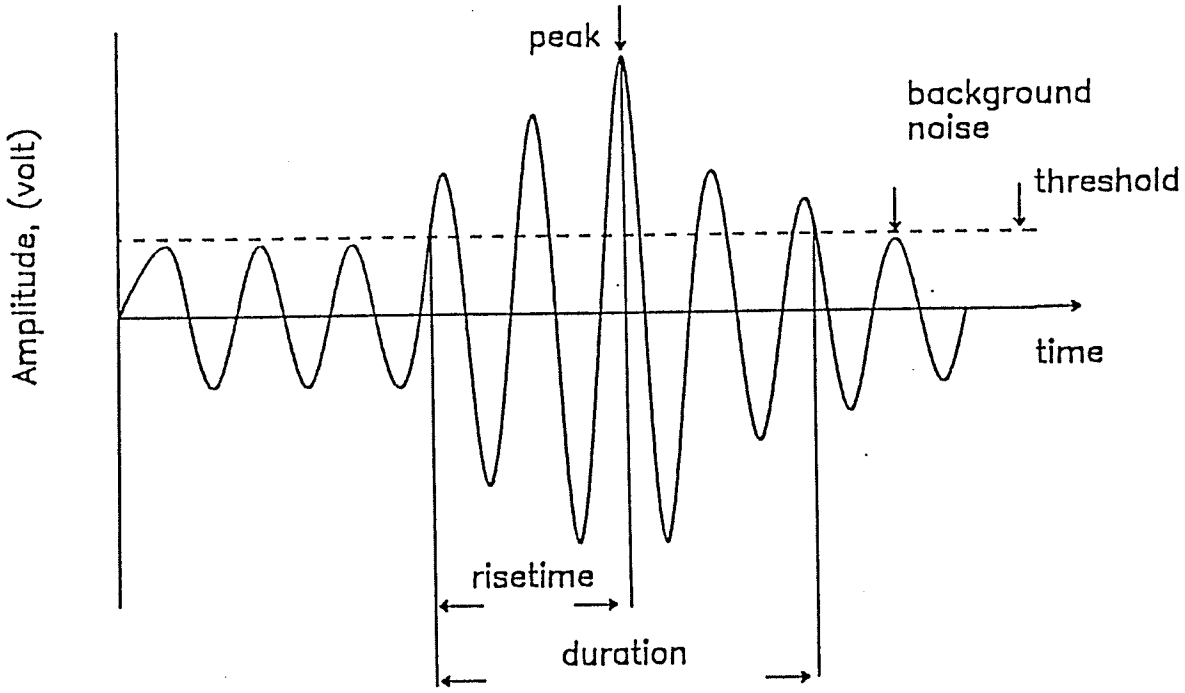

Figure 3.8. An idealized acoustic emission event.

3.5 Microstructural Examination.

3.5.1 Optical Microscopy.

Optical microscopy was performed to determine the structure of all the steels tested and the morphology of the non-metallic inclusions present in the steels. The size, shape and distribution of inclusions were measured on unetched samples. For this investigation the microstructure of the plane parallel to the upper rail surface was of primary interest. All the metallographic specimens were prepared as described in section 3.2.4 and examined using a Nikon Epishot optical microscope equipped with a 35mm camera. The objective magnifications ranged from 50X to 1000X. Image analysis was performed on unetched specimens using the technics outlined in section 3.6.

3.5.2 Scanning Electron Microscopy

Scanning electron microscopy (SEM) was used for high resolution observations of unetched specimens to analyze the types of inclusions present and for etched specimens to measure the inter-lamellar spacing. The techniques used are described in section 3.6. The microscope used was a JEOL JXA-840 operating at 10 Kv.

3.5.3 Crack Observations.

Tested samples which were suspected to contain cracks were examined using both the optical microscope and the SEM. Using either microscope the entire tension side of the reduced section was examined to find the point of crack initiation. By using the energy dispersive x-ray analyzer attached to the SEM small suspected cracks were analyzed to insure they were not thin inclusions. Using the same equipment the length of the crack and the accompanying inclusion were also measured. To ease detection typical specimens were sectioned after testing and mounted in bakelite. The reduced section was then polished according to the procedure outlined in section 3.2.4.

Table 3.4 Signal conditioning parameters:

Burst Window Settings	Hardware Settings
Energy	**Gain**
Count	**Threshold**
Peak	**filter**
Risetime	
Duration	
(a)	(b)

(a) The burst window settings
(b) Hardware settings

For the shot peened specimens the reduced section's tensile surface was polished after testing. This surface was polished according to the procedure outlined in section 3.2.3. After polishing there is still evidence of the shot peening. The entire shot peened surface was not removed in order to avoid polishing away any cracks. Typical samples were also sectioned and mounted.

3.6 Quantitative Metallography

3.6.1 Inclusion Morphology

Analysis of the volume fraction, size and shape of the non-metallic inclusions was performed using unetched polished metallographic specimens. All four steel types were examined. The plane of observation was parallel to the rail head's upper surface. All the image analysis was performed on a Leitz/Tasic automated image analyzer interfaced to a DEC(PDP-11) computer. Customized software programs were employed to measure specific parameters and to calculate their statistical distribution. All the examinations were conducted at 520X magnification.

Quantitative observations revealed the great variation in the inclusions morphology from region to region in the FHH steel and the C steel. Therefore, for these tow steels all of the inclusion morphology measurements were repeated on at least two specimens. One from a region of low inclusion content, (a clean region) and one from a region of high inclusion content (a dirty region).

The volume fraction of the non-metallic inclusions was found using a manual point count method. The volume of each inclusion type is the percentage of intercepts between a reference marker and the sample that coincides with an inclusion. Using this method it was possible to distinguish round inclusion (primarily oxides) form large elongated inclusions (mangenese-sulfides). The test was repeated over a large area of the sample until the measured volume percentage of each phase became constant.

The size of the inclusions was measured by two parameters. First, the mean cord length, which is the average of three projections, measured at 0°, 120° and 240°, see Figure 3.9 (a). The second parameter used to measure the size of the inclusions was the feret diameter, which is defined as the length of the side of the smallest rectangle that can be drawn around an object at a specific orientation, see Figure 3.9 (b). The feret diameter was measured in 15° intervals from 0° to 165°. The program returned the value for the maximum feret diameter and the feret at 90° to the maximum. The feret diameter measurement is dependant of the object's shape but the mean cord length is independent of the object's shape.

A measurement of the inclusion's spacing was determined by calculating the mean free path between inclusions from the size and volume fraction measurements. The mean free path for a random distribution of particles is given by [61]

$$\lambda_i = L_i(V_i^{-1} - 1) \qquad (3.7)$$

where:

λ_i = mean free path

L_i = mean particle size

V_i = volume fraction of particles.

The shape of the inclusions was determined from the minimum and maximum feret diameter measurements and from a second measurement, the form factor. The form factor is derived from an object's area and perimeter measurements. It ranges from 0 for an infinitely narrow line to 1 for a perfect circle. The area of each individual detected particle was also measured.

All of the measurements taken with the image analyzer were tailored to eliminate inclusions that were not significant influences on the fatigue behaviour of the steels. Individual particle analysis was used to measure inclusions which were found to initiate

cracks. Inclusions which were smaller then the critical size determined by the individual particle analysis were eliminated from the statistical distribution.

3.6.2 Pearlite Interlamellar Spacing

The mean interlamellar spacing was determined from an average of manual measurements made directly on 20 pearlite colonies obtained from SEM examination. Approximately 2-3 measurements were made on each pearlite colony using a mean directed measurement [62], shown in Figure 3.10. The spacing is found using the formula:

$$S_m = \frac{D}{NM} \tag{3.8}$$

where:

S_m = mean directed spacing

D = perpendicular distance from centre to centre of cementite layers

N = number of lamellar intersected

M = magnification

This procedure was repeated on all four steels. For all the steels two different methods were used to select the pearlite colonies for measurement. First, the finest pearlite colonies were selected. Second, a random selection method to represent the variation in inter-lamellar spacing within each steel.

3.6.3 Type and Composition of Inclusions.

To characterize what type of inclusions were present in the steels, unetched samples were prepared as out lined in section 3.2.4 and examined using energy dispersive x-ray analysis (EDX). The EDX system is attached to the JEOL SEM. Each type of inclusion present in each steel was analyzed. However, oxide inclusions could not be analyzed

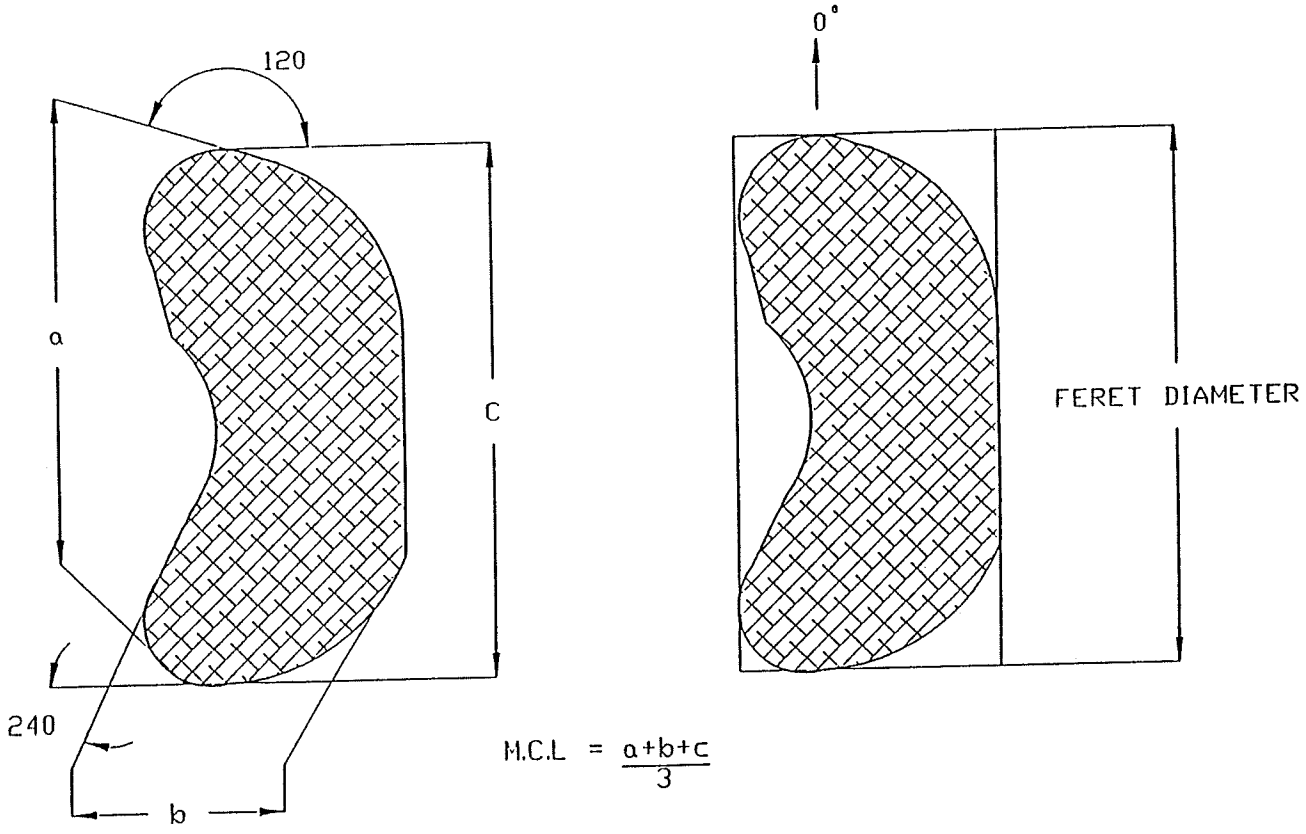

Figure 3.9 Image analysis parameters: (a) Mean cord length (MCL) and (b) feret diameter at 0^{o}.

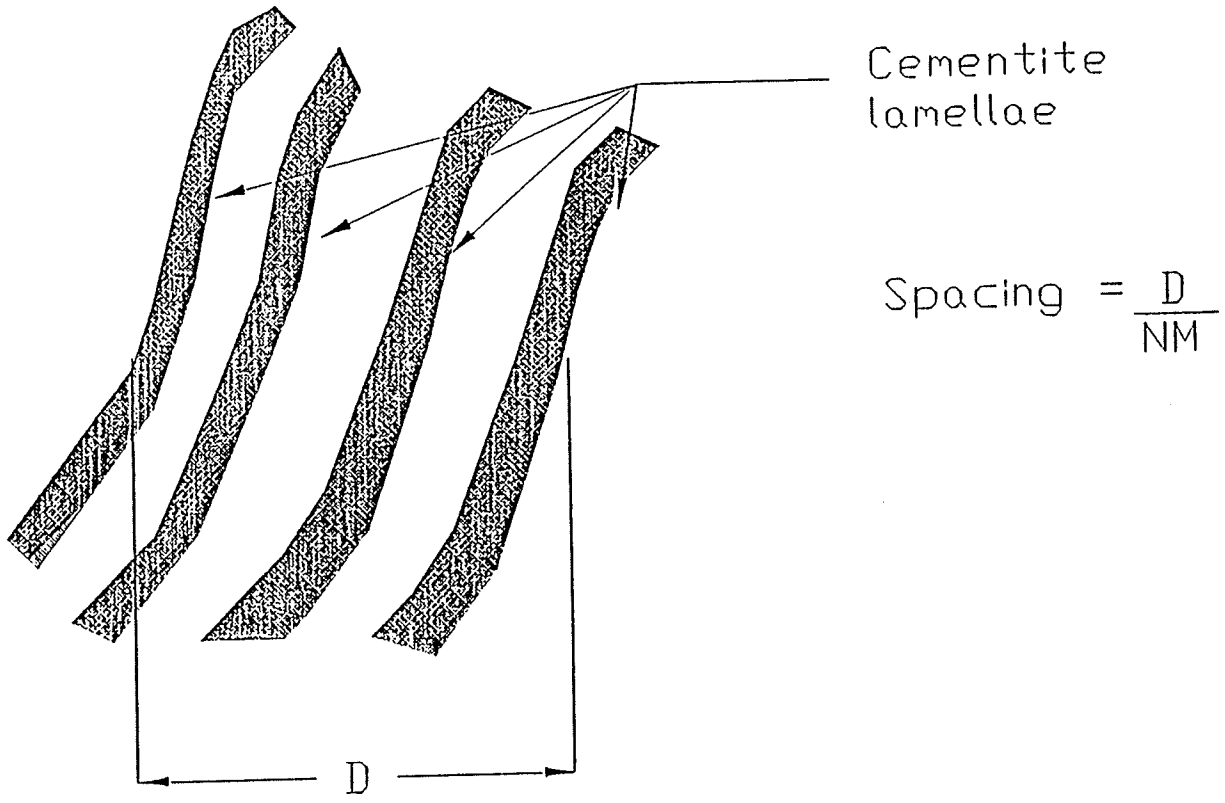

Figure 3.10 Directed spacing method used to determine pearlite interlamellar spacing.

because the SEM is not equipped with a window for light element detection. The presence of oxide inclusions was confirmed from examinations using the optical microscope. According to Samuels [64] oxides are dark and small. Inclusions fitting this description were observed in all four steels.

3.7 An overview of the Experimental Procedure

3.7.1. Characterization of the steels

Metallographic specimens were cut from the untested specimens to characterize the steels structure and to quantify the types of inclusions present and their morphology. The inclusions morphology includes determining the inclusions size, shape and distribution.

3.7.2. Mechanical testing

The first step was to determine the bending strength of the steels. Next, the fatigue behaviour was characterized by subjecting samples of each steel to two different fatigue testing programs. For the first testing procedure the specimen was subjected to a designated schedule of tensile stresses which increase in a stepped pattern. For the second testing program the samples were tested at a constant mean stress. For both testing programs the specimen was tested until crack initiation was detected by an increase in acoustic emission activity.

3.7.3. Observing crack initiation sites

At the termination of the fatigue tests the samples were removed cleaned and if necessary polished for metallographic observation. Preliminary observations were performed on a optical microscope followed by a detailed investigation using a scanning

electron microscope. Using the SEM the details of the crack initiation site were determined, this includes measuring the size and determining the type of inclusion present.

Chapter IV

Experimental Results

4.1 Microstructural Observations

4.1.1 SEM investigation of the rail steels microstructure

Figure 4.1 (a)-(d) shows the fully pearlitic microstructure of each rail steel tested. The plane of observation is parallel to the rail head upper surface. Although it is not evident in Figure 4.1 all of the steels are fully pearlitic. A higher magnification investigation revealed the fine lamellar structure as shown in Figure 4.2 (a)-(d).

In all of the steels tested the pearlite is made of a lamellar structure of ferrite and cementite (Fe_3C). The lamellar structure is generally random in orientation and ordered, ie. alternating layers of ferrite and Fe_3C, see Figure 4.1 and Figure 4.2. However, these steels also contain colonies of pearlite in which the lamellar structure is degenerated, as shown in Figure 4.3 (a)-(d).

The mean inter-lamellar spacing was determined using the directed spacing method outlined in section 3.6.2. The results are presented in Table 4.1. Two methods were used for selecting the colonies to be measured. First, the colonies with the finest lamellar structure, and second a random selection of colonies which covered the entire range within a sample. Using the first selection method, the order in terms of decreasing lamellar spacing is 0.165μm for the steel C, 0.117μm for steel A, 0.109μm for steel B and 0.093μm steel D. The order of the steels remains the same using the second selection method, the results are 0.213μm steel C, 0.184μm steel A, 0.176μm steel B and 0.120μm steel D.

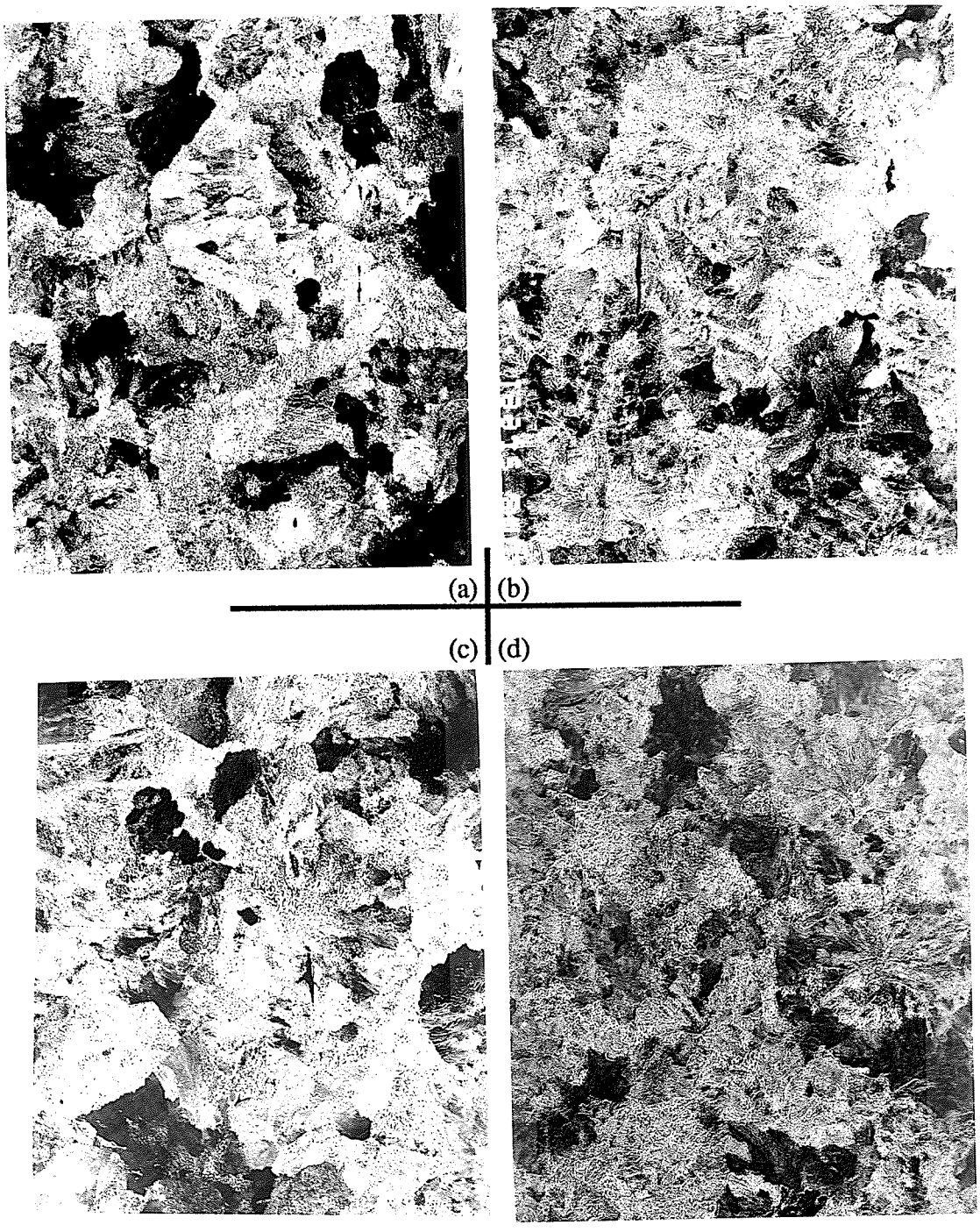

Figure 4.1 Etched Microstructures: (a) Steel A, (b) steel B,

(c) steel C and (d) steel D. (250X)

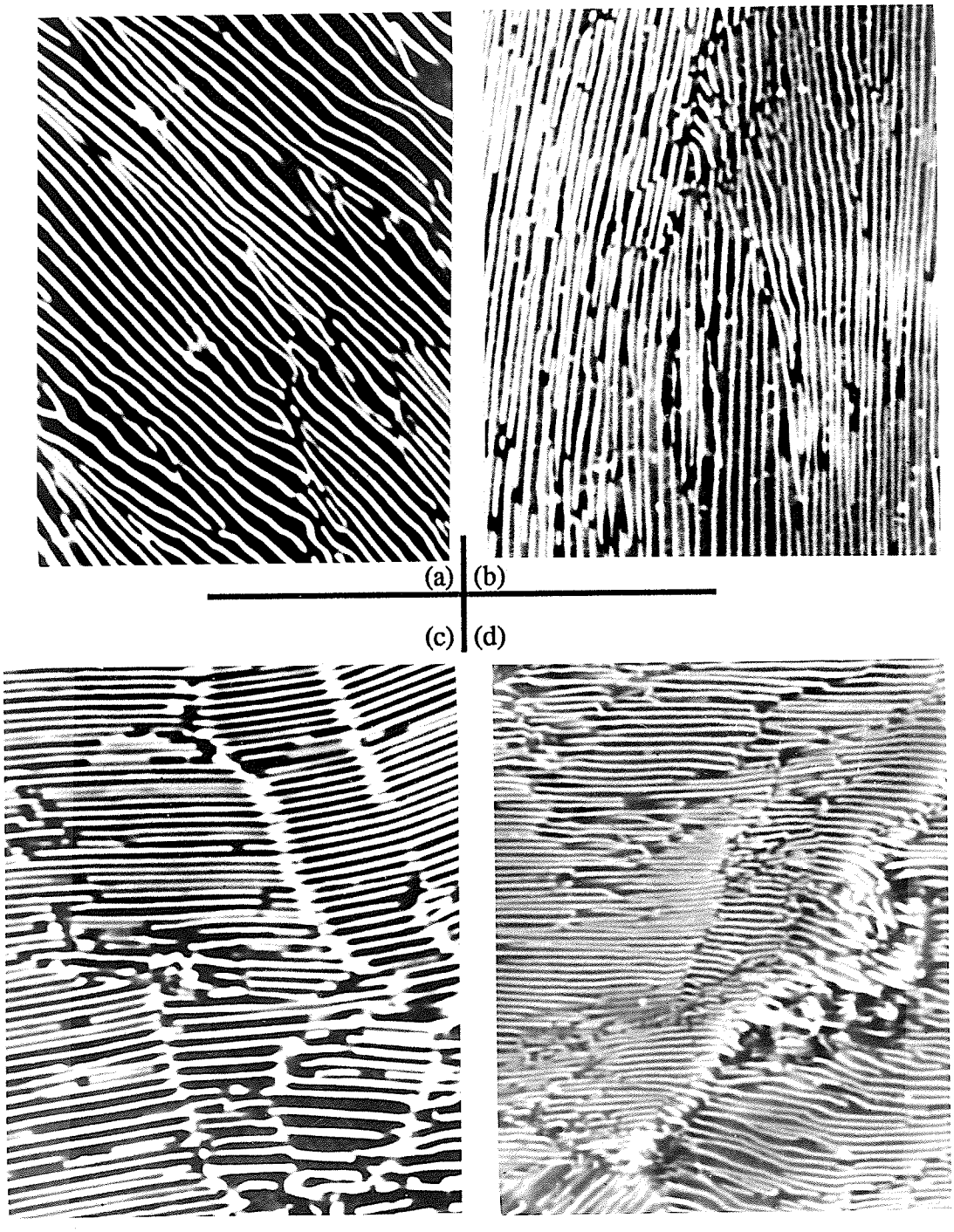

Figure 4.2 Etched Microstructre: (a) Steel A, (b) steel B,

(c) steel C and (d) steel D. (10 000X)

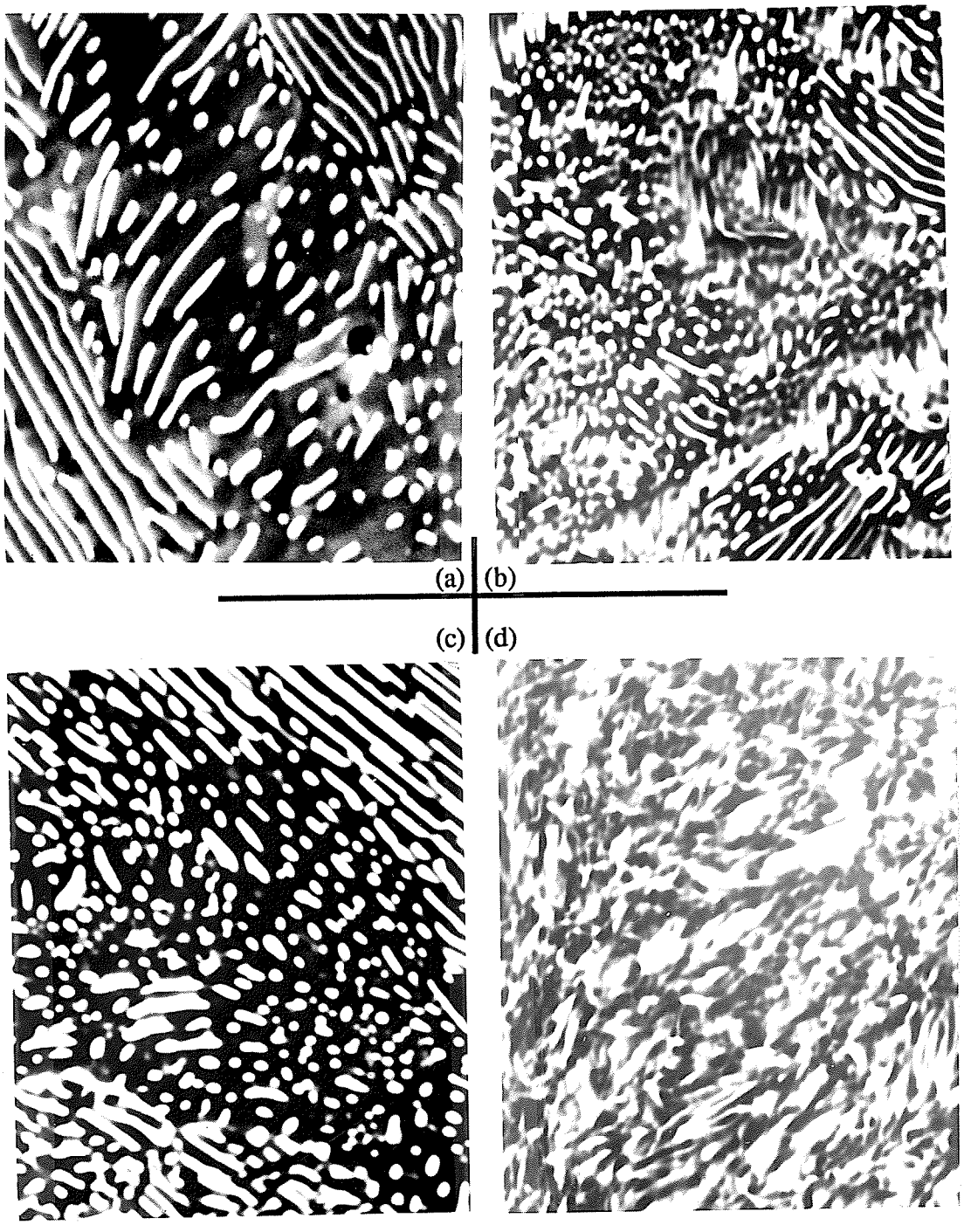

Figure 4.3 Degenerated Pearlite: (a) Steel A,

(b) steel B, (c) steel C and (d) steel D. (10,000X)

Table 4.1 Interlamellar Spacing

Steel type	Random Colony Selection		Colonies with Fine pearlite spacing	
	Mean (μm)	Relative Error (%)	Mean (μm)	Relative Error (%)
A	0.1836±0.065	35	0.1166±0.0142	12
B	0.1765±0.0519	30	0.1093±0.0143	13
C	0.2134±0.1237	58	0.1647±0.0191	12
D	0.1203±0.0408	34	0.0926±0.0093	10

4.1.2 Inclusion Types

The element composition of the inclusions was determined using an energy dispersive X-ray (EDX) analyzer. The system used was restricted because it cannot detect light elements. However, heavier elements which form nonmetallic inclusions were detected. The results of the EDX analysis are summarized in Table 4.2.

Common to all the steels are elongated manganese sulfide (MnS) inclusions. There was a variation in this type of inclusion from steel to steel because of the possible presence of other alloying elements which form a second nonmetallic phase. The second phase is normally restricted to the ends of the inclusion or along the inclusion/matrix interface.

The existence of a second inclusion phase occurs most frequently in steel C. Most of the elongated MnS inclusions in this steel are duplex inclusions with a second phase at the ends of the inclusions, as shown in Figure 4.4(a). Occasionally the second phase surrounds the entire MnS inclusion. In steel C the elements detected in the second phase are Al and Si. This phase was presumed to be formed from a combination of Al_2O_3 and SiO_2. Both of these oxides are common nonmetallic inclusions in steel [62].

In the steel A the number of MnS inclusions with a second nonmetallic inclusion phase was less than in the C steel. The second phase is normally restricted to the ends of the inclusions, as shown in Figure 4.5 (a). The elements detected include Al, Si and Ca. For steel B there were few duplex MnS inclusions, the inclusion/matrix interface was usually free of any second phase, see Figure 4.5(b).

In steel D the MnS inclusions with a second phase along the inclusion/matrix interface were common, see Figure 4.6(a). There also existed an extremely brittle iron and manganese silicate glass inclusion.

These inclusions were normally associated with a MnS inclusion, as shown in Figure 4.6(b). This inclusion contains 41%Al, 19%Si, 19%Fe, 9,5%Mn, 10.5%S and 0.65%Cr in atomic percentage.

Table 4.2 Inclusions in each steel.

Steel	Inclusion	Identification and Comments
A. Steel A	I. Round	1. Aluminum silicates and aluminum oxides 2. The aluminum oxides are most common. Presumed to be Al_2O_3. As shown in Figure 4.5(c) 3. Complex duplex inclusions containing Al,Ca,Mn and S
	II Elongated	1. MnS, see Figure 4.5 (a) 2. Infrequently with a second distinct region containing Al, Si and Ca.
B. Steel B	I. Round	1. Aluminum silicate and aluminum oxides, see Figure 4.5 (d) 2. Complex inclusions containing Al,Si,Mg and Ca
	II. Elongated	1. MnS, see Figure 4.5(b) 2. Most of these inclusions are homogeneous, without any regions containing other elements.
C. Steel C	I. Round	Aluminum oxides, see Figure 4.4(c)
	II. Elongated	A. 1. MnS 2. Most MnS inclusions have regions of high Al and Si concentrations, usually at the ends of the inclusion's long axis, occasionally surrounding the entire inclusion, see Figure 4.4(a) B. 1. Aluminum silicate and duplex inclusions of aluminum oxide and aluminum silicate, see Figure 4.4(b) 2. Elongated in the rolling direction and usually smaller then the MnS inclusions
	III. Angular	1. Silicon oxides, SiO_2 2. Square and larger then the circular oxide inclusions and the elongated Al_2O_3/SiO_2 inclusions, see Figure 4.4(d)
D. Steel D	I. Round	1. Aluminum oxides and Aluminum silicates, as shown in Figure 4.6(c) 2. Other elements detected include Mg, S, Ca and Mn
	II. Elongated	A. 1. MnS, shown in Figure 4.6(a) B. Fe and Mn silicate glass, a brittle phase found at the ends of many of the MnS inclusions, see Figure 4.6(b)
	III. Angular	1. Silicon inclusions, SiO_2, triangular, see Figure 4.7(d).

In addition to the elongated MnS inclusions each steel also contained alumina and alumina silicate inclusions. Alumina silicate inclusions were found in steel D, Figure 4.6(d), in steel A, Figure 4.5(c) and in steel B, Figure 4.5(d). In steel C there were strictly alumina inclusions as shown in Figure 4.4(c).

Unique to steel C were elongated aluminum oxide and aluminum silicate inclusions as shown in Figure 4.4 (b). These inclusions were larger then the aluminum oxide inclusions in the other steels. The EDX analysis shows that these inclusions are composed of aluminum and silicon, they are presumed to be a combination of Al_2O_3 and SiO_2. The weight percentage of aluminum and silicon was the same as the second phase that exists around the MnS inclusions. These inclusions occasionally also contained regions of pure Al.

Generally, hard brittle oxide inclusions are considered far more detrimental to the fatigue performance of steels then formable MnS inclusions [64]. These oxides are considered harder then the matrix because they resist deformation during rolling. However, for these steels it would be incorrect to make any predictions about the influence of the inclusions on the fatigue behaviour of the steels based on their shape. In all of the steels small circular MnS inclusions were found, which are approximately the same size as the circular oxide inclusions. Their existence and the presence of elongated Al_2O_3/SiO_2 inclusions in steel C suggests that there exists a minimum diameter and any inclusions below this size will not be deformed during rolling. The deformation of the inclusion is determined by the area of contact between the inclusion and the matrix. If the contact area is too small, the forces will be insufficient to deform the inclusion [64]. Therefore, it seems incorrect to conclude that the small circular oxide inclusions will be more detrimental to the fatigue performance of the steels because they have retained their shape and resisted deformation during rolling.

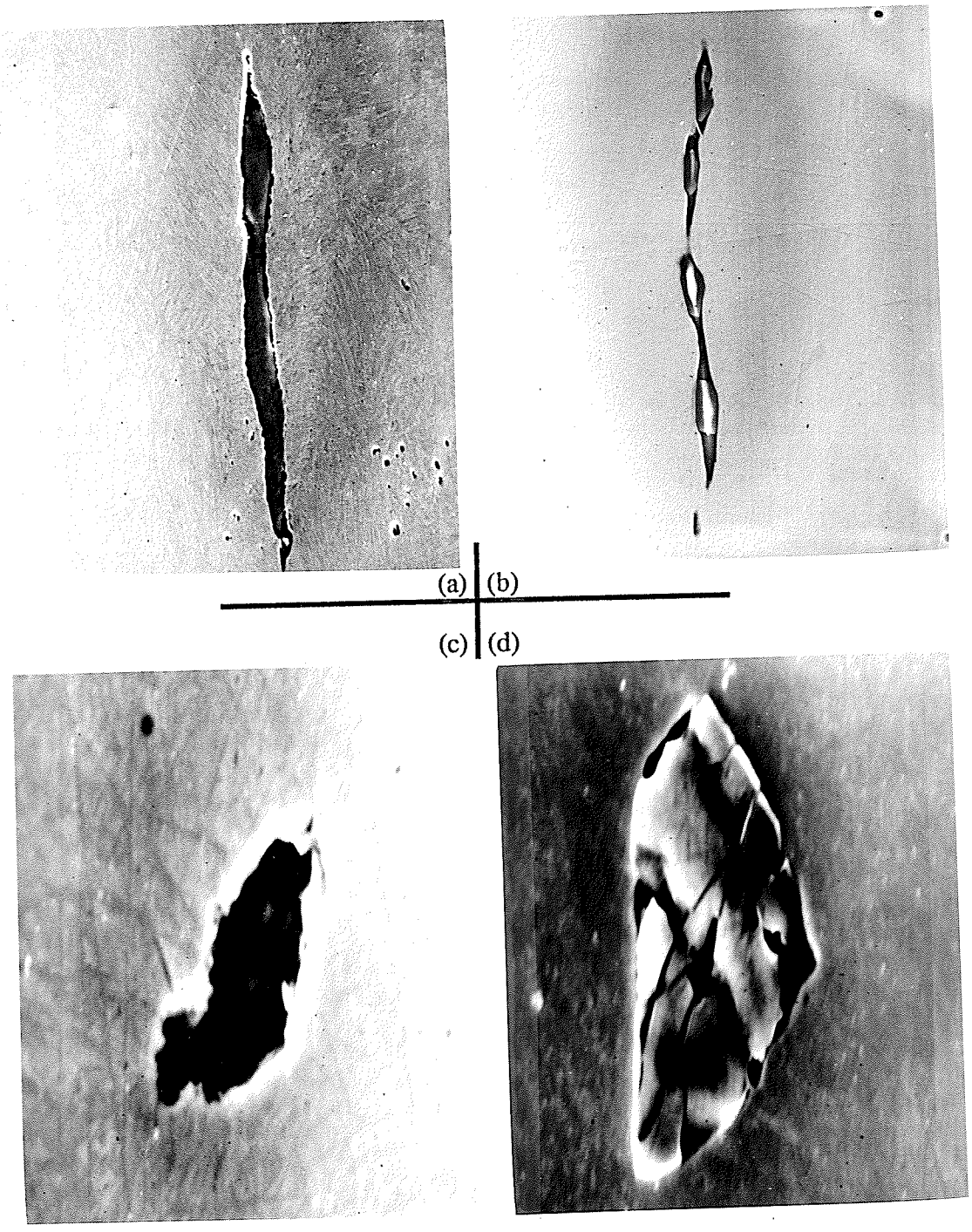

Figure 4.4 Inclusion types in steel C (a) MnS (1000X) (b) Elongated alumina silicate (1000X), (c) Alumina oxide (5000X) and (d) SiO_2 (2500X).

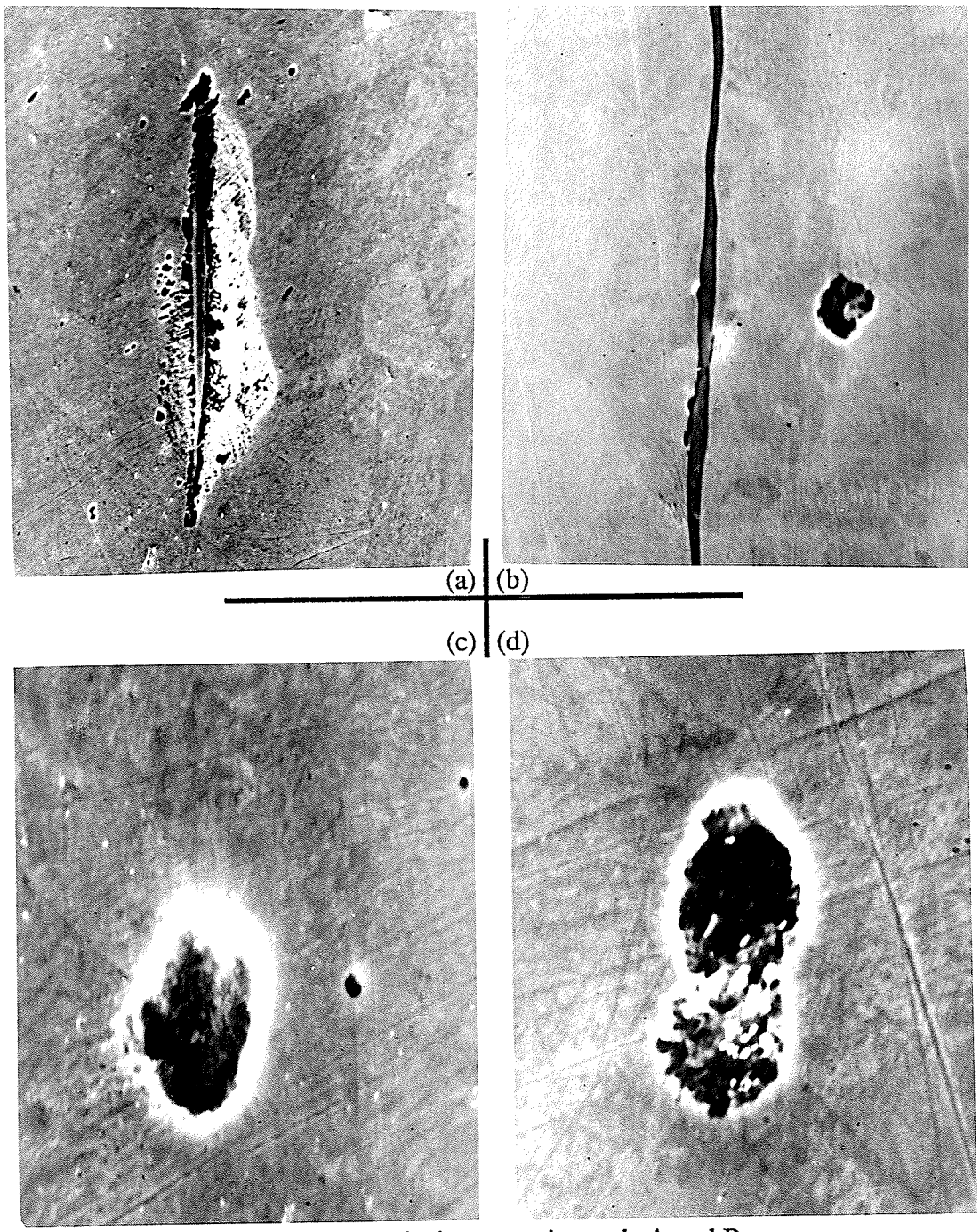

Figure 4.5 Inclusion types in steels A and B:

(a) Steel A MnS (1000X), (b) steel B MnS (1000X), (c) Steel A alumina silicate (5000X) and (d) steel B alumina silicate (5000X).

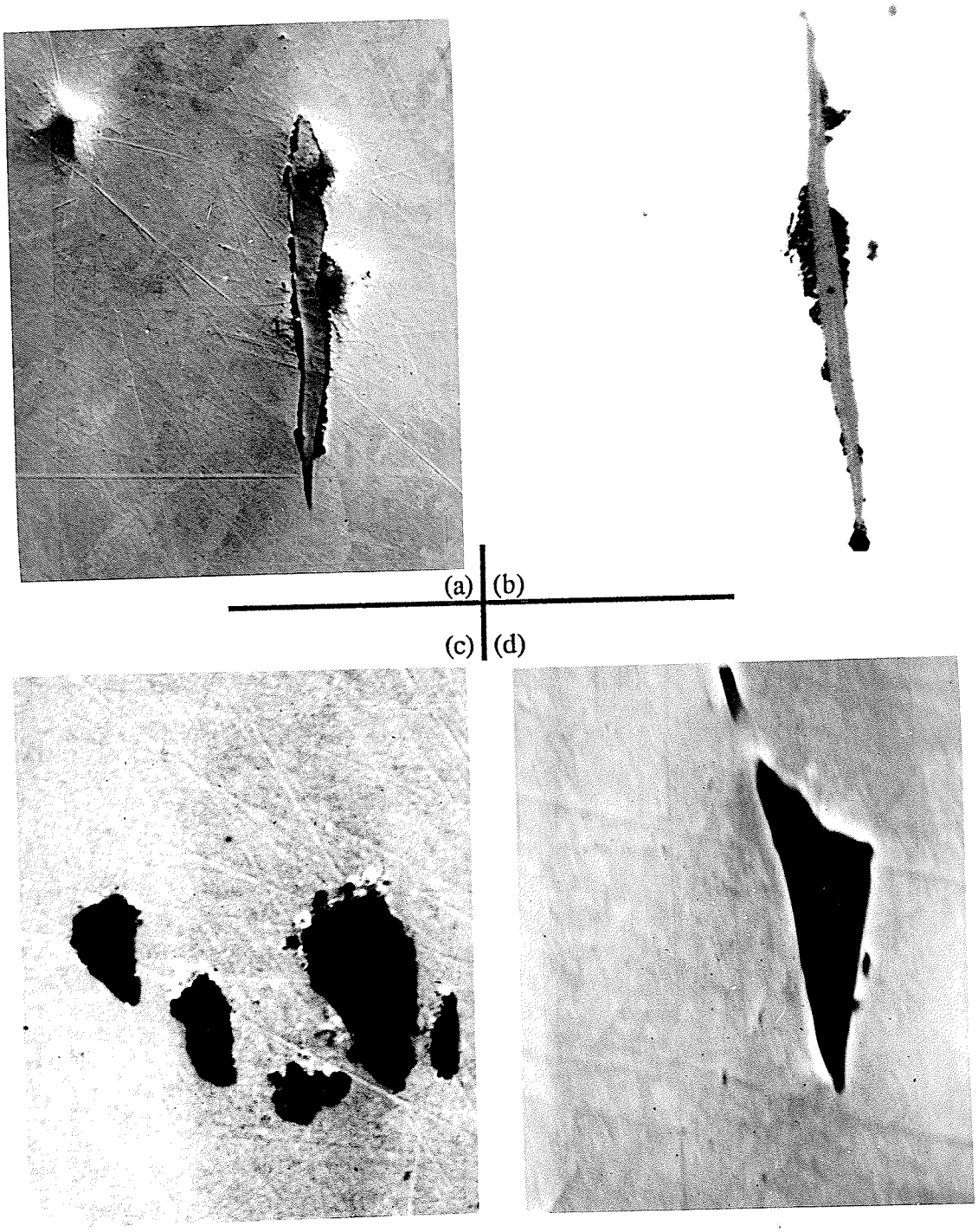

Figure 4.6 Inclusion type in steel D (a) MnS (1000X),
(b) MnS and silicate glass (1000X), (c) alumina silicate (2500X) and (d) SiO_2 (5000X).

Angular silicon inclusions were found only in steels C and D. In steel C these inclusions were square (Figure 4.4(d)) and larger then the triangular silicon inclusions in steel D, (Figure 4.6(d)). The EDX analysis only detected silicon for these inclusions, so their composition was presumed to be SiO_2.

The importance of each inclusion type in influencing the fatigue performance of the steels becomes apparent in the observations of the fatigue crack initiation sites following testing.

4.1.3 Inclusion Morphology

To access the influence of the inclusions on the fatigue performance of each steel the types of inclusions must be determined and their spacing, size and shape must be quantified. This section presents the results of the quantitative metallographic observations of unetched specimens that were performed to describe the inclusion morphology.

The volume fraction of nonmetallic inclusions was determined using the manual point count method described in section 3.6.1. As shown in Figure 3.1 the volume fraction of inclusions was small so a high degree of uncertainty may be attached to these measurements. The results are given in Table 4.3. The total volume fraction of inclusions in the steels in ascending order is 0.347% for steel B, 0.348% for steel D, 0.375% for steel A and 0.576% for steel C. The total volume fraction of inclusions in all the steels except steel C is essentially equal. The variation in inclusion content from region to region within steel C and steel D is also given in Table 4.3. The increase in the total inclusion content is roughly 100% for steel C and 30% for steel D. For both of these steels the increase in the volume percentage of oxide inclusions is considerably greater then the increase in the volume percentage of sulfides when comparing the clean regions to the dirty regions. The increase in the volume percentage of oxides is 44% greater then the increase in MnS inclusions for steel C and 91% greater for steel D.

Steel type	Clean Sample			Dirty Sample			% Change			Combined total		
	Oxide (%)	Sulfide (%)	Total (%)	Oxide (%)	Sulfide (%)	Total (%)	Oxides (%)	Sulfide (%)	Total (%)	Oxide -	Sulfide -	Total -
A	0.2249	0.1459	0.3738	-	-	-	-	-	-	-	-	-
B	0.1973	0.1492	0.3465	-	-	-	-	-	-	-	-	-
C*	0.25	0.1553	0.4053	0.5021	0.2438	0.7459	101	57	103	0.3761	0.200	0.5761
D*	0.1514	0.1487	0.3001	0.2408	0.1558	0.3966	59	5	32	0.1961	0.1523	0.3484

Table 4.3. Volume fration (%) of inclusions in the four rail steels

*These steels have a great variation in their inclusion content within the rail head.

The size and shape of the inclusions was determined using custom software programs run on a Leitz/Tasic automated image analyzer as described in section 3.6.1. Due to the great variation in inclusion content from region to region within the FHH and C steels all the measurements were performed on samples selected from both the clean regions and the dirty regions. The averages from all the samples for all the measurements are given in Table 4.4.

The linear dimensions of the inclusions was determined by the M.C.L. parameter and the feret diameter measurement. The results of both measurements show that the C steel had the largest inclusions. The size of the inclusions, as determined by their M.C.L. in descending order are 5.79 μm for the C steel, 4.89 μm for steel A, 4.58 μm for steel D and 4.51 μm for steel B. As mentioned in section 3.6.1 the M.C.L. measurement is independent of the object's shape.

The maximum feret diameter was used to determine the inclusions maximum dimension. Again steel C was found to have the largest inclusions. The average of the maximum dimension of the inclusions in steel C is 14.6 μm. The values for the other steels in descending order are 10.23 μm for the steel A, 10.06 μm for steel D and 9.65 μm for steel B. To determine the shape of the inclusions the dimension at 90^{o} to the maximum feret diameter was also measured. From the results shown in Table 4.4 steel C was found to have the longest inclusions and the widest. The inclusions average widths in descending order are 7.62 μm for steel C, 6.71μm for steel D, 6.15 μm for steel A and 5.63 μm for steel B.

The shape of the inclusions was also determined by the form factor measurement (F.F.). On average steel D was found to have the most circular inclusions, F.F. = 0.89 followed by steel A, F.F. = 0.88, then steel B, F.F. = 0.87 and finally steel C, F.F. = 0.77. For steels A, B and D the F.F. measurement is essentially equal. Only steel C had a significantly smaller F.F., which indicates that the inclusions in this steel were on average more elongated.

		Area			Form Factor			Mean Cord Length			Max Feret			Feret 90° to Max		
Steel Type	# of	Mean $(\mu m)^2$	Std. Err.	Rel. Err. (%)	Mean	Std. Err.	Rel. Err. (%)	Mean (μm)	Std. Err.	Rel. Err. (%)	Mean (μm)	Std. Err.	Rel. Err. (%)	Mean (μm)	Std. Err	Rel. Err. %
A	293	44.05±34.2	2.0	78	0.88±.22	0.01	25	4.89±1.33	0.08	27	10.23±6.29	0.37	61	6.15±2.11	0.12	34
B	279	38.66±40.7	2.44	106	0.87±.23	0.01	26	4.51±1.64	0.1	36	9.65±6.28	0.38	65	5.63±2.41	0.14	43
C*	526	79.29±99.3	2.5	125	0.77±.22	0.01	29	5.79±2.84	0.07	49	14.63±10.0	0.25	68	7.62±4.62	0.25	61-
D*	356	55.43±270.4	10.1	487	0.89±.23	0.01	26	4.58±3.70	0.14	81	10.06±11.1	0.42	109	6.71±5.37	0.20	80

Table 4.4 Size and shape of measurements of inclusions

* Inclusion dispersion is not even but tends to be clustered.

The area measurement also show that steel C had on average the largest inclusions. The inclusions mean area for each steel are 79.29 μm^2 for steel C, 55.43 μm^2 for steel D, 44.05 μm^2 for steel A and 38.66 μm^2 for steel B. However, the extremely large standard deviation for steel D ($\pm$270.43 μm^2) indicate that this steel may contain the largest inclusions.

In summary, the measurements given in Table 4.4 show the variation in inclusion's size and shape between the different steels tested and the variations within any steel. All the size measurements show that steel B had the smallest inclusions. On average steel C had the largest inclusions but the large relative errors associated with all the measurements of the inclusions in steel D suggest that this steel may have the largest inclusions. The form factor measurements indicates that the inclusions in steels A, B and D were on average more circular then the inclusions in steel C and the F.F. was essentially equal for these first three steels.

The variation in the inclusion parameters between clean and dirty sections of the rail is given in Table 4.5 for steel D and Table 4.6 for steel C. A comparison of the measurements are given in Table 4.7. Referring to Table 4.7, for steel C the largest change was a 162% increase in the number of particles detected. For steel D the number of particles detected increased by 196%. Another significant result was the 170% increase in the average area of the inclusions in steel D and the accompanying 374% increase in the relative error. This result shows a large variation in the size of the inclusions in this steel, which was also substantiated by the large standard deviations for the mean cord length and feret diameter measurements.

Following fatigue testing the specimens were removed and examined to find the crack initiation sites. In addition to determining the types of inclusions which cause crack initiation the dimensions and shape of the inclusions were measured. By using this

Table 4.5: Variation in inclusion measurements within steel D.

	Clean Section			Dirty Section			
Parameter	Mean	Std. Error	Rel. Error	Mean	Std. Error	Rel Error	% Increase
Area $(\mu m)^2$	29.88±36.74	2.73	81	80.97±311.3	13.5	384	170
Form Factor	0.92±0.27	0.02	29	0.86±0.21	0.01	24	6.5
Mean cord Length	3.87±1.07	0.08	30	5.28±4.23	0.18	80	36
Maximum. Feret	8.98±8.77	0.65	98	11.13±11.77	0.51	106	24
Feret 90° to Max.	4.72±1.71	0.13	36	7.26±6.13	0.27	84	54

Table 4.6: Variation in Inclusion measurements within steel C.

	Clean Section			Dirty Section			
Parameter	Mean	Std. Error	Rel Error	Mean	Std. Error	Rel. Error	% Inc increase
Area $(\mu m)^2$	71.07±80.26	5.33	113	87.51±105.4	3.1	120	23
Form Factor	0.72±0.26	0.02	36	0.82±0.21	6.01	26	14
Mean Cord Length	5.23±1.88	0.12	36	6.35±3.15	0.08	50	21
Maximum. Feret	15.52±11.70	0.78	75	13.74±9.43	0.27	69	-11
Feret 90° to Max.	6.63±2.57	0.17	39	8.61±5.29	0.14	61	30

Table 4.7: Change in the mean and relative error of the inclusion morphology parameters when comparing the averages from the clean and dirty sections.

	% Change in the Mean Values		% Change in the Rel. Errors	
	steel C	steel D	steel C	steel D
# of Inclusions	162	196	-	-
Area $(\mu m)^2$	23	170	6	374
Form Factor	14	-6.5	-28	-17
Mean Cord Length (μm)	21	36	39	17
Maximum Feret (μm)	-11	24	-8	82
Feret 90° to Max (μm)	30	54	30	133

Table 4.8: Measurements of critical inclusions*.

Steels	Area $(\mu m)^2$	Form Factor	Mean Cord Length (μm)	Max. Feret (μm)	Type of Inclusion
A	50	0.5	3.7	20	MnS
B	30	0.75	2.5	12	MnS
C	50	0.5	3.5	15	MnS
D	25	0.5	3.5	25	duplex MnS and glass

* Based on the dimensions and shape of the inclusions which caused crack initiation. The area M.C.L and maximum feret diameters are minimum values and the form factor is a maximum.

Steel Type	Area			Form Factor			Mean Cord Length			Max Feret		
	Mean $(\mu m)^2$	Std. Err.	Rel. Err. (%)	Mean	Std. Err.	Rel. Err. (%)	Mean (μm)	Std. Err.	Rel. Err. (%)	Mean (μm)	Std. Err.	Rel. Err. (%)
A	85.93±32	3.37	37	0.40±.06	0.01	15	5.35±1.20	.08	22	25.78±4.70	0.90	18
# of inclusions	90			26			198			27		
B	69.28±51.54	4.93	74	0.55±.14	0.02	25	4.96±1.76	0.12	35	18.60±6.65	0.81	36
# of inclusions	109			74			198			68		
C	147.6±127.0	5.88	86	0.37±.09	0.01	24	6.73±3.03	0.09	45	24.88±10.29	0.62	41
# of inclusions	290			52			602			171		
D	95.75±115.4	6.97	121	0.35±.11	0.02	31	6.06±4.84	0.25	80	48.41±30.64	2.38	63
# of inclusions	274			29			378			27		

Table 4.9: Results after removing ineffective inclusions.

procedure the dimensions and shape of the smallest inclusion that was found to initiate cracks were determined. The dimensions and shape of these inclusions were used as critical values to tailor the inclusion morphology measurements. The size of the critical inclusions was used as a minimum value, below which all inclusions are considered ineffective crack initiators and could therefore be eliminated from the statistical study. The F.F. of the most circular inclusion found at a crack initiation site was used as an upper limit. The critical dimensions based of the smallest and most circular inclusions are given in Table 4.8. For steels C and the measurements from the dirty specimens were selected and tailored, the results are given in Table 4.9. The change in the inclusion measurements following the elimination of the ineffective inclusions is given in Table 4.10.

Following the elimination of the ineffective inclusions certain characteristics of the remaining inclusion population were apparent; First, steel B had the smallest and most circular inclusions, second steel C had the largest inclusions and third the inclusions in steel D were the longest and most elongated.

As expected narrowing the range of interest resulted in a considerable reduction of the standard deviation associated with each mean. This was reflected in the improvement in the relative errors, listed in Table 4.10. Just how much the statistical population was reduced is shown by the percentage of inclusions accepted once the limits were applied, the results are given in Table 4.10. For example, the results in Table 4.10 show that only 16% of the inclusions in steel D had a dimension greater then the critical dimension. The elimination of the remaining 84% of the inclusions increased the maximum feret diameter by 350%.

The spacing between inclusions was determined by calculating the mean free path, λ_i, using equation 3.7. The mean cord length measurements are from Table 4.4 and the volume fraction measurements are from Table 4.3. The combined results for steels D and C were used in Equation 3.7. The results are given in Table 4.11. Except for steel C there was little variation in the calculated mean free path values between different steels. The

Table 4.10: The change in inclusion parameters following the elimination of ineffective inclusions. The dirty section is used for comparison.

Inclusion Parameters	% of inclusions accepted	% change	Improvement in the rel. error	Steel Types
Area	31	95	53	**A.**
	39	44	30	**B.**
	43	68	28	**C.**
	52	18	70	**D.**
Form Factor	8.9	-55	40	**A.**
	27	-37	4	**B.**
	7.7	-55	7.7	**C.**
	5.5	-59	29	**D.**
Mean Cord Length	76	9	19	**A.**
	71	10	46	**B.**
	89	6	34	**C.**
	71	13	27	**D.**
Maximum Feret	9.2	60	71	**A.**
	24	48	46	**B.**
	25	81	41	**C.**
	5	350	41	**D.**

Table 4.11: Mean free path between inclusions

Steel Type	Mean Cord Length (μm)	Volume Fraction (%)	Mean free path λ_i (mm)
A	4.89	0.3748	1.3
B	4.51	0.3465	1.27
C	5.79	0.5761	1.0
D	4.58	0.3484	1.31

values are 1.0 mm for steel C, 1.27 mm for steel B, 1.3 mm for steel A and 1.31 mm for steel D.

4.1.4 Pearlitic Structure Following Shot Peening

To observe the effects of the shot peening on the rail steel's pearlitic lamellar structure, samples for metallographic observation were prepared as outlined in section 3.2.4. The pearlite structures are shown in Figure 4.7 for all four steels. All the photographs show the shot peened surface and the immediate subsurface layers. Evidence of the shot peening is displayed by the deformed pearlite in the vicinity of the upper surface. Close to this surface the pearlite is curved and bent away from its original orientation. Such a deformation of the pearlitic structure introduces compressive residual stresses into the material in the region neighboring the shot peened surface. During the fatigue testing the shot peened surface was held in tension, so that this surface had a tensile stress component due to the testing and a residual compressive component due to the shot peening.

4.2 Properties Evaluation

The initial mechanical tests were performed to characterize the mechanical properties of each steel. Following material characterization two different fatigue tests were performed to determine the fatigue behaviour of each rail steel.

4.2.1 Strength and Hardness Measurements

The bending strength of each steel was determined using the procedure outlined in section 3.3.1. The bending proof strength was defined as the stress at which there is a permanent strain of 0.01% in the outer fiber of the sample. The deflection, δ_p, which produces this permanent strain is determined by equation 3.2. The load which

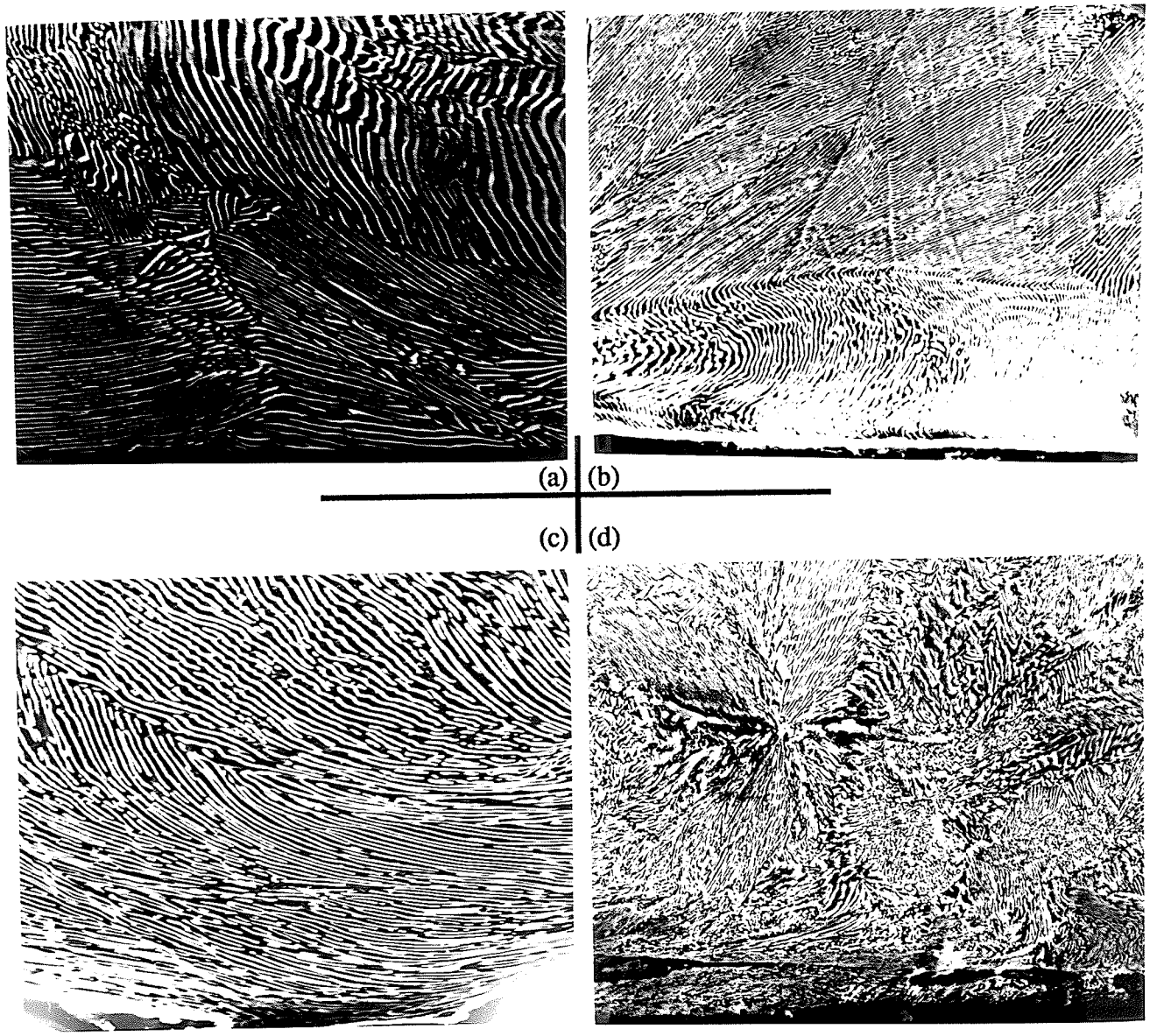

Figure 4.7 Deformed pearlite at the shot peened surface and immediate subsurface layers,

(a) Steel A (b) steel B (c) steel C (d) steel D. (2500X)

corresponds to this deflection was determined from the load-deflection curves for each steel. The deflection was measured at the centre of the specimen. The bending strength or proof stress, σ_p, was determined using equation 3.1. The results of the bending strength calculations are given in Table 4.12.

The hardness of the rail steels was measured in Rockwell C scale as described in section 3.3.1. The results of the hardness measurements are given in Table 4.12.

The strengths of the steels tested ranged from 510 MPa for steel C to 760 MPa for steel D. The hardness measurements had a similar trend, the C steel had the lowest hardness at 24 HRC and the FHH steel the greatest at 38 HRC. There was no difference in the hardness and strength measurements of steels A and B. Both had a bending strength of 630 MPa and a hardness of 31 HRC.

4.2.2 Ramp Mean Stress Fatigue Testing

The experimental procedure for the step mean stress tests was given in section 3.3.3 and was repeated for three specimens from each rail steel in both the unpeened and the shot peened conditions. The results are given in Table 4.13. The averages for each steel and the improvement in the fatigue performance with shot peening are given in Table 4.14 and the averages are displayed in Figure 4.8.

For the unpeened specimens steel C had the best fatigue performance followed by the steel B, steel A and finally steel D. The order remains the same for the shot peened surface condition. For steels A and D the shot peening resulted in at least a 35% increase in the cycles to crack initiation. Surprisingly, for steel C there was little improvement in the materials fatigue resistance following shot peening. For the steel B the shot peening resulted in a 17% increase in the number of cycles to crack initiation if the unpeened fractured specimen was disregarded. When the fractured specimens were disregarded there was close agreement between the three specimens tested for each steel in each surface condition.

Table 4.12: Hardness and yield strength of the steels

Steel type	R_c Hardness Value	$\sigma_{y(MPa)}$
	31	630
A		
B	31	630
C	24	510
D	38	760

Table 4.13: Cycles to crack initiation during step testing.

	Unpeened		Peened	
	Total Cycles	Final Load (σ_y of steel C)	Total Cycles	Final Load (σ_y of steel C)
A	428 000	100	580 000	120
	457 000	100	605 000	140
	450 000	100	630 000*	140
B	515 000	120	580 000	120
	535 000	120	610 000	140
	724 000	100	657 000	140
C	605 000	140	590 000	120
	622 000*	140	637 000	140
	574 000	120	650 000	140
D	415 000	100	558 000	120
	431 000	100	522 000	120
	405 000	100	646 000	140

* Specimen fractured.

Table 4.14: Averages of the three samples tested for each steel with both surface conditions.

Steel Type	Average Cycles to crack initiation		
	Unpeened	Peened	% Increase
A	445 000	605 000	36
		593 000	
B	591000	616 000	4
	525000*		
C	600 000	626 000	4
	590 000		
D	417 000	575 000	38

* Without the fractured sample.

4.2.3 Constant Mean Stress Fatigue Testing.

To more fully characterize the fatigue performance of each rail steel samples were tested at a constant mean stress until crack initiation. The results are presented by a plot of stress S against the number of cycles to initiation N. The results of all the tests are shown in Figure 4.9 through to Figure 4.12. A comparison of all four steels in the unpeened condition is shown in Figure 4.9 and for the peened condition in Figure 4.10. A comparison of the effect of shot peening on the fatigue performance of each steel is shown in Figure 4.11 and Figure 4.12.

The best fatigue characteristics of any of the rail steels in the unpeened condition was for steel C, see Figure 4.9. The fatigue performance of the remaining steels in descending order is, B, A and D. The improved resistance to crack initiation of steel C was most evident at intermediate stress levels, ($40 \leq \sigma \leq 80\%$). At high and low stress levels the difference in the fatigue performance between each of these steels is smaller in comparison. At the lowest stress level, ($\sigma = 20\%$), all of the rail steels reached the upper limit of testing, ie. $N = 10^7$. At the low stress levels there was little difference in the cycles to crack initiation for the two best steels, B and C. However, at the higher stress levels the performance of steel C was noticeably better, see Figure 4.9.

The better fatigue performance of steels C and B compared to the other two rail steels was reflected by their higher fatigue limits. For both of these steels their fatigue limit was close to $\sigma = 40\%$. Steel D had the lowest fatigue limit, $= 20\%$ and the fatigue limit of steel A was slightly lower than 40%.

Steel C did not have the best fatigue performance of the shot peened specimens, see Figure 4.10. Due to the scatter in the results it was difficult to determine which steel had the best fatigue performance. The only quantitative observation that could be made was that steel D had the poorest fatigue resistance. The performance of the other three steels was closely matched, see Figure 4.10.

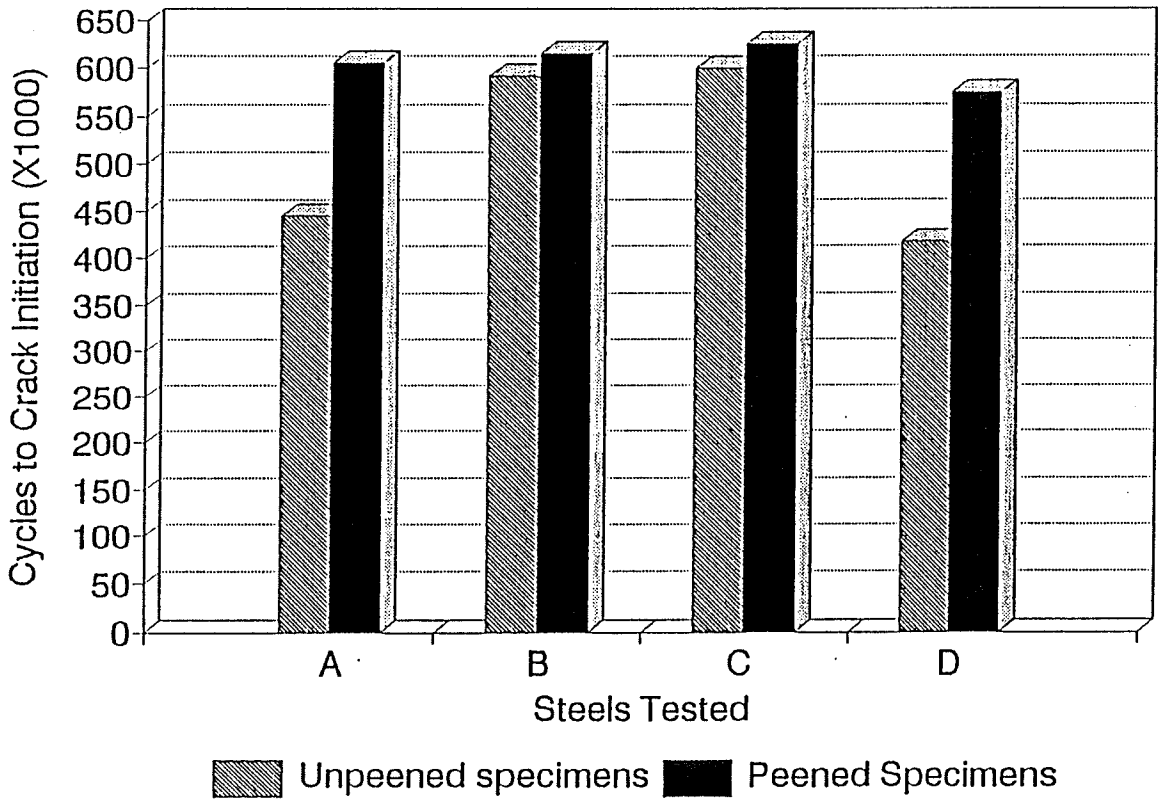

Figure 4.8 Average number of cycles to crack initiation for steels tested using the step mean stress pattern.

The improvement in the fatigue performance of the steels following shot peening was shown by the increase in the fatigue limit for each steel, except for steel D. Following shot peening the fatigue limit for steel B had risen from 40% to 60%. The fatigue limits of steels A and C had also risen above 40%.

The effects of shot peening on the individual fatigue performance of each rail steels is shown in Figure 4.11 for steels A and B and Figure 4.12 for steels C and D. The fatigue performance of each steel was improved by shot peening. This was most clearly demonstrated by the results for steels A and B. For steel C shot peening raises the fatigue limit and improves the resistance to crack initiation in the intermediate range. At high stresses the shot peening appeared to have little influence on the fatigue performance of this steel, as shown by the converging lines in Figure 4.13 (a). Shot peening improved the fatigue performance of steel D but there was a great deal of scatter in the results, see Figure 4.13 (b).

4.3 Acoustic Emission Results

4.3.1 Introduction

During the fatigue testing, the acoustic emission activity was monitored to detect the moment of crack initiation. Crack initiation was assumed to correspond to a substantial increase in acoustic emission activity. Ideally the acoustic emission activity should increase continually with crack growth. Therefore, the moment of crack initiation is simply the beginning of a continual increase in acoustic emission activity. To monitor crack growth the most commonly used acoustic emission parameter is the count rate, which was used for these experiments. The following sections present the acoustic emission results from typical tests. The results are confined to just steels C and D.

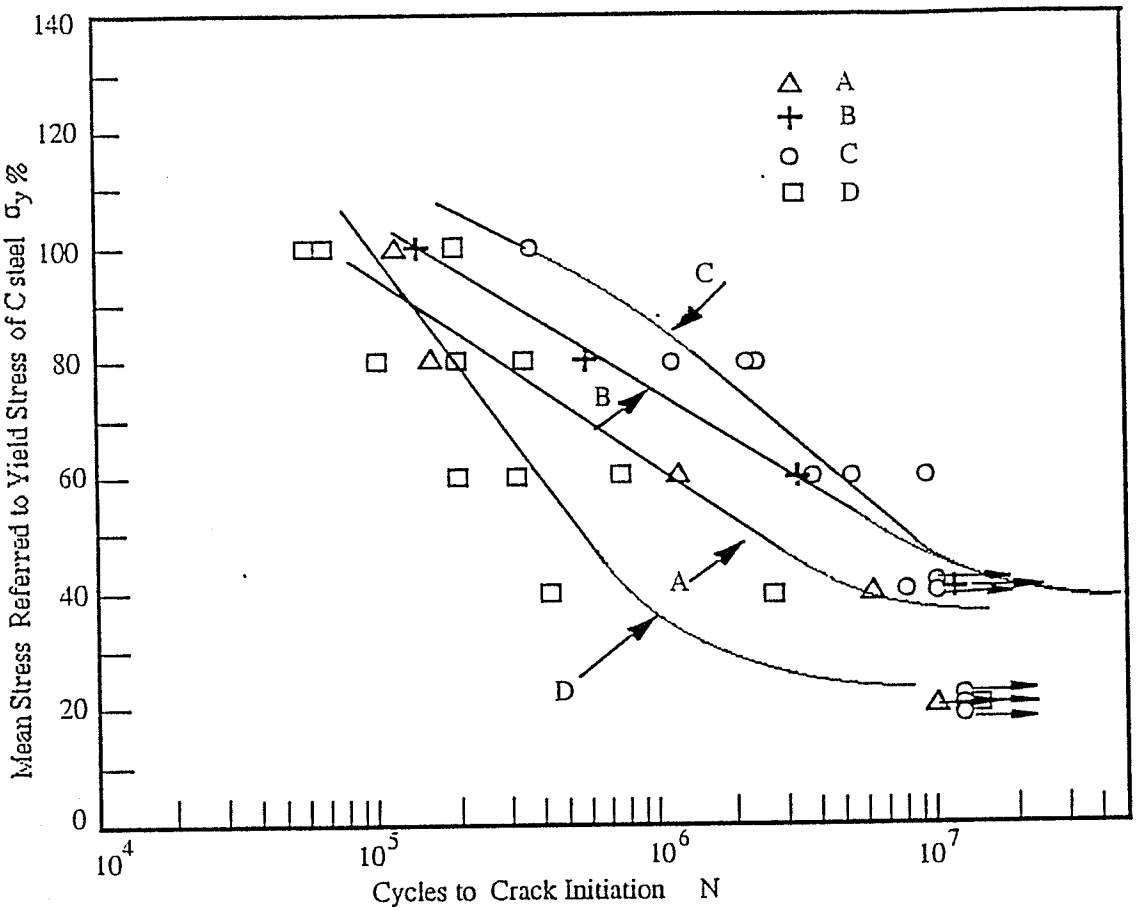

Figure 4.9: Results from the S-N tests of unpeened specimens for all four steels

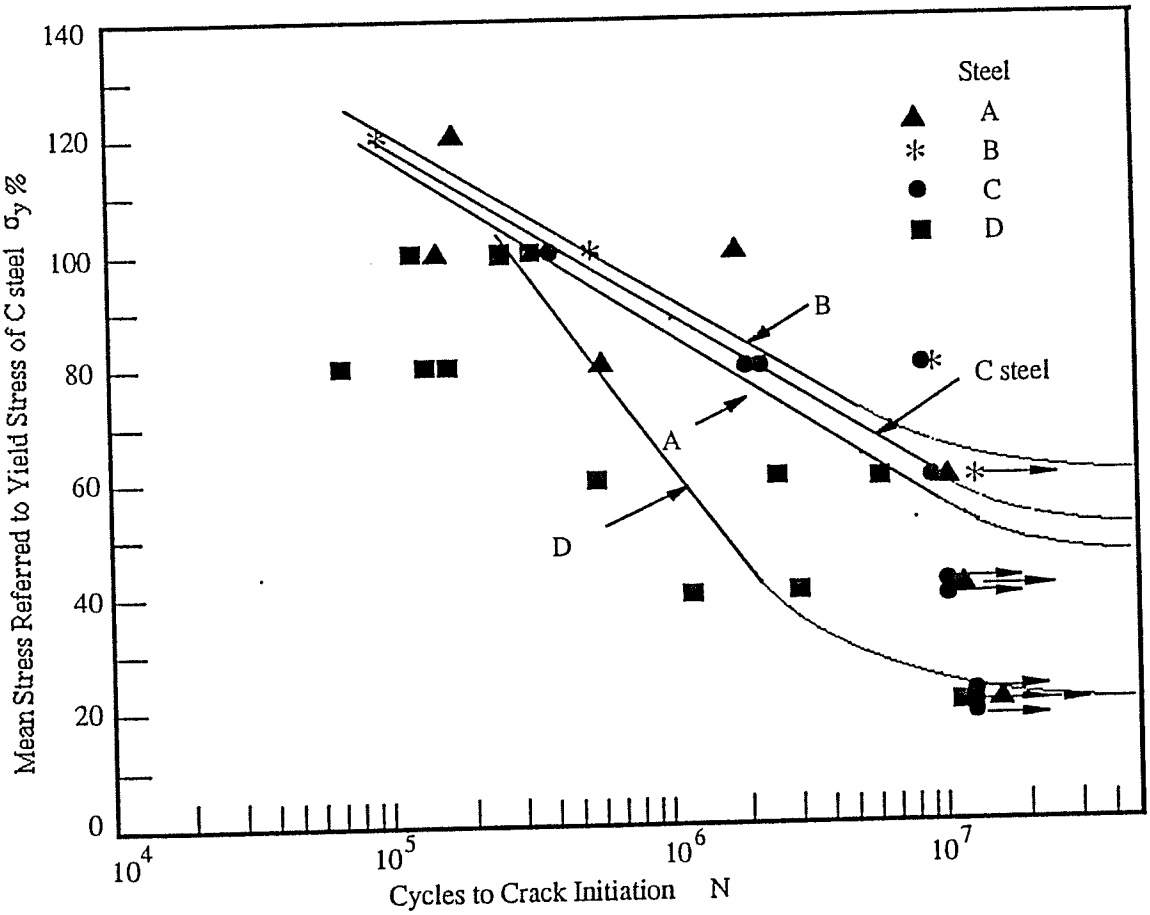

Figure 4.10: Results from S-N tests of peened specimens for all four steels

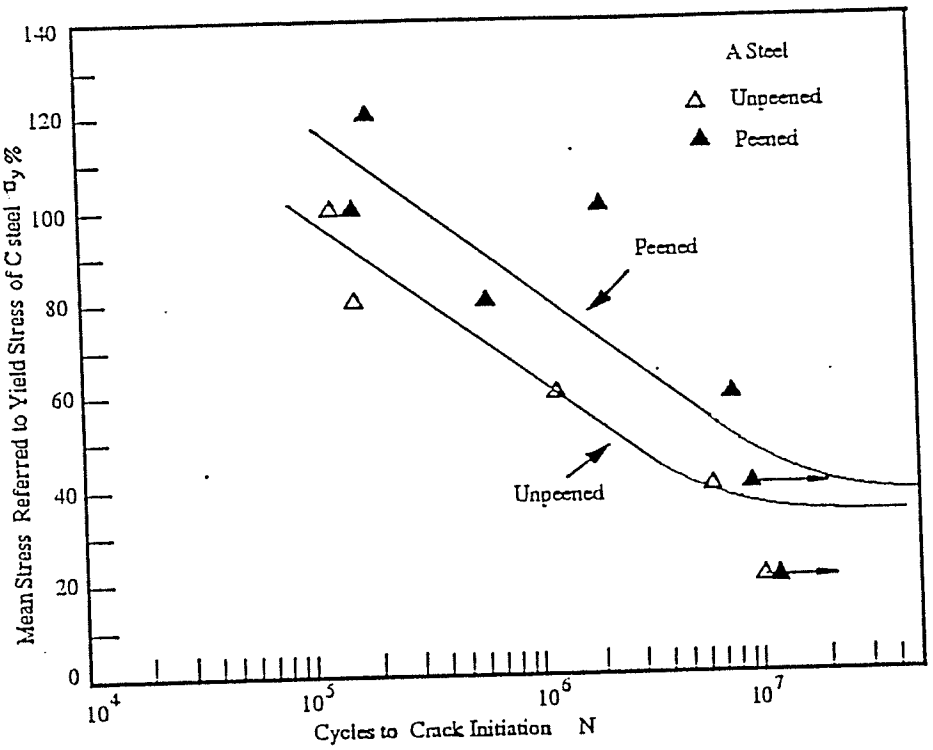

(a)

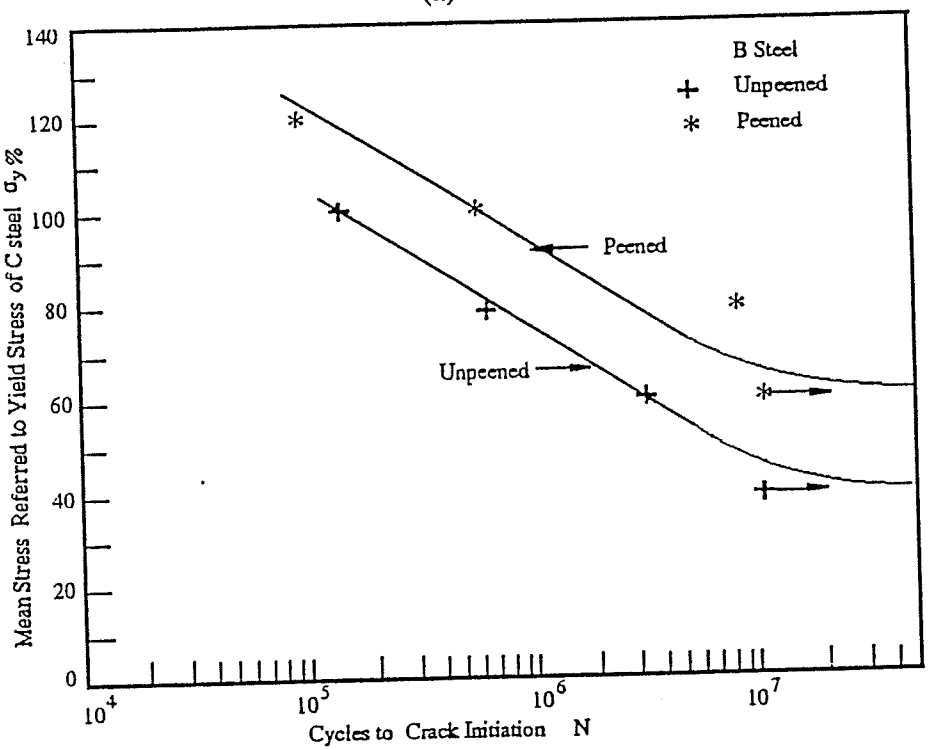

(b)

Figure 4.11: The comparative fatigue results from S-N tests on peened and unpeened specimens of (a) Steel A and (b) Steel B.

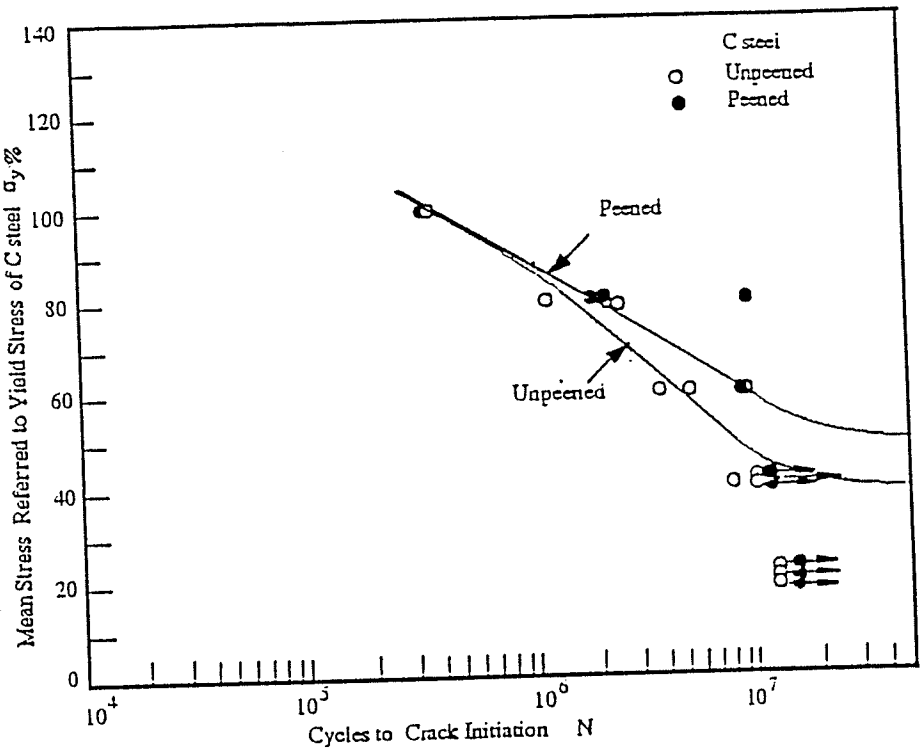

(a)

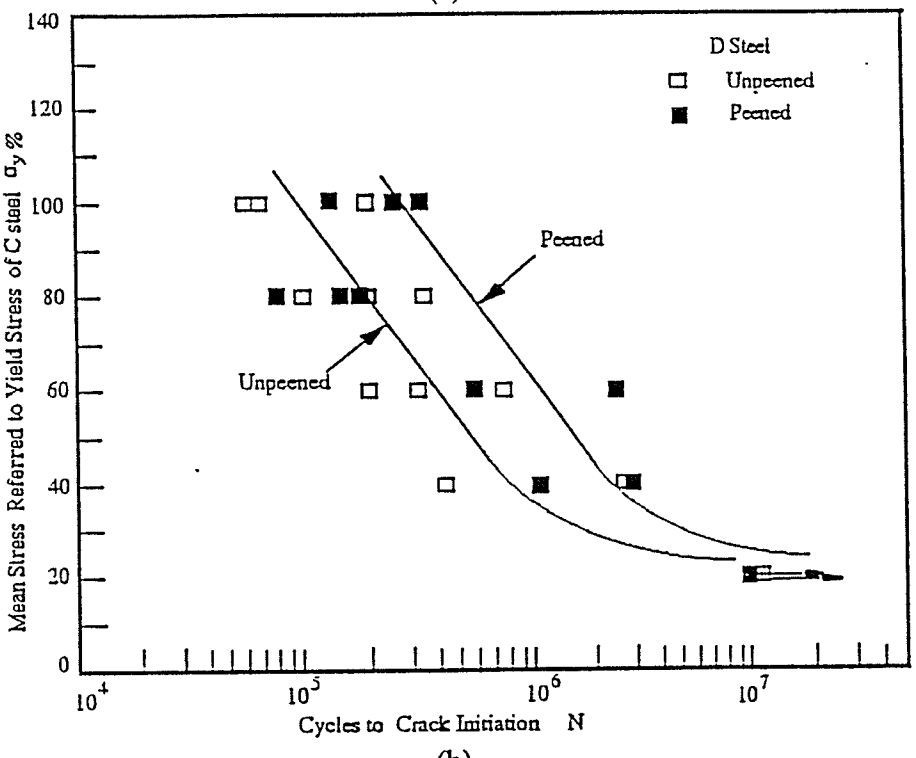

(b)

Figure 4.12: The comparative fatigue results from S-N tests on peened and unpeened specimens of (a) steel C and (b) steel D.

4.3.2 Steel C, Ramp Test, Peened and Unpeened Samples.

Results of the count rate monitoring for an unpeened sample of steel C are shown in Figure 4.13, three stages of the test are shown. Common to most of the samples of steel C during step loading was a gradual increase in acoustic emission activity at low stress levels (ie, 20% or 40%), see Figure 4.14 (a). However, this increase did not indicate fatigue crack initiation, as confirmed by metallographic examination. At higher loads the acoustic emission activity usually stabilized or slightly decreased, as shown in Figure 4.13 (b). Also common to most of the tests at intermediate loads was a substantial increase in activity immediately following the increase in the mean stress level. The eventual initiation of a fatigue crack and the corresponding increase in acoustic emission activity are shown in Figure 4.13 (c).

Similarities between the results for unpeened and peened specimens can be seen by comparing Figure 4.13 and Figure 4.14. Figure 4.14 shows the counts per interval at three mean stress levels, 40%,60% and 120%, for one sample. The results from the tests for both surface conditions show a decrease in the count rate activity at intermediate stress levels, as shown in Figure 4.14 (b). The substantial and continually rising count rate activity at high loads, Figure 4.14 (c) corresponded to the initiation and propagation of a fatigue crack.

4.3.3 Steel C, S-N Tests, Peened and Unpeened Samples.

The increase in acoustic emission activity with the initiation of a fatigue crack was more clearly defined for the results from tests at constant mean stress levels. The complications introduced into the experiment resulting from the increasing stress levels were eliminated and the test were simply run continuously until crack initiation. The results of the acoustic emission monitoring were most effective in detecting crack initiation at low to moderately high stress levels, ie., any test where $\sigma_m \leq 100\%$. At the highest stress levels the vibration of the specimens surface sometimes obscures crack initiation.

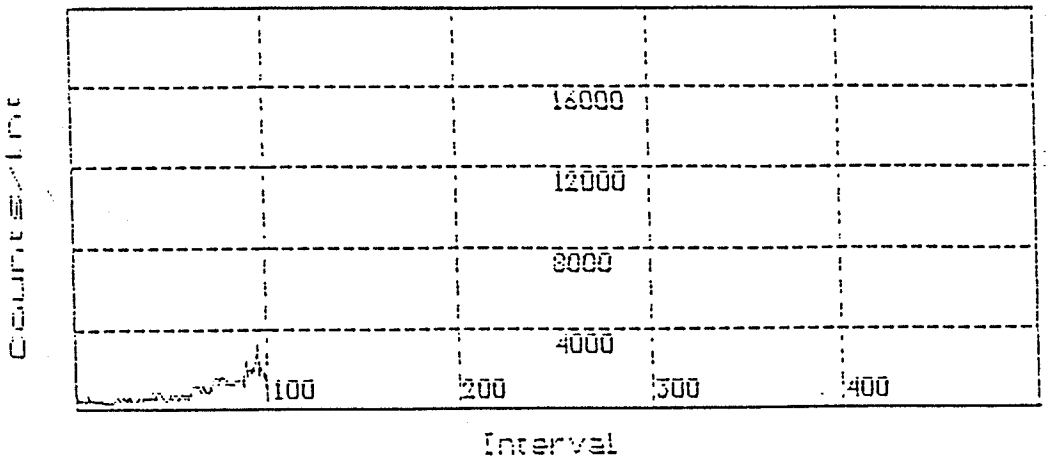

(a)

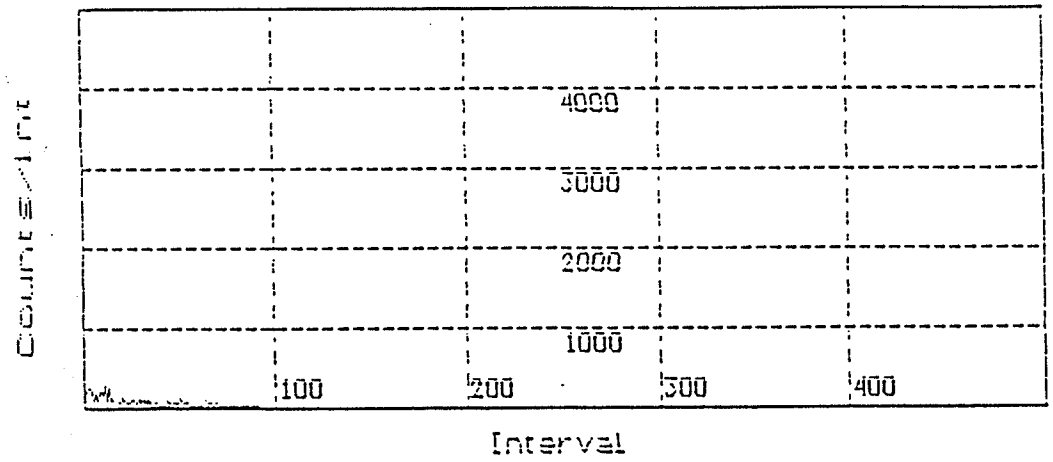

(b)

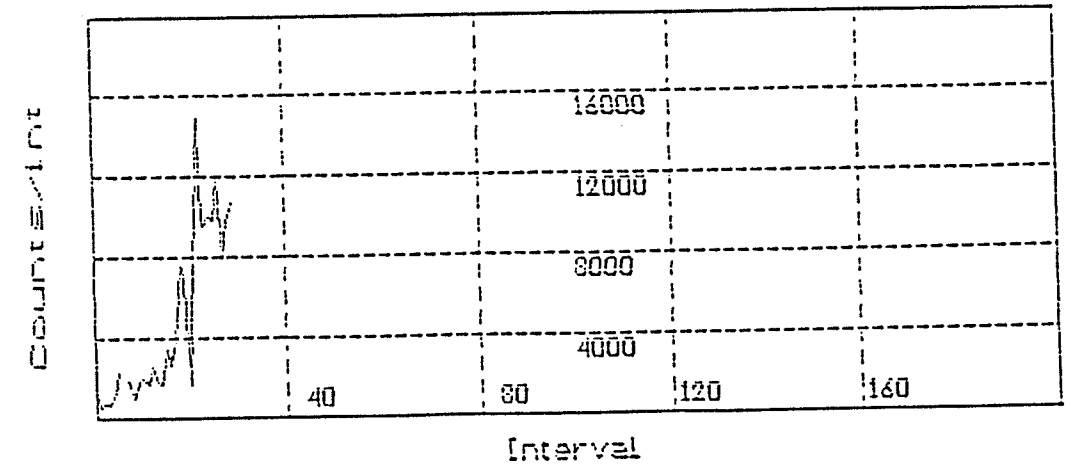

(c)

Figure 4.13: Acoustic emission activity during ramp mean stress level testing of an unpeened steel C sample, (a) 40%, (b) 60% and (c) 120%

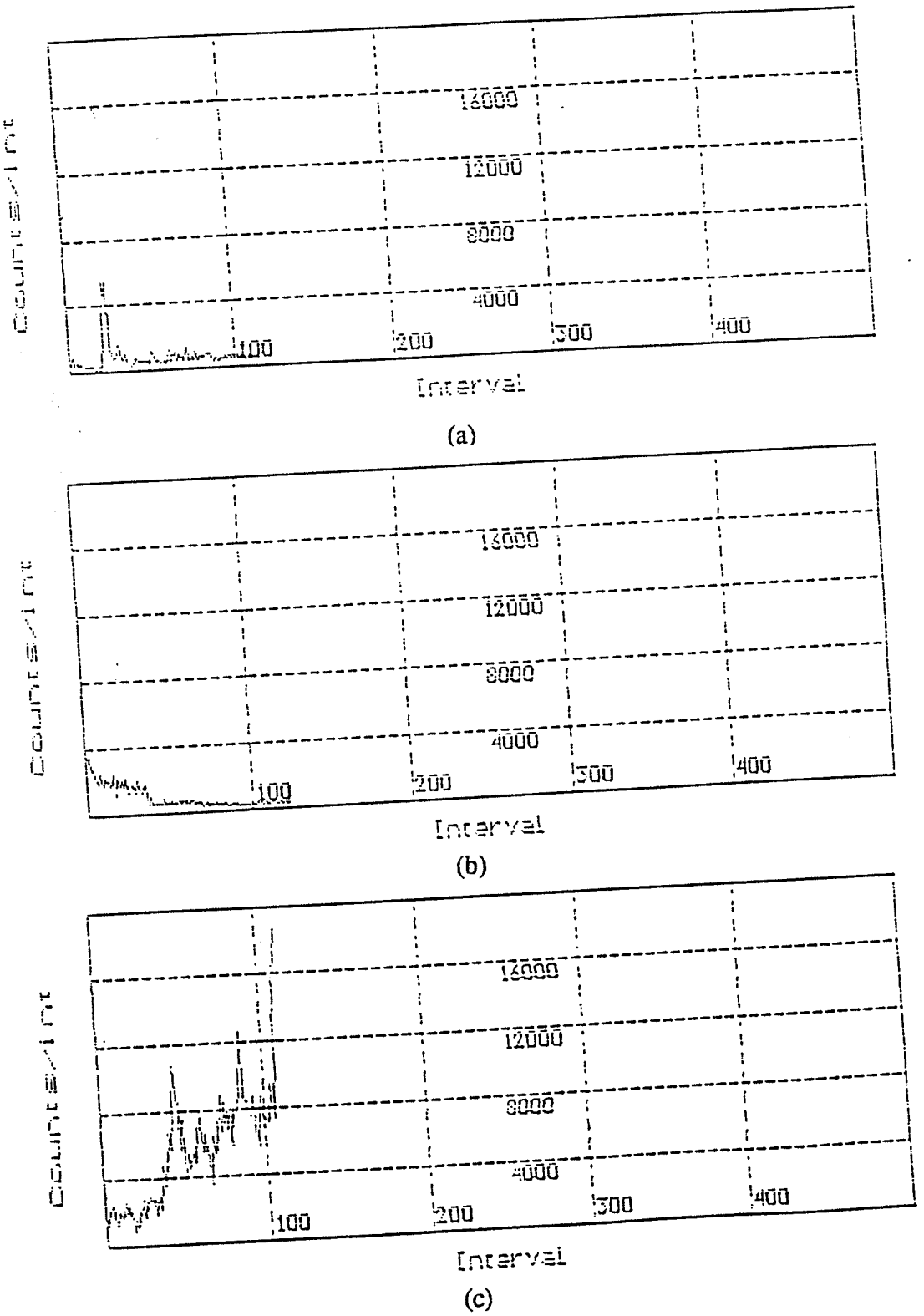

Figure 4.14: Acoustic emission activity during ramp mean stress level testing steel C,(a) 40%, (b) 60% and (c) 120%.

The acoustic emission activity during constant mean stress tests for unpeended and peened specimens are shown in Figure 4.15 and Figure 4.16 respectively. The unpeened specimen was tested at a mean stress of 80%. The point of crack initiation is clearly shown in Figure 4.15(b), the steady acoustic emission activity before crack initiation is shown in Figure 4.15(a). Two different examples for peened specimens are shown in Figure 4.16. The point of crack initiation was evident for the specimen tested at the higher load, Figure 4.16 (a), but the results were not as conclusive for the specimen tested at a mean stress of 60%, Figure 4.16 (b). At the lower stress level, the count rate activity was characterized by sporadic bursts but without a general increasing trend. There was the possibility of crack initiation but the results were not conclusive. In the metallographic examination which followed no definite cracks were found in this specimen, there was only evidence of some void formation at the ends of the inclusions but no clearly defined cracks.

4.3.4 Steel D, Ramp Tests, Peened and Unpeened Samples.

The acoustic emission profiles for an unpeened sample are shown is Figure 4.17 and for a peened sample in Figure 4.18. For either surface condition the low stress level tests were characterized by low signal amplitudes. At the intermediate stress level ($60 \leq \sigma \leq 80$) there was a distinct pattern developed by the acoustic emissions. At the beginning of the test there was a brief period of high acoustic emission activity followed by a quite steady period and then a final active period towards the end of the test. The characteristic signal pattern is shown in Figure 4.17 (a) for the unpeened specimen and Figure 4.18 (a) for the peened sample.

At the higher stress levels the point of crack initiation corresponded to a rapid increase in the acoustic emission activity, as shown in Figure 4.17 (b) and Figure 4.18 (b) for the unpeened and peened samples respectively. For either sample crack initiation was characterized by a sudden increase in acoustic emission activity.

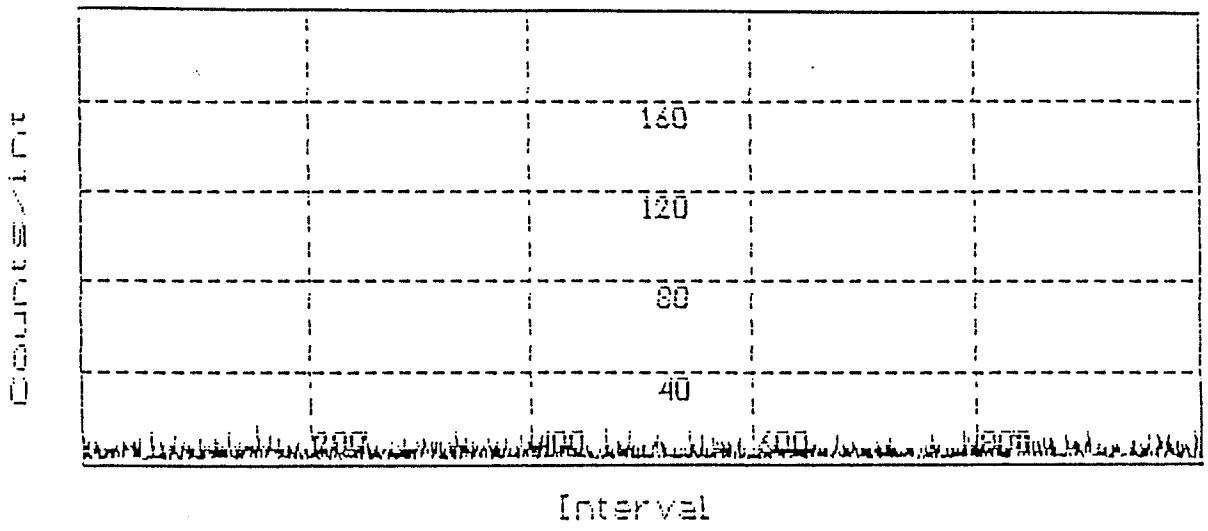

(a)

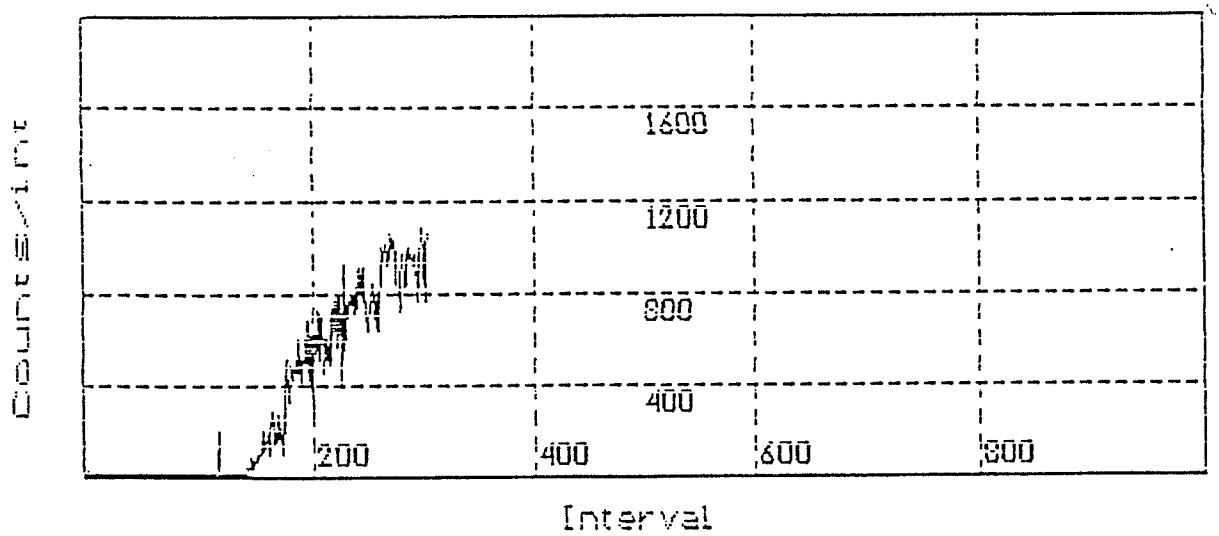

(b)

Figure 4.15: Acoustic emission activity during constant mean stress testing, steel C unpeened, (a) steady background noise and (b) crack initiation.

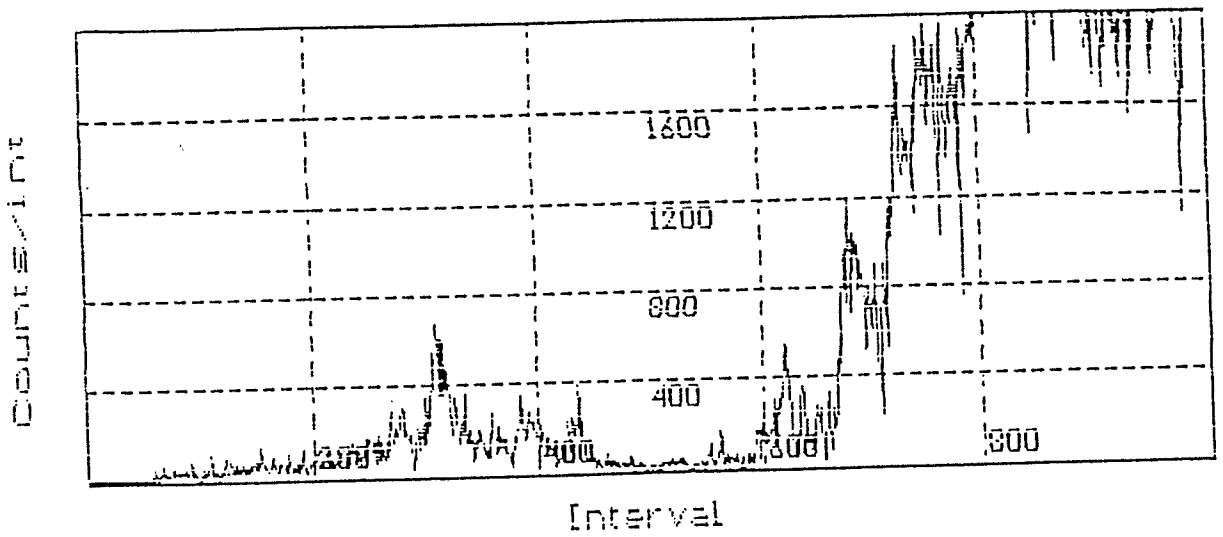

(a)

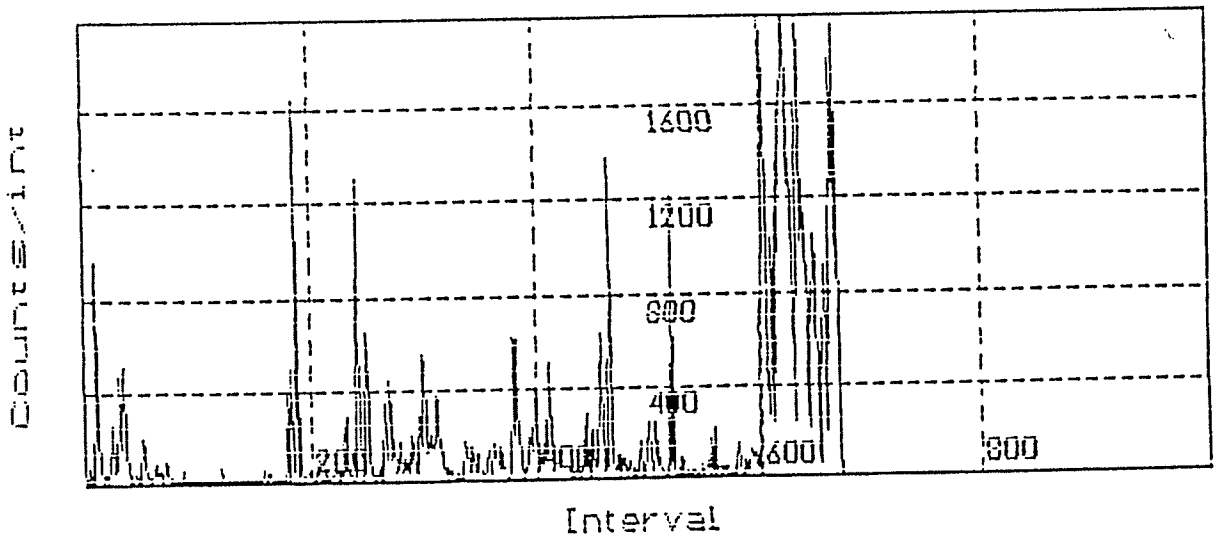

(b)

Figure 4.16: Acoustic emission activity during constant mean stress level testing, steel C peened samples, (a) 80% and (b) 60%.

4.3.5 Steel D, S-N Tests, Peened and Unpeened samples.

Two examples of the acoustic emission activity during constant mean stress level tests are shown in Figure 4.19 and Figure 4.20. Figure 4.19 is for an unpeened sample tested at the 40% stress level and Figure 4.20 is for a peened sample tested at the 80% stress level.

For the unpeened sample the presence of an active fatigue corresponds to the rapid increase in acoustic emission activity after 400 intervals, see Figure 4.19. The increase in activity before the 400 interval may signify crack initiation and beyond this interval propagation of a well defined Stage II crack.

The behaviour of acoustic emission at the intermediate stress level for a peened sample are shown in Figure 4.20. The acoustic emission characteristics are similar to the results from step tests at intermediate stress levels, see Figure 4.17 (a) and Figure 4.18(a). In the initial stages of the test there was a period of high activity followed by a long period of low signals. The point of crack initiation is revealed by a sudden increase in acoustic emission. The drop after a period of high activity may be caused by crack blunting. The crack may blunted when the crack tip must propagate through or around a region of high compressive stresses. Beyond this point acoustic emission increase dramatically until the test is stopped.

4.4 Crack Initiation Sites

Following mechanical testing the specimens were examined to find the crack initiation sites. A detailed metallographic examination was necessary to confirm the acoustic emission results and to determine the causes of crack initiation.

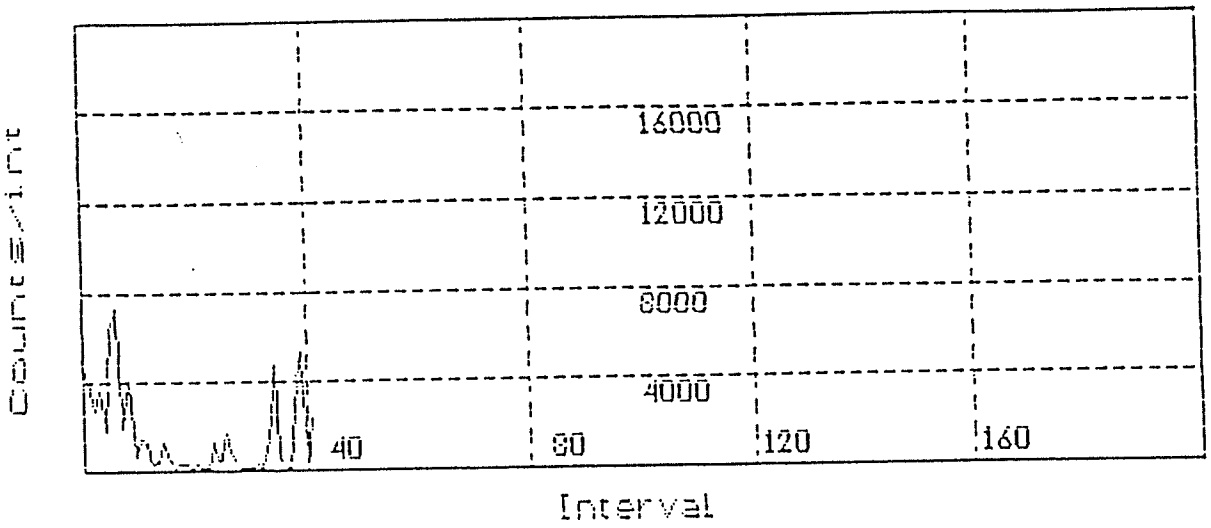

(a)

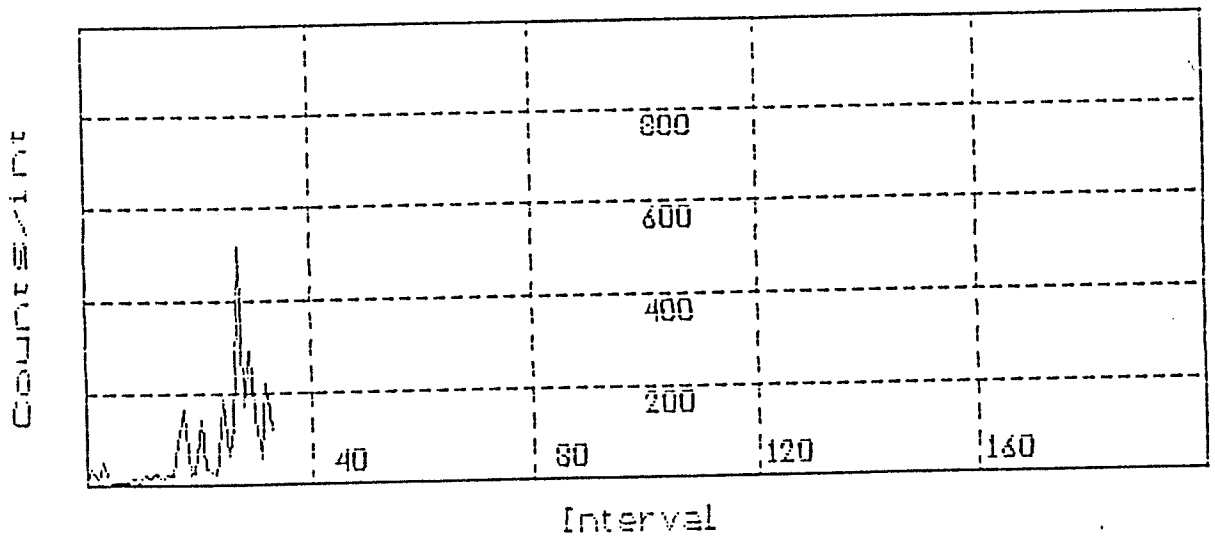

(b)

Figure 4.17: Acoustic emission activity for an unpeened steel D sample during step mean stress testing, (a) 60% and (b) 100%.

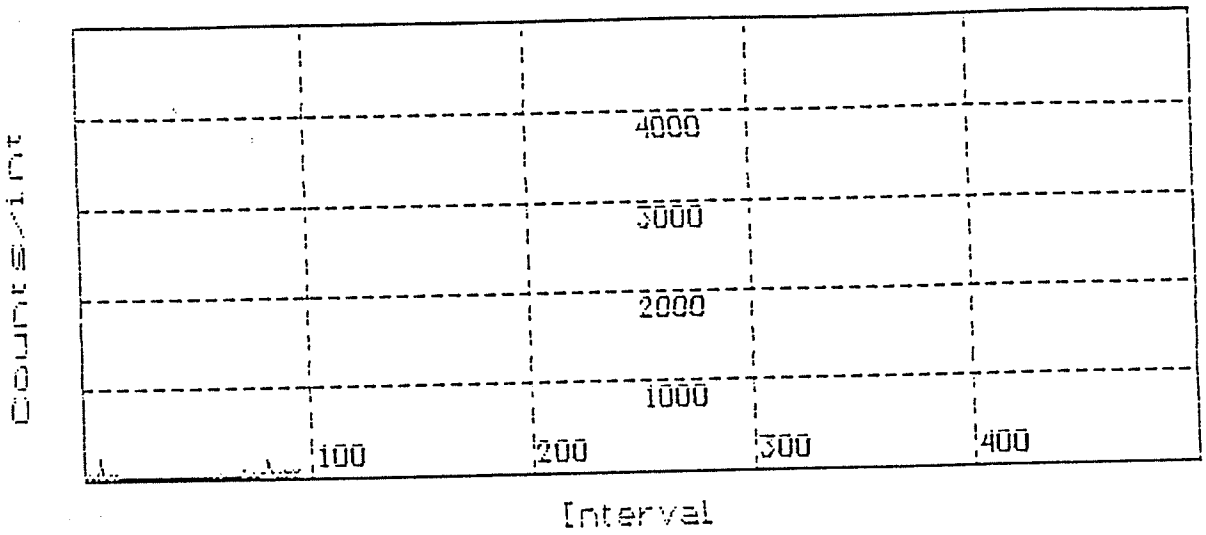

(a)

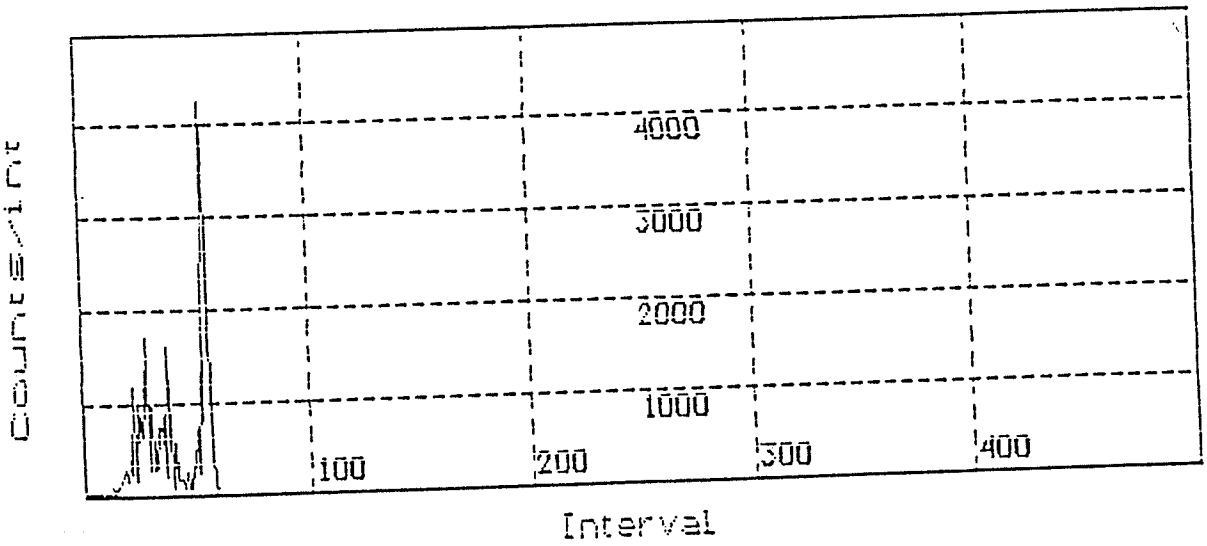

(b)

Figure 4.18: Acoustic emission activity for a peened steel D sample during step mean stress level testing, (a) 60% and (b) 120%.

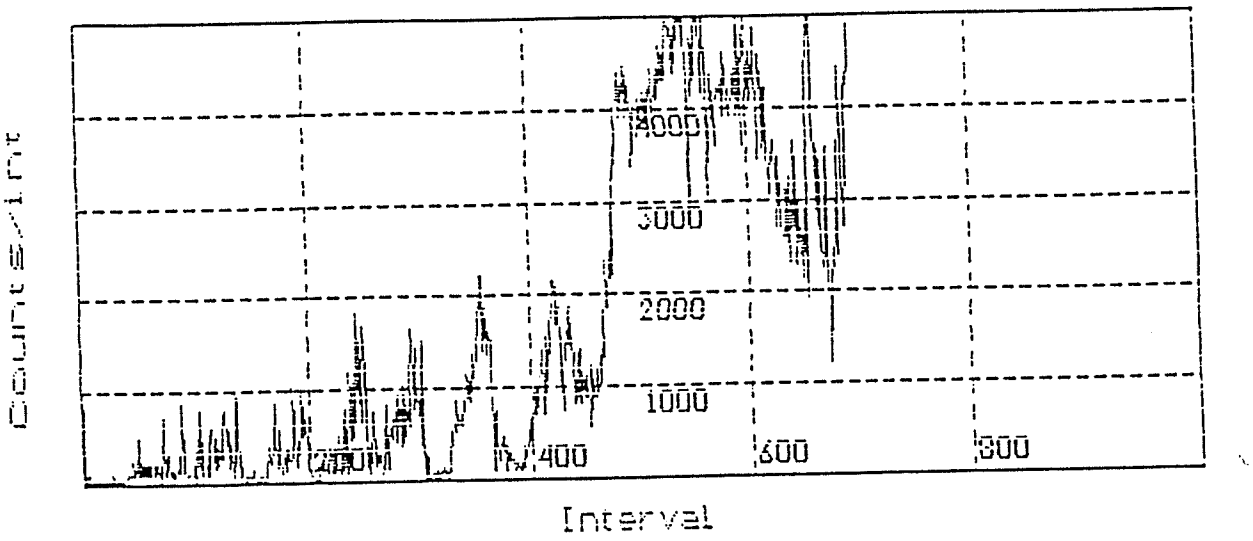

Figure 4.19: Acoustic emission activity for steel D unpeened sample during constant mean stress level testing, 40%.

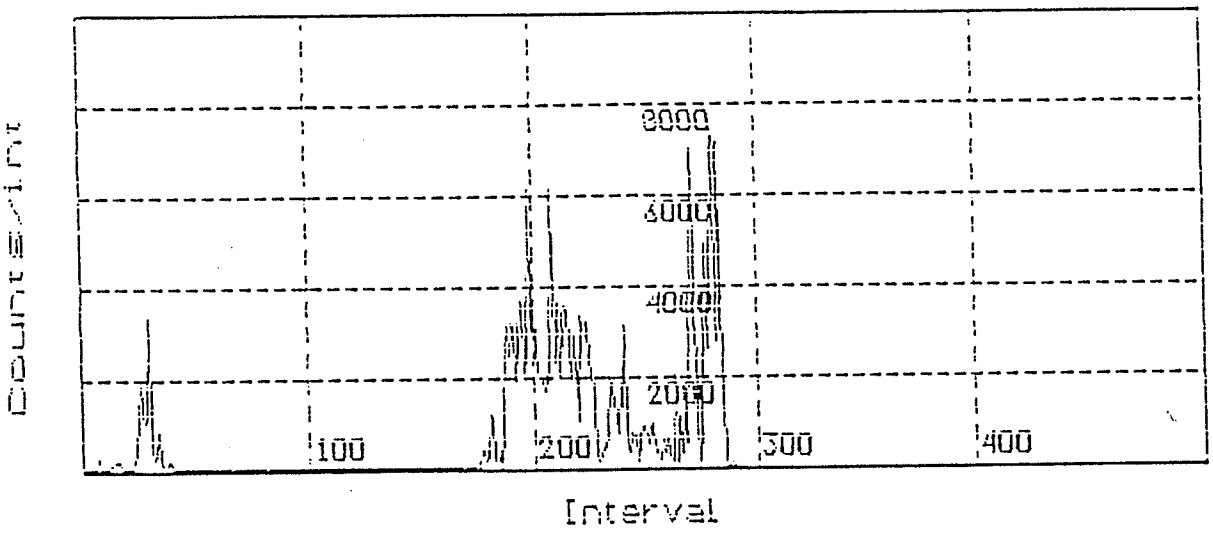

Figure 4.20: Acoustic emission activity during constant mean stress level testing for a peened steel D sample, 80%.

4.4.1 Preliminary Metallographic Investigations

Initial observations were usually performed using the optical microscope. Typical crack initiation sites for the four steels are shown in Figures 4.21 through to Figure 4.25. In all the fatigue samples the cracks propagate in a direction perpendicular to the principle tensile stress.

Crack initiation sites in steel C are shown in Figure 4.21 to Figure 4.23. Figure 4.21 shows a crack extending between clustered MnS inclusions. Their combined total length is approximately 35 μm. This crack was found in an unpeened sample following step testing. Another crack extending from a small cluster of MnS inclusions is shown in Figure 4.22. The specimen was peened and tested using the step loading program. The dark region of the inclusion at the crack initiation site is aluminum/silicate.

The majority of cracks in steel C were found to initiate at elongated duplex inclusions of MnS and Al_2O_3/SiO_2. Cracks were also found at extremely large aluminum silicate inclusions, as shown in Figure 4.23. However, the presence of such an inclusion was extremely rare.

The crack initiation sites in steel D were usually at thin elongated MnS inclusions with brittle silicate second phases. An example is shown in Figure 4.24. The crack extends from both end of the large inclusion. The smears and dark regions surrounding the inclusion are evidence of the brittle silicate phase. To confirm the nature of the inclusion the specimen was examined in the SEM.

Examples of cracks found in steels A and B are shown in Figure 4.25 (a) and (b). The inclusions are MnS and both samples were tested using the step mean loading program. In the steel B sample a small crack extends between the two inclusions can be seen in Figure 4.25 (a).

A higher magnification investigation using the SEM reveals the effect of the brittle silicate inclusion in initiating cracks. In Figure 4.26 (a) two cracks originating within a brittle silicate inclusion are shown. Both cracks are perpendicular to the principal

tensile stresses. Figure 4.26 (b) shows an extended crack passing through the MnS inclusion. Both photographs are taken from samples tested using the step mean load program.

To determine the types of inclusions which initiate cracks and to reveal the details of the crack initiation mechanism further examination of etched specimens was carried out using the SEM. The EDX analyzer attached to the electron microscope was used to identify the inclusions and to distinguish cracks from extremely thin inclusions.

4.4.2 Detailed Metallographic Observations

Following the initial examination to determine if a specimen was cracked selected typical cases were etched and reexamined. By etching the samples the microstructural influences on the crack initiation mechanisms were revealed. All of the samples selected were tested at constant stress amplitude with a mean stress of 80%. The results of this investigation are shown in Figure 4.27 through to Figure 4.30.

A crack beginning at an elongated inclusion in steel C is shown in Figure 4.27(a). The dark boundary surrounding the inclusion and extending into the matrix is Al_2O_3/SiO_2. The details of the crack are clearly visible in Figure 4.27(b). Immediately in front of the inclusion is a zone of highly deformed pearlite but the actual crack is approximately 30μm from the inclusion. Between the deformed pearlite and the crack is a zone of small voids and bent cementite plates. The voids are not joined and the crack is therefore discontinuous.

Details of the crack initiation site in steel A are shown in Figure 4.28 (a) and (b). The inclusion is MnS with no second nonmetallic phase present. In Figure 4.28(b) voids can be seen between the inclusion and the matrix. The voids surround the entire end of the inclusion and form a continuous boundary separating the inclusion and the matrix. The crack is clearly defined and continuous from the inclusion.

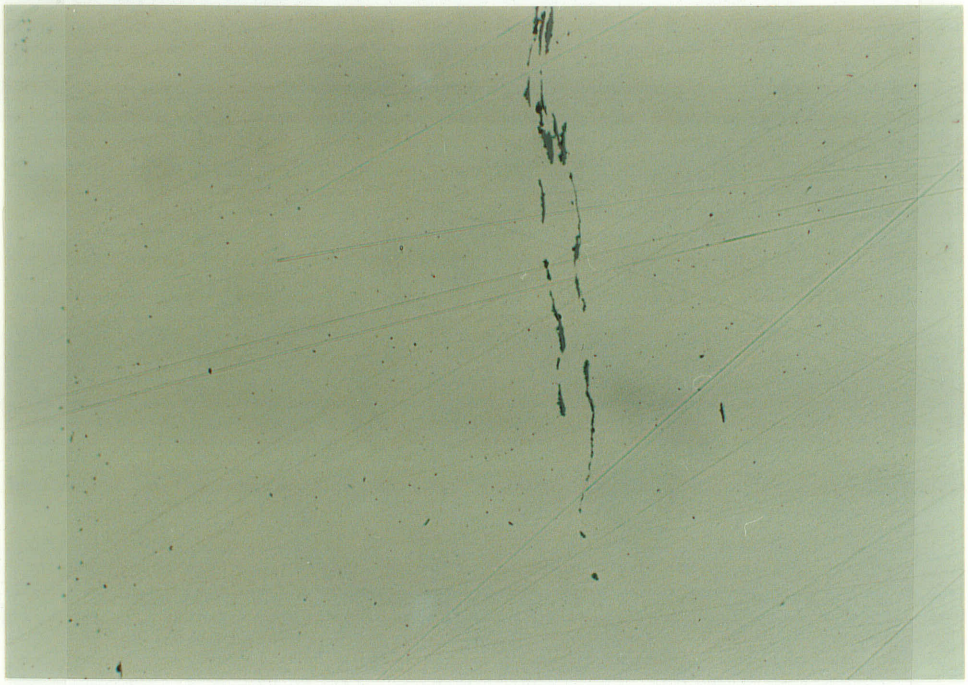

(a)

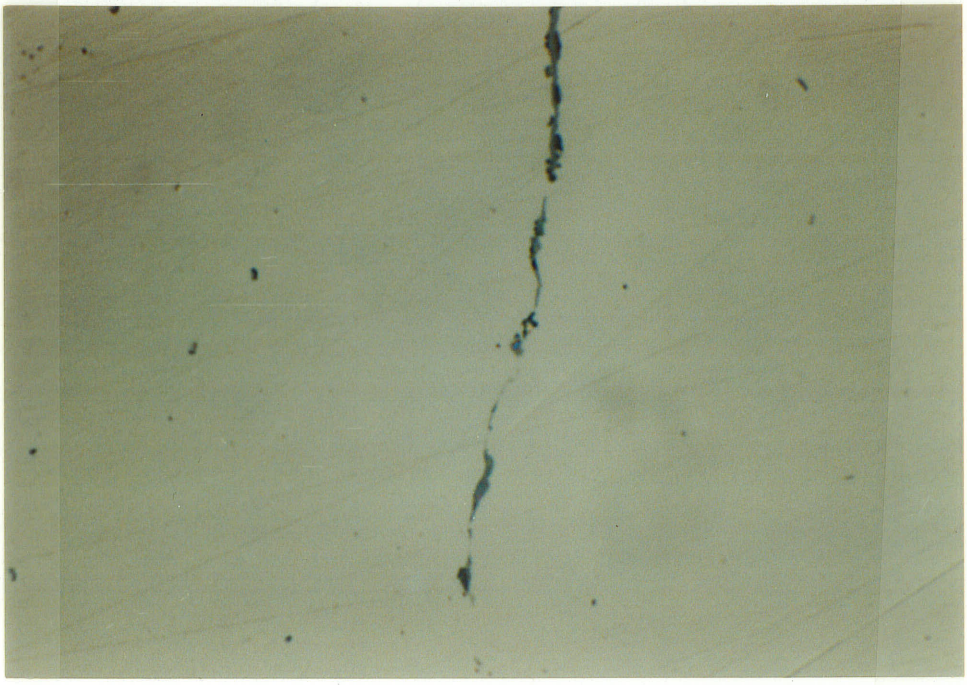

(b)

Figure 4.21: Cracks occurring in an unpeened steel C sample following ramp mean stress level testing, (a) 200X and (b) 1500X.

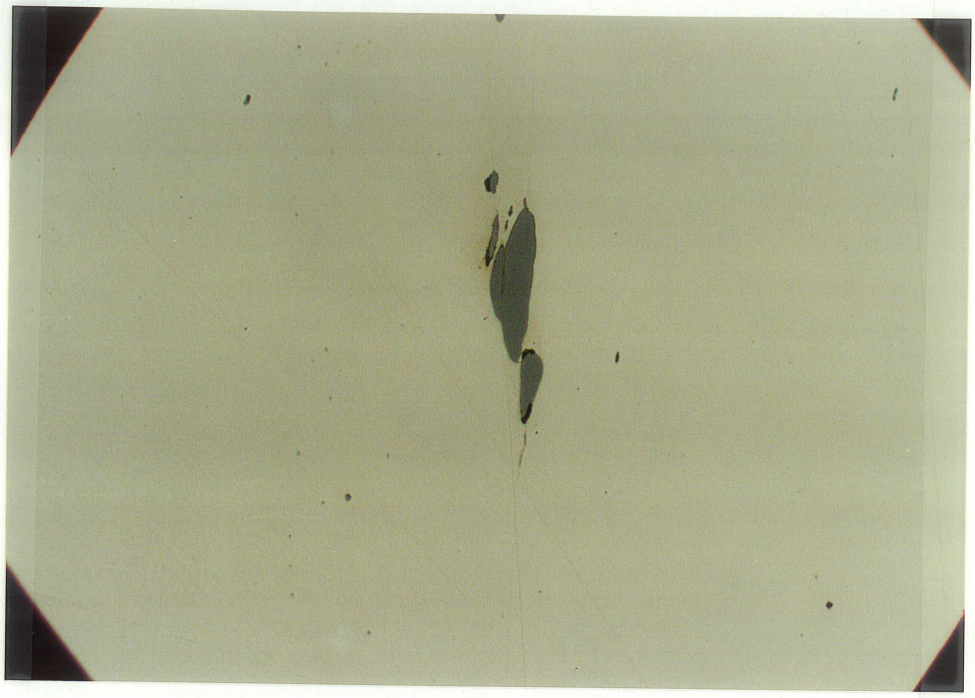

(a)

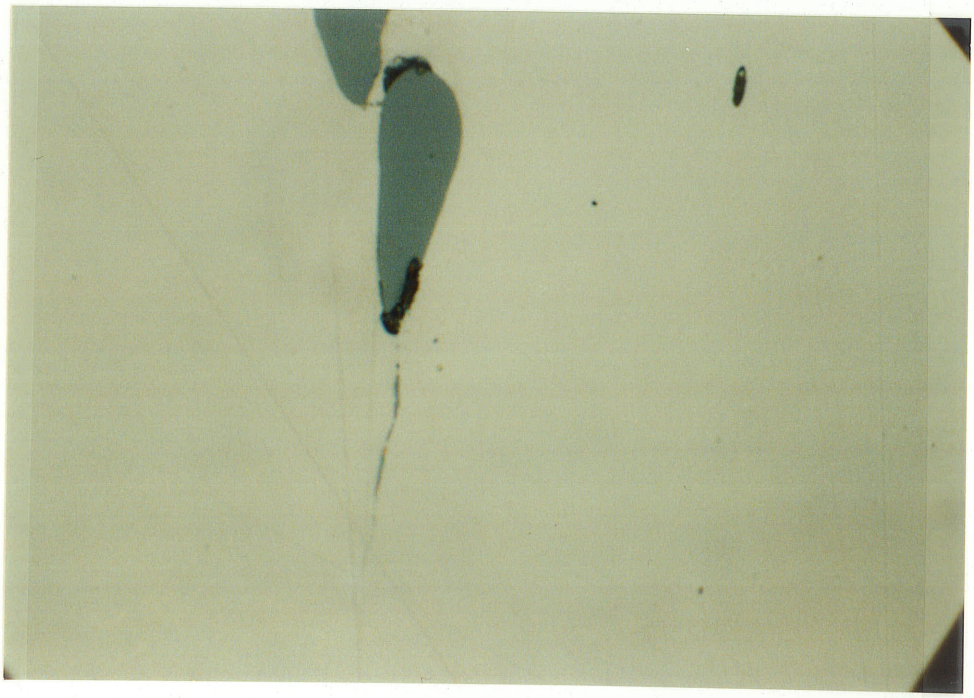

(b)

Figure 4.22: A crack extending from a MnS inclusion in a peened steel C sample. Ramp mean stress level testing, (a) 400X and (b) 1500X

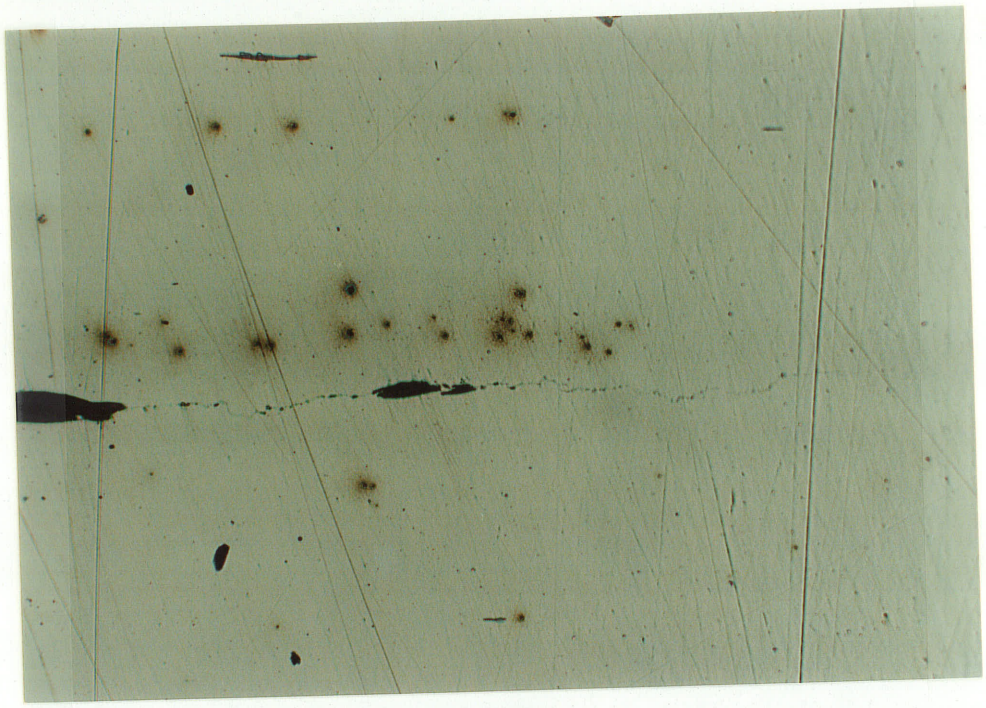

(a)

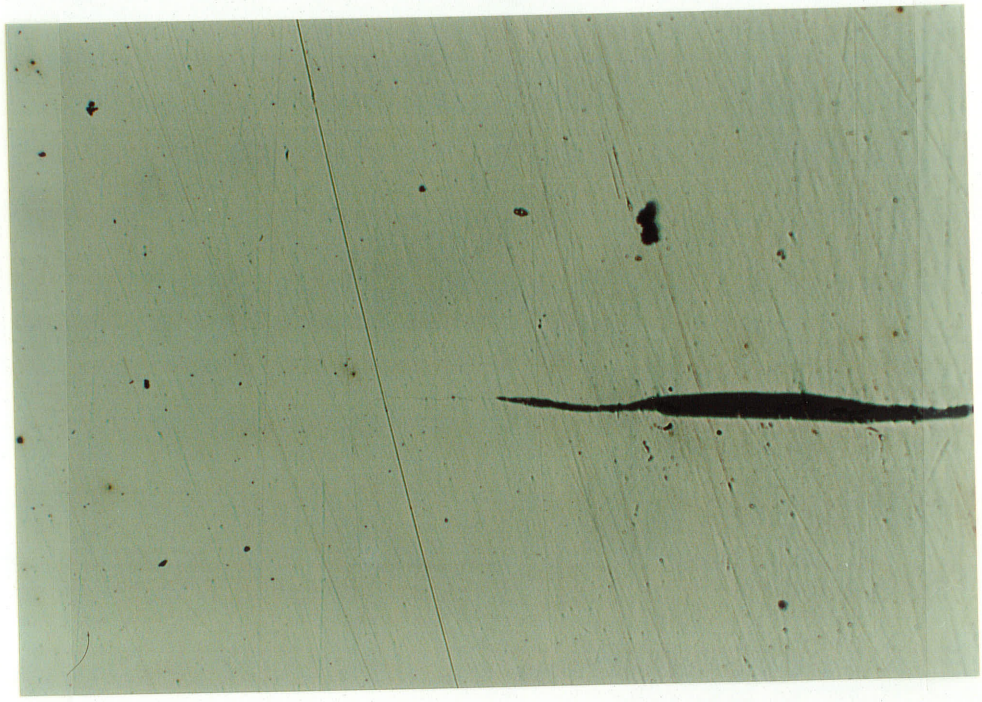

(b)

Figure 4.23: Crack at a elongated Al_2O_3/SiO_2 inclusion in steel C. (200X)

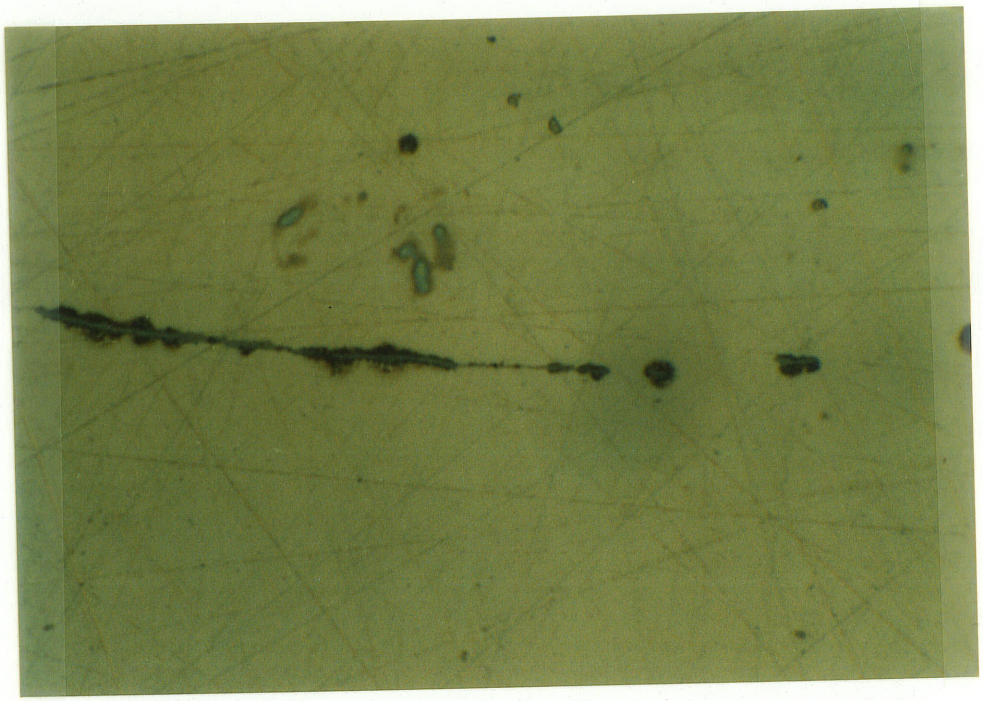

Figure 4.24: Crack extending from a thin elongated MnS inclusion in a sample of steel D, S-N testing, (1500X)

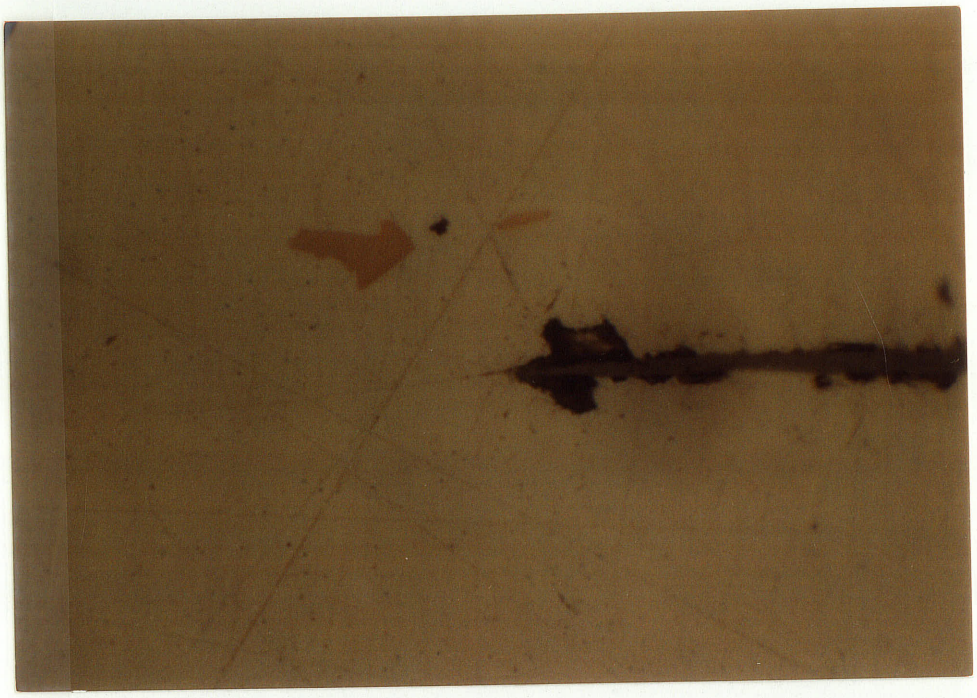

(a)

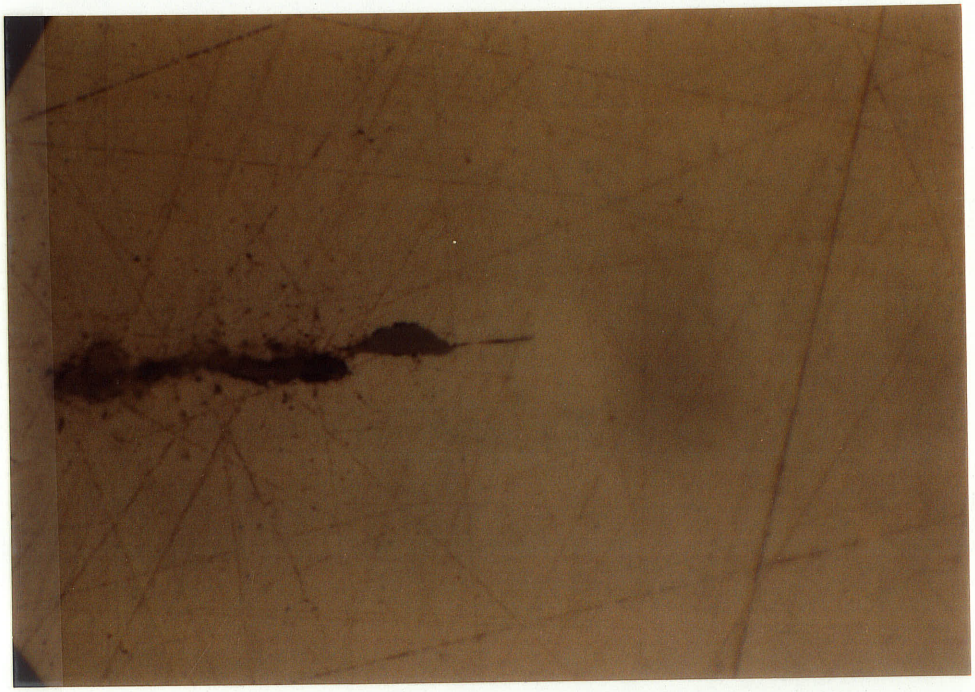

(b)

Figure 4.25: Crack at elongated MnS inclusions, (a) steel A, and (b) steel B.(1500X).

(a)

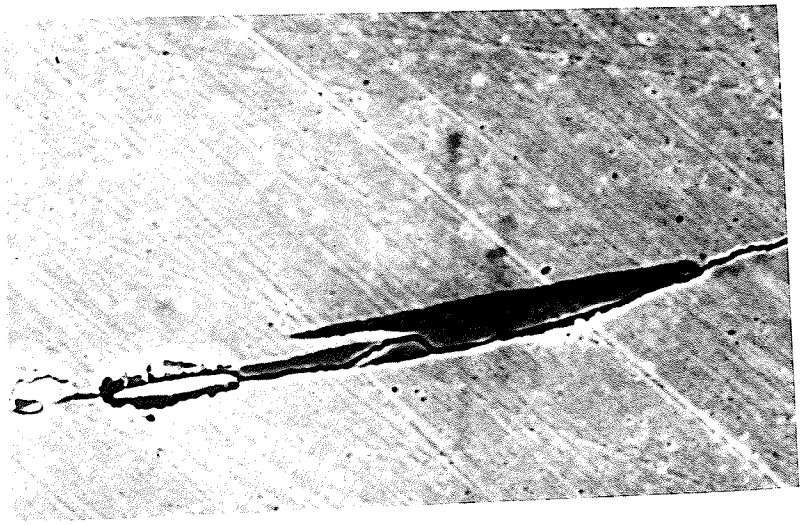

(b)

Figure 4.26: SEM photographs of (a) Crack initiation within a brittle silicate inclusion (3300X) and (b) a crack extending through a MnS inclusion (2500).

A similar separation between the inclusion and the matrix can be found in the sample of steel B, shown in Figure 4.29 (a) and (b). The voids and the crack are clearly continuous and extend along the entire length of the inclusions and into the matrix. Separated fragments and intrusions of cementite into the voids surrounding the inclusion can be seen in Figure 4.29 (b).

A thin long MnS inclusion was found at the crack initiation site in steel D, shown in Figure 4.30. The inclusion also has a brittle silicate second phase at the centre and towards one end, as shown in Figure 4.30 (a) and (b). The crack is clearly defined and can be seen passing along the entire length of the inclusion. The extension of the crack into the matrix can be seen in Figure 4.30(b).

In the steels A, B and C the pearlite lamellae is perpendicular to the crack direction at the initiation sites. This is shown in Figures 4.27(b), Figure 4.28(b) and Figure 4.29(b) for each steel respectively. A strict perpendicular orientation between the pearlite lamellae and the crack is not evident at the crack initiation site in steel D, which can be seen in Figure 4.30(b).

4.4.3 Quantifying the Crack Initiation Sites.

From the observations of tested and cracked specimens, certain characteristic features of the crack initiation sites for each individual steel and for all the steels were apparent. For all of the steels cracks were found to initiate at elongated inclusions and not at circular oxide inclusions. In the steel C the cracks initiate primarily at duplex inclusions of MnS and Al_2O_3/SiO_2. Extremely large aluminum silicate inclusion were also found to initiate cracks. However, the presence of large elongated aluminum/silicate inclusion was extremely rare. In steels A and B the cracks initiate at elongated MnS inclusions which have little or no second phase. A duplex inclusion of MnS with brittle silicate glass initiated cracks in steel D. The cracks were observed to originate within the brittle inclusion and propagate through an accompanying MnS inclusion.

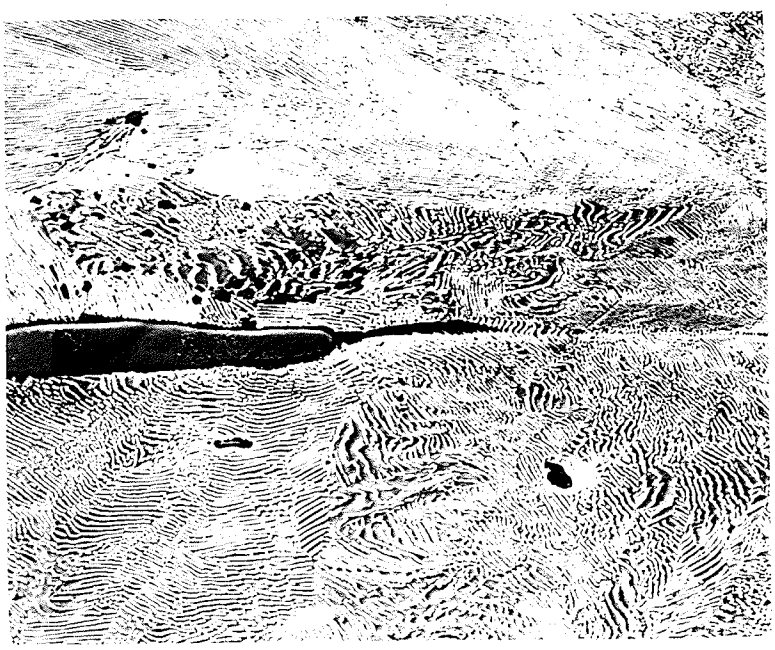

(a)

(b)

Figure 4.27 Etched fatigue crack initiation site in steel C: (a) a crack at the tip of a duplex inclusion (2500X) and (b) a microcrack formation away from the inclusion tip and a local deformation band ahead of the inclusion (5000X).

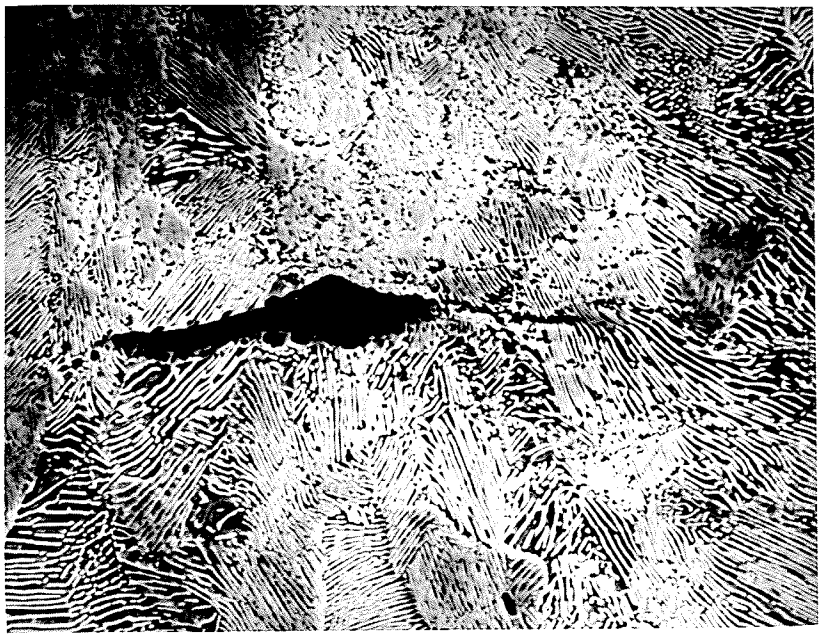

(a)

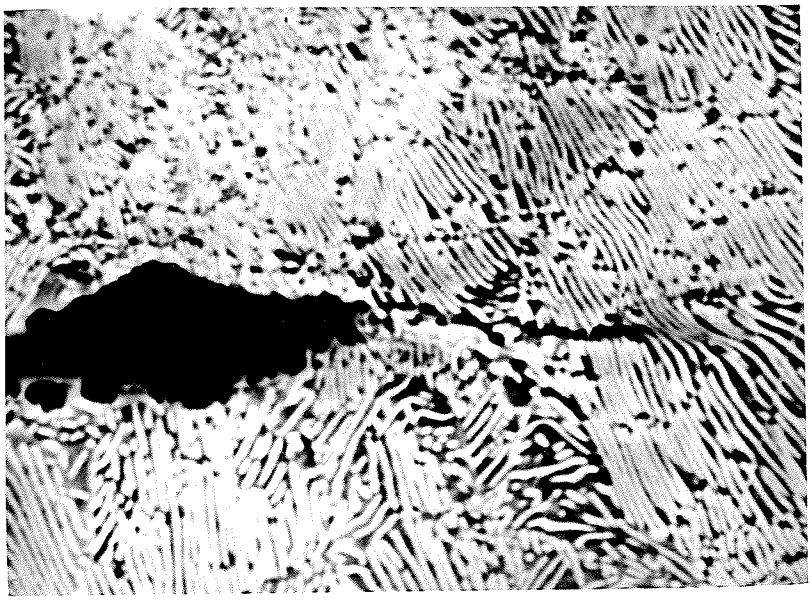

(b)

Figure 4.28: Fatigue crack initiation site in steel A: (a) crack initiation at the tip of an elongated MnS inclusion (2500X) and (b) void formation at the inclusion/matrix interface (5000X)

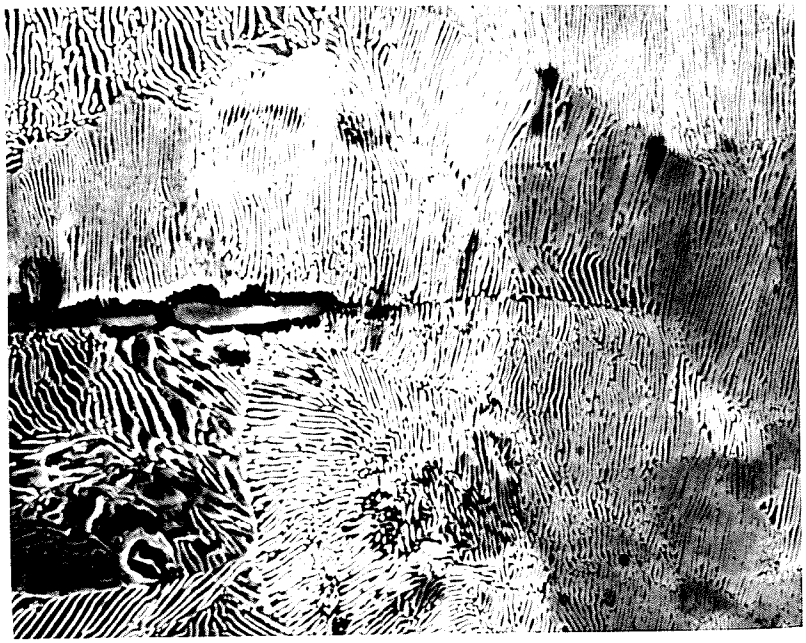

(a)

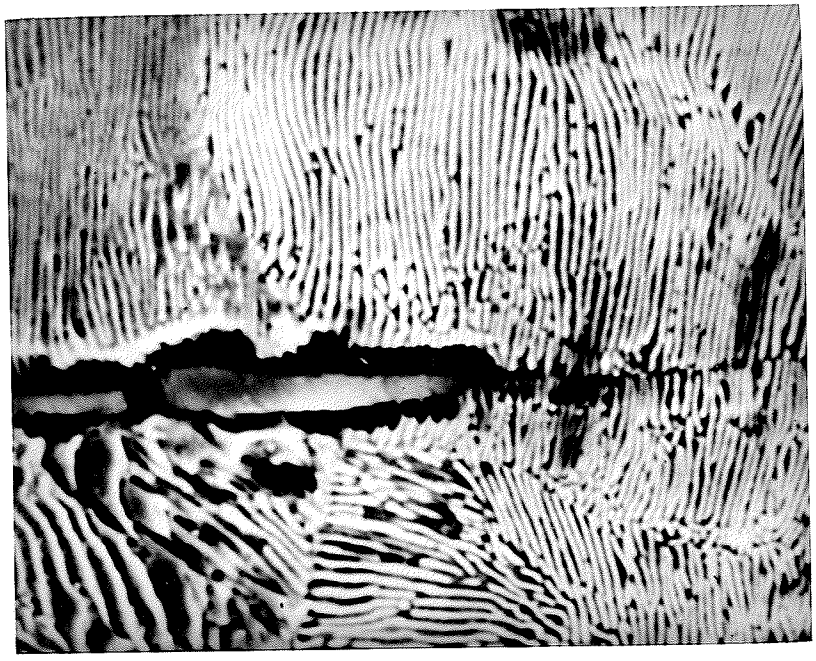

(b)

Figure 4.29: Fatigue crack initiation in steel B: (a) a crack at a MnS inclusion (2500X) and (b) debonding between the inclusion and the matrix (5000X).

(a)

(b)

Figure 4.30: Fatigue crack initiation site in steel D: (a) a crack from a broken silicate glass inclusion (500X) and (b) crack extending from the inclusion into the matrix (2500X).

4.5 Summary of the Experimental Results

4.5.1 Inclusion Types

Each steel contained elongated MnS inclusions, but this inclusion varied from steel to steel because of the possible presence of a second inclusion phase. In steel C, the MnS inclusions usually contained regions of Al_2O_3/SiO_2. This second phase can encapsulate the entire MnS inclusion. In steels A and B most of the elongated MnS inclusions were homogeneous without any second phase along the inclusion/matrix interface. In steel D the MnS inclusions were often associated with a brittle silicate inclusion.

Each rail steel also contained circular alumina oxides and alumina silicate inclusions. In addition to circular alumina inclusions in steel C there were elongated alumina and alumina silicate inclusions.

4.5.2 Inclusion Morphology

The steel with the highest inclusion content was steel C, followed by steel A, steel D and finally steel B. In addition to having the largest volume percentage of inclusions, the inclusions in steel C were also on average the largest. Following the elimination of the inclusions which were found to be ineffective crack initiators steel C was still had the largest inclusions but the remaining inclusions in steel D were the most elongated. For both statistical populations steel B had the smallest and most circular inclusions. The calculated spacing between inclusions was significantly smaller for steel C. Another indication that this steel contained the most inclusions and was therefore the 'dirtiest'.

4.5.3 Properties Evaluation

Steel D was the hardest steel and had the highest yield strength. Steel C was the softest and had the lowest strength. The steel with the best overall fatigue performance in the unpeened condition was steel C. This was true for both the ramp mean stress level testing

and the constant mean stress level testing. Steel C also had the best fatigue performance in the shot peened condition for the ramp testing. However, steel B had the best resistance to crack initiation during constant mean stress level testing for shot peened specimens. Surprisingly, the steel with the highest yield strength was found to have the poorest fatigue performance, steel D. The poor fatigue performance of this steel was reflected by both a low fatigue limit and a low number of cycles to crack initiation at higher stress levels.

4.5.4 Acoustic Emission Results

At low to moderately high stress levels the acoustic emission monitoring system was able to detect crack initiation reliably. Often cracks as small as 0.01 mm were detected. At the highest stress levels the surface vibrations would occasionally interfere with the acoustic emission and obscure crack initiation.

4.5.5 Crack Initiation Sites

In all of the steels the cracks initiated at elongated inclusions. In steels A and B these inclusions were strictly MnS. In steel C the cracks would usually initiate at duplex MnS and Al_2O_3/SiO_2 inclusions. The crack initiation sites in steel D were at duplex inclusions of MnS and brittle silicate glass.

Detailed metallographic studies of etched specimens revealed three different initiation sites. In steels A and B the cracks initiated because of the stress concentration resulting from the debond seam between the MnS inclusion and the matrix. In steel C the cracks initiated by void coalescence in the highly stressed zone ahead on the inclusion. The cracks were found to initiate away from the inclusion. The third crack initiation site was found in steel D. The cracks initiated within the brittle silicate-glass inclusions and would then grow through an accompanying MnS inclusions or into the matrix.

Chapter V

Discussion

5.1 The Crack Initiation Mechanisms

5.1.1 Introduction

In this section of the discussion the details of the different crack initiation mechanisms in the four rail steels are investigated, and the influence of the nonmetallic inclusions are examined.

5.1.2 A Review of the Crack Initiation Sites

The detailed metallographic observations of tested specimens revealed three distinct crack initiation mechanisms. The micrographs are shown in Figure 4.27 to Figure 4.30. The crack initiation mechanisms in steels A and B are the same while steel C and steel D each have a unique mechanism. A factor common to all four steels is that cracks initiate at elongated inclusions and not at circular oxides.

The crack initiation sites in steels A and B are shown in Figure 4.28 and Figure 4.29 respectively. Both cracks initiate at elongated MnS inclusions which are separated from the matrix by voids. Fragments of cementite can be seen in the voids surrounding the MnS inclusions in Figure 4.29 (b).

The initial stages of crack initiation is steel C are shown in Figure 4.27. The crack initiates ahead of elongated duplex inclusions. The inclusion has an inner core of MnS surrounded by a thin layer of Al_2O_3/SiO_2 which extends from one end of the inclusion into the matrix. Immediately in front of this extension is a zone of highly deformed pearlite followed by a zone of tiny voids in the ferrite, see Figure 4.27 (b). The crack is ahead of the separated voids, approximately 30 μm from the inclusion.

In steel D the cracks were found to initiate within brittle silicate inclusions which are normally associated with MnS inclusions, as shown in Figure 3.30. The crack in Figure 3.30 is clearly defined and extends along the entire length of the MnS inclusion. Cracks initiating within a brittle silicate-glass inclusion are shown in Figure 4.26 (a)

5.1.3 Mechanisms of Crack Initiation

The principal effects of inclusions are to increase stress magnitudes in their immediate vicinity and to alter the uniaxiality of the stress field [19]. The effectiveness of the inclusion in increasing the local stress magnitude and in altering the stress field depends on the shape and size of the inclusion, on the ratio of the elastic modulus of the inclusion and the matrix and on the strength of the inclusion/matrix bond.

Due to the number of variables involved, several different crack initiation mechanisms exist. The mechanisms are a function of all of the above influences and the loading condition. That is, the amount of plastic deformation taking place. The different mechanisms proposed include debonding of the inclusion from the matrix [28], the formation of slip bands which impinge on inclusions [65], and plastic zone development about the inclusions [24]. For the four rail steels tested three different initiation mechanisms were observed and will be discussed in the following section. An important and common factor to all three mechanisms is that the cracks initiate at a local surface discontinuity or hole. How this discontinuity is formed distinguishes the three different mechanisms.

5.1.4 Void Formation at the Inclusion/Matrix Interface

The crack initiation mechanism in steels A and B begins with the formation of voids at the inclusion/matrix interface. The voids form as a result of intrusions of ferrite at the boundary and the accompanying fracture of the cementite plates. Fragments of cementite in the voids are shown in Figure 4.29 (b). The separation of the inclusion from the matrix

suggests a low cohesive strength at the interface which allows the inclusion to become detached from the matrix.

If the bond between the inclusion and the matrix is weak then the interface may be considered as a free surface where cracks can initiate. The formation of cracks is further enhanced if the bond is degenerated and voids form. Chipperfield and Skinner [44] proposed that crack initiation in rail steels begins at inclusions that are separated from the matrix. Crack propagation from debonded stringer inclusions was also observed by Fowler and Tetelman [66].

Debonding of the inclusion is a mechanism of crack initiation proposed by Langford and Kusenberger [28] and for certain loading conditions verified by Eid and Thomason [23]. Common to both investigations is the presence of hard second phase particles which either debond or become fatigue damaged. The MnS inclusions observed at the crack initiation sites in steels A and B are not hard and brittle. Thus, the mechanism by which the inclusions become separated from the matrix differs. Instead of forming a debond seam as a result of being pulled from the matrix, voids form as a result of the intrusions of ferrite and fracture of the cementite plates. A debond seam which encompasses the entire inclusion may form as the voids grow and coalesce with further cyclic loading. Experimental observations revealed that it is not necessary for the inclusion to be entirely debonded to act as a crack initiation site, see Figure 4.28 (b). If the voids surround one end of the elongated inclusion an effective stress raiser is created and crack initiation can result.

A similar crack initiation mechanism was observed by Kung and Fine [65] during fatigue experiments of aluminum alloys. Cracks initiated where slip bands in the matrix impinged on constituent particles. This has also been observed by Barnby and Peace [26]. The slip bands form intrusions and extrusions at the particles interface. According to Kung and Fine, the need for both a singularity in the matrix as well as an inclusion may explain

why certain inclusions initiate cracks and why many larger particles do not. Slip bands are the most obvious singularity.

Once the inclusion and the matrix are separated the stress concentration ahead of the inclusion increases substantially. Edwards [21] has determined the stresses in the matrix surrounding an elliptical inclusion as a function of the inclusion's rigidity and shape. If the elastic modulus of the inclusion is zero, then the problem reduces to that of a cavity and local stresses reach a maximum. Regardless of the inclusions shape the stresses are always maximum at the pole of the elongated axis when the rigidity of the inclusion is zero. If the inclusion is infinitely long, ie., a straight line segment, then the stresses ahead of the inclusion are calculated to be approximately 2.75 times the uniaxial tension. As the inclusion's shape becomes more spherical this stress intensity reduces to a factor of approximately 2. If the inclusion can be treated as a cavity once it is separated from the matrix then the stresses in the neighboring matrix are maximum regardless of the inclusion's shape.

This explains why crack initiation occurs at the poles of the elongated axis once the inclusion is separated from the matrix. In these areas of high local stress concentration, plastic zones will form when the applied stress, σ, times the local stress concentration factor, K, exceeds the materials yield stress, σ_y. For these two steels this can occur when σ_{mean}= 60% if K≈ 2. At this stress level the applied maximum stress, σ_{max} = 470 MPa, times the stress concentration factor exceeds the steels yield strength, σ_y = 630 MPa.

5.1.5 Void Formation in Localized Deformation Bands.

Unique to steel C is a crack initiation mechanism resulting from void coalescence in a region of stress concentration ahead of an elongated inclusion. In this steel the cracks initiate at elongated duplex inclusions which have a MnS inner core surrounded by Al_2O_3/SiO_2. The Al_2O_3/SiO_2 compound may encapsulate the entire MnS inclusion or be restricted to just the ends of the elongated axis.

The crack initiation mechanism reveals some characteristics of these duplex inclusions. First, the absence of any voids suggests that there is a strong cohesion between the inclusion and the matrix. Second, the inclusions are ductile and accommodate the elastic deformation of the matrix without themselves becoming fatigue damaged. Third, the combined elastic modulus of the inclusion is generally smaller then the elastic modulus of the matrix. If the reverse is true then the matrix should be deformed or strained around the inclusion following cyclic loading. No evidence of any matrix deformation is found at the duplex inclusions following testing, except in the regions where crack initiation occurred.

The crack initiation mechanism operating in steel C is a result of the stress concentration and the triaxial stress field associated with the duplex inclusions. If the elastic modulus of these inclusions is smaller then the elastic modulus of the matrix then there is a stress concentration at the ends of the elongated axis of the inclusions. According to the calculations by Edwards [21] the stress concentration varies with the rigidities of the two materials. The stress concentration decreases as the ratio of the two elastic modului approaches 1.

Eid and Thomason [23] have estimated the elastic modulus of a MnS inclusion to be 138 GPa. The elastic modulus of rail steel has been determined by Scutti et al. [67] to be 190 GPa. Their steel is similar in composition and strength to steel C. The ratio of the inclusion/matrix is then, $E_{mn}/E_m \approx 0.73$. Therefore, at the ends of the elongated inclusion there is a stress concentration.

Evidence of the stress concentration at these duplex inclusions is provided by the crack initiation mechanism operating in steel C. The cracks initiate away from the inclusion/matrix interface, possibly at a site of maximum stress concentration. Langford and Kusenberger [28] observed that cracks initiate away from the inclusion/matrix interface at a location of maximum shear stress in 4340 steel.

Regardless of the relative rigidity of the inclusion and the matrix, inclusions also change the stresses in their immediate vicinity due to the incomplete transmission of stresses across

the metal/inclusion interface [9]. Therefore, even if the stress concentration at the inclusions due to differences in physical properties is minimized, a local stress triaxiality will result. The highly deformed pearlite and microvoids, shown in Figure 3.27 (b) indicate high deformation in the matrix ahead of the inclusion tip. The voids form in a region of high triaxial stresses which is a result of the Al_2O_3/SiO_2 extension.

The presence of voids in the ferrite and the adjacent kinked and fractured cementite suggests a crack initiation mechanism which is similar to that proposed by Miller and Smith [68] called shear cracking. In this modal cracking occurs at a cementite plate under the combined influence of an applied tensile stress and localized shear in the ferrite lamellae, as shown in Figure 5.1 (a). Deformation becomes concentrated in a shear band Figure 5.1(b) causing cracking of adjacent cementite plates which leads to void growth and coalescence Figure 5.1 (c,d). Tendency for void formation is greatest when the pearlite colony is aligned with the principal tensile stress axis. The initial shear bands result from the stress concentration caused by the inclusion.

5.1.6 Fatigue Damaged Brittle Inclusions

The crack initiation mechanism in steel D results from fatigue damaged inclusions. Brittle silicate glass inclusions in this steel form internal fatigue cracks, as shown in Figure 4.26 (a). Subsequent fatigue cycling results in crack propagation either into the matrix or through an accompanying MnS inclusion. Fatigue cracks initiate within these brittle inclusions because they are unable to accommodate the plastic deformation in the matrix.

Cracks initiating from fatigue damaged inclusions was also verified by Lankford [24] and by Eid and Thomason [23]. Although the details of the loading conditions differ for each study the effect of the damaged inclusions is the same. In each case the crack or hole formed within the inclusion provides a local stress concentration and any further cycling leads to a fatigue crack within the matrix. According to Eid and Thomason at damaged

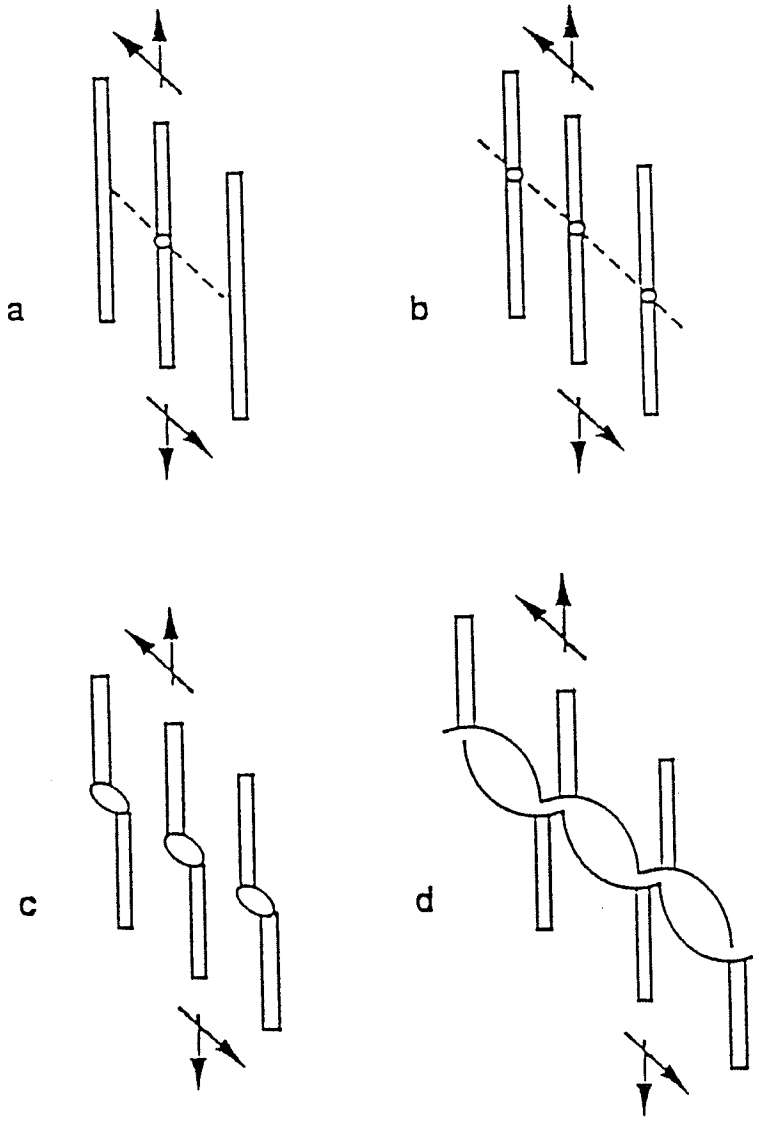

Figure 5.1 Fracture mechanism for pearlite: (a) cracking of a cementite plate, (b) shear zone development in ferrite causing cracking of adjacent plates, (c) and (d) void formation and coalescence [68].

inclusions cyclic-plastic zones develop which are essential to the nucleation of fatigue cracks.

Once a crack initiates within a brittle silicate-glass inclusion it can either propagate into the matrix or into a neighboring MnS inclusion. Whether the crack propagates into the matrix or through the MnS inclusion depends on the ΔK_{th} associated with each material. Assuming the initial short crack can propagate more easily through the softer MnS inclusion or along the inclusion/matrix interface then the crack tip will have a larger stress intensity factor before reaching the matrix. This is because the stress intensity at the crack tip is proportional to the crack length. Before the crack reaches the the matrix its length may be sufficiently long so that the crack growth will be continuous and smooth. At this stage the crack grows without experiencing periods of hesitation as observed by Stulen [69] for short cracks which initiated at inclusions in 4340 steels.

The length of the crack, once it has propagated through both inclusions can be estimated using the measurements given in Table 4.9. The average length of the inclusions following the elimination of all ineffective crack initiators is 48.41 μm with a standard deviation of 30.04 μm. The crack length can be estimated to be within a range from 25 μm to 127 μm. The minimum was the length of the smallest complex inclusion found at a crack initiation site. Lankford [24] concluded that any crack 50 μm in length was never observed to arrest. At this length the crack growth was smooth and continuous. Leis [8] adopted a length of 125 μm in his investigation of the crack initiation and growth behaviour of 1080 pearlitic steels. At this length the early growth transients, which are microstructure controlled, are avoided.

The threshold stress intensity ΔK_{th} has been conservatively estimated by Barsom and Imhoff [70] using the formula:

$$\Delta K_{th} = 6.98(1-0.85R) \qquad (5.1)$$

where ΔK_{th} is in MPa$\sqrt{m}$.

At the stress ratio of R = 0.3, ΔK_{th} can be estimated as 5.2 MPa$\sqrt{m}$, which is within the range for rail steels at different values of R as determined from experiments by Scutti et al. [67]. The stress intensity factor K_I ahead of a crack of length 2a is given by:

$$K_I = \sigma\sqrt{\pi a} \tag{5.2}$$

where σ is the applied stress.

If the stress intensity fluctuation associated with a crack of length 2a is 5.2MPa$\sqrt{m}$ then the corresponding applied stress can be calculated using equation 5.2. If the crack length, 2a, is equal to 0.025 mm then equation 5.2 suggests that the discontinuity is subjected to an equivalent nominal tensile stress fluctuation greater then the tensile strength of the steel.

If the crack growth is smooth and continuous then the crack will be in the stable stage II growth regime before entering the matrix. Although a barrier may exist at the inclusion/matrix interface the energy at the crack tip should be sufficient to overcome this obstacle. The crack can now propagate through the matrix.

As well, high strength steels are more notch sensitive [16], so defects reduce their fatigue strength to a greater extent. Therefore, the presence of an active fatigue crack within a MnS inclusion will be more detrimental to steel D than to the other three steels.

5.1.7 Summary of the Crack Initiation Mechanisms

The three distinct crack initiation mechanisms are illustrated in Figure 5.2. Each initiation mechanism has been summarized into four separate stages, beginning with a bonded inclusion, stage I.

In steels A and B crack initiation begins with the formation of voids at the inclusion/matrix interface, as illustrated in Figure 5.2(a) stage II. The voids coalesce and

form a debond seam along the inclusion/matrix interface, stage III. The resulting stress concentration initiates a fatigue crack in the matrix, stage IV.

Cracks initiate ahead of an elongated duplex inclusions in steel C. The crack initiates away from the inclusion, as shown in Figure 5.2(b) stage II. The crack forms as the microvoids within the ferrite coalesce, stage III. Eventually the voids form a continuous crack, stage IV.

In steel D the cracks initiate within a brittle silicate glass inclusion as shown in Figure 5.2(c) stage II. The cracks then extend along the interface between an accompanying MnS inclusion and the matrix, stage III. These long cracks propagate through the matrix, stage IV.

5.2 Characteristics of the Fatigue Performance of the Steels

5.2.1 Introduction

Three distinct crack initiation mechanisms were observed and they all be characterized as having introduced a surface discontinuity. How these surface discontinuities form distinguishes the different mechanisms but all eventually result in the initiation of a fatigue crack. The different initiation mechanisms influence the fatigue performance of the steels. The purpose of this section of the discussion is to examine the fatigue performance of the steels and to explain the results with reference to the three crack initiation mechanisms.

5.2.2 Ramp Mean Stress Level Testing

The close agreement between the three samples tested for each steel in both surface conditions is indicative of low cycle high stress fatigue tests. With increasing stress there is a general decreasing scatter in fatigue life [1]. Although the number of cycles to crack

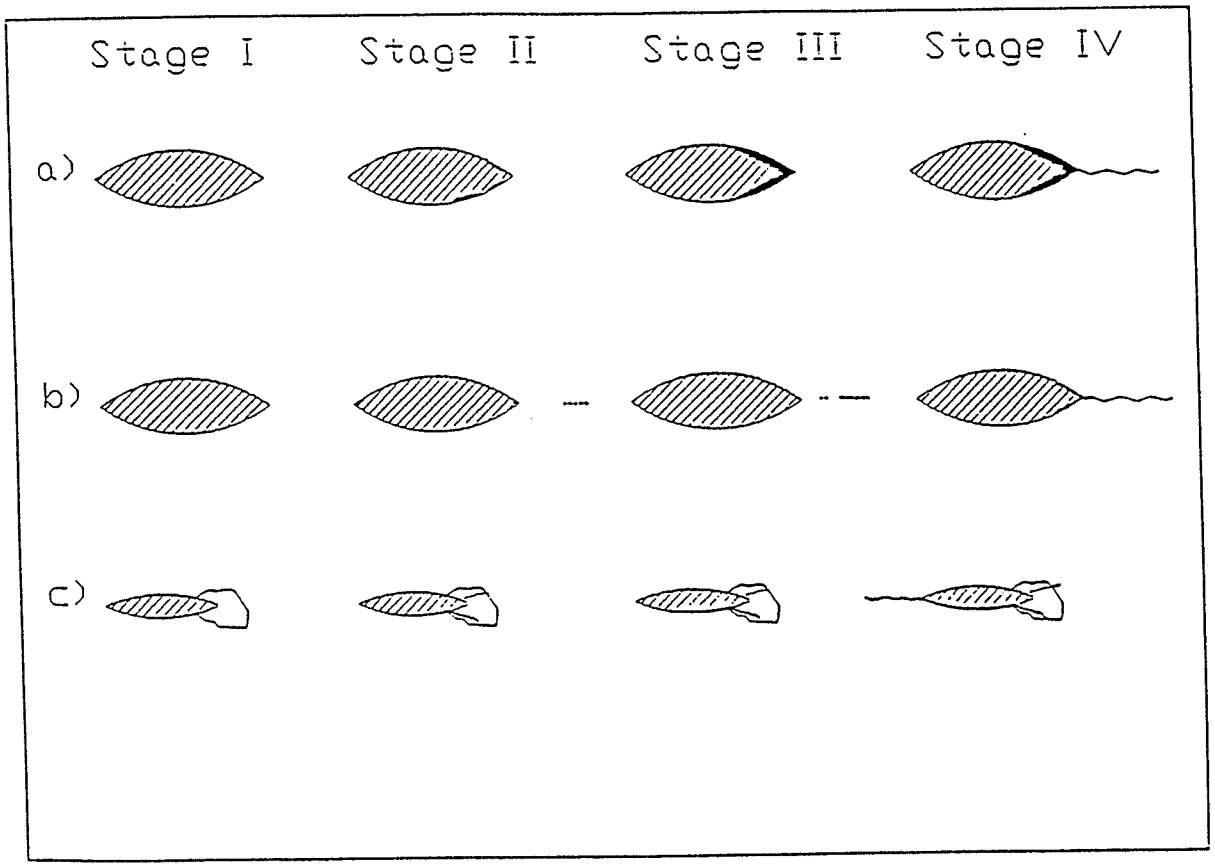

Figure 5.2 Three distinct crack initiation mechanisms: (a) debonded inclusions, steels A and B; (b) void coalesce in a zone of high stress concentration, steel C; (c) fatigue damaged brittle inclusions, steel D.

initiation for all the steels is within the range of the upper end of the intermediate-cycle range (10^5-10^6) the large stresses at the final loading stages are more indicative of low cycle fatigue.

The results given in section 4.2.2, reveal that steel C has the best overall fatigue performance for both surface conditions. Examination of the specimens following testing verified the crack initiation mechanism discussed in section 5.1.5. The crack initiation mechanism for steels A and B discussed in section 5.1.4 and the initiation mechanism discussed for steel D in section 5.1.6 were also verified.

The results of the ramp mean stress level fatigue testing indicate that steel C has the greatest fatigue resistance. The strong adhesion between the matrix and the duplex inclusion and the absence of a brittle easily damaged inclusion gives this steel the best overall fatigue performance, ie., the longest life to crack initiation.

There is little improvement in the fatigue performance of steel C following shot peening, see Table 4.14. The beneficial compressive stresses introduced by the shot peening may be neglected at high stress levels. Fading of the residual stresses occurs because of the plastic deformation occurring during high stress or low cycle fatigue testing [1].

Further evidence of fading of the residual compressive stresses in steel C during ramp mean stress testing is provided by the results from the higher strength rail, steel D. Following shot peening there is a substantial increase in the fatigue performance of steel D, see Table 4.14. The results of the tensile test given in section 4.2.4 show that this steel has the highest yield strength and should experience less plastic deformation, at any stress level. The beneficial compressive stresses introduced by the shot peening should therefore be evident at higher stress levels and result in a improvement in the fatigue performance of steel D during the ramp mean stress level testing. There was also a large increase in the number of cycles to crack initiation following shot peening for steels A and B. Both these steels have a yield strength high than steel C.

5.2.3 Constant Mean Stress Level Testing

To fully characterize the fatigue performance of each rail steel, specimens were subjected to an alternating load over a range of mean stress levels until crack initiation occurred. The resulting S-N curves were included in section 4.2.3. The steel with the best fatigue performance in the unpeened condition was steel C. There was close agreement between steels A, B and C following shot peening. Regardless of the surface condition, steel D displayed the poorest fatigue performance.

The difference in the number of cycles to crack initiation between the individual steels fluctuates with the mean stress level. This is a function of the ease with which a crack initiates and the applied stress. At low stress levels cracks form first in steel D, all the other steels approach the fatigue limit. The brittle silicate-glass inclusions are easily damaged and initiate cracks in steel D within a relatively low number of cycles at low stress levels, (ie. $\sigma_{mean} = 40\%$). The difference in the number of cycles to crack initiation between steel D and the other three steels decreases as the mean load increases.

Differences in the fatigue performance of each steel are also reflected by the slopes of the S-N curves. In particular the slope of the curve for steel D for either surface condition is steeper than the corresponding curves for the other steels, see Figure 4.9 and Figure 4.10. The steeper slope implies less variation in the number of cycles to crack initiation at increasing stress levels. This lack of variation is the result of the crack initiation mechanism operating in this steel. The brittle silicate-glass inclusions may be quickly damaged soon after cyclic loading begins. This creates a surface discontinuity with an accompanying stress concentration. The number of cycles to crack initiation is now a function of how quickly this surface discontinuity can initiate a fatigue crack within the matrix. However, the number of cycles to crack initiation is greatly reduced because a stress concentration has been created quickly in this steel.

For a particular steel a variation in the cycles to crack initiation at a particular stress level may be a function of the inclusion dispersion. Inclusions are known to introduce a degree

of scatter into the results of a fatigue study [71]. For steel D, large variations may result from the uneven dispersion of harmful inclusions. The variation in content and the dimensions of the inclusions are given in Table 4.3 and Table 4.5 receptively. Smaller fluctuations may result from differences in the size of the harmful duplex inclusions from specimen to specimen.

A variation in the number of cycles to crack initiation at a given stress level is also apparent for steel C. However, the variation for steel C is less than for steel D. The variation in the dispersion and dimensions of the inclusions may also be the principal cause of this scatter. At high stress levels the scatter decreases. This behaviour is in agreement with the results from the ramp mean stress level testing.

Improvements in the fatigue performance of all the steels following shot peening are reflected by increases in the fatigue limit of each steel and the fatigue life at higher stress levels. The most significant improvements in the fatigue performance are made at low stress levels near the endurance limit. Fading of the beneficial residual stresses at higher stress levels is most apparent for steel C, see Figure 4.12 (a).

5.2.4 Influence of the Inter-Lamellar Spacing

The results of the fatigue tests contradict the normally observed relationship between the fatigue performance of pearlitic steels and tensile strength. Usually, the fatigue limit is proportional to the tensile strength of the steel [38,72]. Increasing the yield strength by decreasing interlamellar spacing influences both the endurance limit and the number of cycles to failure at higher stresses. The manner by which decreasing interlamellar spacing increases the endurance limit is believed to be linked to the role of dislocations in crack initiation [5].

During cyclic plastic deformation dislocations can either emerge at a free surface or pile up against an obstacle depending on the nature of the mircostructure. The mechanism which causes dislocation pile ups of sufficient magnitude to cause a dislocation avalanche

essentially depends on slip length. Smaller mean free paths, resulting from interlamellar spacing refinement, reduce the magnitude of the local plastic strain and therefore reduce the ease of crack initiation and Stage I growth. As the pile up stress is reduced the stress which could cause a cementite plate to fail is reduced. Several theories of crack initiation in pearlite require a sufficient stress build up at the ferrite carbide interface to fracture the carbide lamellae [6].

5.2.5 Influence of the Inclusion Alignment

The results of this investigation suggest that the overriding influence on each steel's fatigue performance is not due to its microstructure but due to the influence of the non-metallic inclusions. As discussed by Rosenfield et al. [6] inclusion content has an overriding effect which tends to obscure the effect of other metallurgical variables. Epremean and Mehl [73] investigated the fatigue properties of SAE 4340 steel and Amco iron. Their results indicate that the scatter in fatigue endurance and in the fatigue limit were much more dependent on the inclusion content than on the composition and heat treatment. The significance of the inclusions in initiating fatigue cracks is further enhanced by the perpendicular alignment of the inclusions and the principal tensile stress axis. With this orientation the inclusions shape is more notch like and has a stronger influence on the fatigue properties.

The importance of the inclusions relative to the principal tensile stress was concluded from an investigation into the fatigue performance of two commercial heats of 4340 steel [18]. Fatigue failures were initiated by inclusions whenever the long axis of the inclusion was parallel to a direction of maximum shear stress or normal to a direction of principle tensile stress. Therefore, the stress concentration associated with an elongated inclusion is high for stresses perpendicular to its length but practically nil for stresses parallel to its length.

The same conclusion regarding the influence of elongated inclusions on the fatigue performance of steels was reached by Fowler and Tetelman [42]. For this investigation specimens for reverse bending loading were machined from the head of a fully pearlitic rail steel. The specimens axis were either aligned with the elongated inclusions or perpendicular to the inclusions long axis. The endurance limit was greatly reduced when the elongated inclusions were aligned perpendicular to the specimen axis. The same relationship between specimen orientation and fatigue resistance was observed by Leis [74].

The effect of elongated inclusions in initiating fatigue failures in rail steels has also been observed. An investigation by Heller et al. [72] located the origin of an incipient crack within a rail head at a oxide inclusion stringer. The inclusions act as internal notches and increase the stresses in their immediate vicinity. Chipperfield and Skinner [44] also observed crack initiation at stringer inclusions. The inclusion types were preliminary silicates and aluminates and are usually clustered together. Fegredo et al. [41] observed a strong association between elongated MnS inclusions and near-surface cracks. These subsurface cracks were located at the gauge corner of the rail head.

In all four rail steels tested in this investigation cracks initiate at elongated inclusions and not at circular oxide inclusions. The ineffectiveness of the circular oxide inclusions is a result of their small stress concentration compared to the elongated inclusions. The stress concentration depends on the inclusions dimensions, properties and orientation relative to the principal stress axis. For all three crack initiation mechanisms the stress concentration associated with the elongated inclusions is greater then the stress concentration at the small circular inclusions. Ransom [18] concluded that inclusions which are small spherical and evenly dispersed should not have as deleterious effects on the transverse fatigue properties as do the larger and elongated types.

5.2.6 Influence of the Matrix

For steels A, B and C the crack initiation site depends on the nature of the inclusion and on the influence of the matrix. For all three steels the pearlite lamellae must be aligned parallel to the principal tensile stress. Void formation in the matrix by cracking of the cementite plates occurs most easily when the colonies are aligned with the principal stress axis because the tensile stresses acting on the Fe_3C plates will be maximum.

Further influence of the microstructure in the crack initiation mechanism proposed for steels A and B results from slip band formation within the matrix. The resulting void growth mechanism involves intrusions of ferrite which impinge on the inclusion.

The ease with which a crack initiates by either mechanism is a function of both the nature of the inclusion and the matrix. The inclusion provides a local stress concentration where crack initiation can occur. But the initiation site also depends on the influence of the matrix. That is, the ease with which the matrix is cyclically deformed and therefore results in crack initiation.

The influence of the matrix in initiating fatigue cracks in steel D is minimal. Usually, a reduction in the pearlite inter-lamellar spacing improves the steel resistance to crack initiation. However, because of the easily damaged inclusions in this steel the beneficial influence of the matrix in preventing crack initiation is never realized. Once a crack is initiated, the effects of inter-lamellar refinement are no longer beneficial. Coarse inter-lamellar spacing results in more fatigue retardation and a slower propagation rate [7]. Head hardened rail steels should have better fatigue crack initiation characteristics then plain carbon rail steels because of a reduction in the amount of plastic deformation.

5.2.7 Inclusion Morphology versus Fatigue Performance

Due to the three different crack initiation mechanisms involved it is not possible to correlate the inclusion morphology measurements to each steel's fatigue resistance. Except for steels A and B, this aspect is examined later in the discussion. Even though steel C has

the greatest volume of inclusions, (see Table 4.3) and has the largest inclusions (see Table 4.4) it has the best fatigue performance. This is a result of the unique crack initiation mechanism operating in this steel. Therefore, it can be concluded that the greatest influence on the fatigue characteristics of these steels is due to differences in the types of inclusions present.

The type of inclusions present in each steel affects both the crack initiation mechanism in each individual steel and the characteristics of the initiation sites which are common to all four steels. In all four steels cracks initiate at elongated inclusions and not at spherical oxides. Differences in the elongated inclusions result in three different initiation mechanisms. The fatigue performance of each steel is a consequence of the initiation mechanism and is therefore directly related to the nature of the elongated inclusions. Steel C has the best overall fatigue performance because the elongated inclusions in this steel resist fatigue damage the most. In comparison steel D has the poorest fatigue resistance because the elongated inclusions are easily damaged and form fatigue cracks quickly.

Only for steels A and B may the inclusion measurements be used to account for differences in the fatigue performance between the two steels. The is because the same initiation mechanism operates in both steels. Differences in the fatigue performance can be related to the size and the shape of the elongated inclusions. For both the constant mean stress testing and the ramp mean stress testing steel B has a better fatigue performance than steel A for both surface conditions. The overall better fatigue performance of steel B is shown in the S-N curves of Figure 4.9 and Figure 4.10 and by the results of the ramp mean stress testing given in Table 4.13. Before and after the removal of the ineffective inclusions from the statical study the remaining inclusions in steel B are smaller and more circular than the inclusions in Steel A, see Table 4.9. The volume percentage of inclusions is also smaller for steel B than for steel A, see Table 4.3.

Both the size and shape of the inclusions influence the fatigue resistance of the steel. The size of the inclusion will have two effects. First, according to Kung and Fine [65],

larger inclusions are more likely to initiate fatigue cracks because of the higher probability of a slip band impinging on the inclusion. Second, the size and shape of the inclusions influences both the stresses at the ends of the inclusion and the stresses at the resulting cavity that forms when the inclusions becomes separated from the matrix. According to the calculations of Edwards [21] higher stress concentrations result as the inclusion becomes more elongated and larger.

Therefore, a qualitative relationship exists between the size and shape of the inclusions and the fatigue performance of steels A and B. Steel B which has on average smaller and more spherical inclusions has a superior fatigue performance than steel A which has larger more elongated inclusions. Similar relationships between the inclusions size and fatigue performance were reported by Uhrus [14], Duckworth and Ineson [15] and Dekazinczy [16].

5.2.8 Comparison to the Results from Other Investigations

As stated previously the fatigue performance of the four rail steels tested in this investigation contradict the normally observed relationship between fatigue performance and yield strength or hardness. An investigation into the fatigue resistance of rail steels as a function of actual loading history by Leis and Rice [37] noted that the fatigue resistance of a rail is a function of the hardness. The same conclusion was reached by Hiller [73] from the results of an experimental investigation into the bending fatigue strength of pearlitic rail steels. Increasing fatigue resistance with increasing steel hardness is also apparent in the results of Park and Fletcher [42].

The anomalous behaviour of the steels tested for this investigation are the result of the metallurgical cleanliness of these steels and the loading configuration. The metallurgical influence is due to the nature of the inclusions present in each steel. As already discussed, differences in the nature of the elongated inclusions change the crack initiation mechanism and greatly affects the steel's fatigue resistance. This accounts for the poor fatigue

resistance of the head hardened steel D in comparison to the fatigue performance of the plain carbon rail steel C.

Differences in the fatigue performance of each steel are further emphasized by the loading configuration used for these experiments. With the specimens cut transverse to the loading direction and the elongated axis of the inclusions the stress concentration around the inclusions is maximized. For both investigations by Heller [72] and Park and Fletcher [42] the specimens are cut longitudinal to the rail axis so the effects of the elongated inclusions are minimal.

It is because of the results of this investigation are not in agreement with the results of others [72,42] that the important influence due to the nature of the inclusions is fully demonstrated. Even though the microstructure of steel D has been optimized in terms of fatigue resistance this steel's actual fatigue performance is poor because of the presence of easily damaged elongated inclusions. Conversely steel C has the best overall fatigue performance because the elongated inclusions in this steel resist deformation. The fatigue performance is the best even though the microstruture should have the least resistance to crack initiation.

5.3 Application of Acoustic Emission to Crack Detection

The acoustic emission technique proved to be a reliable method of detecting the onset of crack initiation. Careful selection of the window parameter settings, the gain and threshold, eliminates most of the background noise and detects crack growth at its earliest stages, as proven by the photographs shown in Figure 4.21 through to Figure 4.30. The cracks are usually detected very early in the stage II propagation regime, as proven by their perpendicular orientation to the principle tensile stress direction and their short lengths. For example, the etched specimen of steel C, Figure 4.27, is still in its earliest stages of development, individual voids within the ferrite are still evident in Figure 4.27 (b).

For steel D there is a pattern in the acoustic emission profiles as was noted in section 4.4.4. At the beginning of the test the acoustic emission activity is high, followed by a period of low activity and finally a second stage of substantial activity which usually corresponded to the initiation of a fatigue crack. A possible explanation of this behaviour follows.

As discussed by Bassim [53], during low cycle fatigue of steels the curve of acoustic emission total counts versus number of cycles is characterized by three stages. At the beginning of the test an initial softening or hardening results in high acoustic emission activity. The initial increase is followed by a decrease in activity which corresponds to a quasi-stable state. The final increase in activity accompanies crack initiation and propagation.

Three distinct stages were observed for steel D as shown in Figure 4.17. However, the final increase did not always correspond to crack initiation, Figure 4.17 (a) shows three distinct regions but the sample was not cracked. The second increase in the acoustic emission activity may result from changes in the internal deformation mechanisms occurring during cyclic loading. The final stress level shown in Figure 4.17 (b) does have an initial period of low activity followed by a sudden increase which corresponded to crack initiation. An initial but short period of acoustic emission activity is apparent at the high stress levels.

During constant mean stress level testing a final period of increasing acoustic emission activity is superseded by an initial stage of high activity, as shown in Figure 4.19 and Figure 4.20. The combination of the two stages may result from the different stages of crack growth. In Figure 4.20, there is initially a brief period of high activity which may result from internal cracks within a brittle silicate-glass inclusion. The next stage which is characterized by low acoustic emission activity may correspond to crack propagation through a MnS inclusion or be just a period of dormant crack growth. The final stage of high activity results from stable crack growth through the matrix. However, there is no

experimental verification to link these stages of acoustic emission activity to the stages of crack initiation.

The acoustic emission activity for steel C was usually characterized by low activity followed by high activity which corresponded to crack initiation and propagation, see Figure 4.15 (a) and Figure 4.15 (b). For the shot peened specimens occasional erroneous signals would occur, see Figure 4.16 (b). These occasional bursts may result from the early stages of crack growth and possible retardation as the crack tip encounters regions of high compressive stresses.

For all four rail steels tested the crack initiation detection system provided to be reliable and sensitive. Extremely small cracks were usually detected, sometimes as small as 0.01 mm. Therefore, the acoustic emission detection system could capture crack growth in its earliest stages. Subsequent metallographic examination revealed in detail the different crack initiation mechanisms operating in these steels. These observations explained why the fatigue performance of the rail steels is not in agreement with the expected relationship between hardness and fatigue resistance.

Chapter VI

Conclusions

The fatigue performance of four pearlitic rail steels has been investigated. The fatigue performance was evaluated in terms of the number of cycles to crack initiation, which was detected by monitoring the acoustic emission activity during cyclic loading.

Metallographic examinations of tested and etched specimens from each of the rail steels revealed three distinct crack initiation mechanisms. The mechanism operating in each steel was a result of the nature of the inclusions. In all the steels cracks were found to initiate at elongated MnS inclusions and not at circular oxide inclusions. The three different crack initiation mechanisms resulted because of differences in the elongated inclusions from steel to steel.

In steels A and B cracks were found to initiate at elongated MnS inclusions which had become either partially or holly debonded from the matrix. The stress concentration was found to rise when the inclusions were separated from the matrix and this resulted in the initiation of a fatigue crack. The debond seam resulted from the coalescence of initially separated voids along the inclusion/matrix interface. The voids formed by intrusions of ferrite into the inclusions and the accompanying fracture of cementite plates.

The second crack initiation mechanism observed was unique to steel C. In this steel cracks initiate in local deformation bands ahead of elongated inclusions. The elongated inclusions were found to have an inner core of MnS surrounded by Al_2O_3/SiO_2 which resisted the formation of voids in the inclusion/matrix interface. The cracks initiated in a zone of stress concentration and triaxiality ahead of the inclusion. The earliest detected stage of crack initiation was the appearance of voids within the ferrite. The crack grew as the voids coalesced by fracturing the cementite plates.

In the head hardened rail, steel D, cracks initiated within easily damaged brittle silicate inclusions. These inclusions were unable to accommodate the cyclic deformation occurring

within the matrix and became fatigue damaged. The cracks formed within these brittle inclusions either propagated into the matrix or through an accompanying MnS inclusion.

The size and shape of the inclusions, the inclusion/matrix interfacial strength and the elastic modulus of the inclusion relative to the matrix were all important influences on the fatigue performance of the steels. The crack initiation mechanism operating in each steel was a function of the relative importance of each of these factors. The fatigue performance of each steel was determined by the crack initiation mechanism and was therefore directly related to the nature of the inclusions.

Steel D was found to have the poorest fatigue performance because of the presence of brittle inclusions that were easily fatigue damaged. The fatigue performance was found to be poor because of a low endurance limit and a comparatively short fatigue life at higher stress levels. Steel C had the best overall fatigue performance because its inclusions resisted being damaged during cyclic loading. The elongated inclusions in this steel were not brittle enough to be fatigue damaged and had a high interfacial strength that prevented void formation. Steels A and B had a good overall fatigue performance compared to steel D. However, their performance was generally lower than the fatigue performance of steel C because of the voids or intrinsic cracks that formed along the inclusion/matrix interface. A qualitative relationship between the size and shape of the elongated inclusions and the fatigue performance of steels A and B was found to exist. Steel B had a better overall fatigue performance than steel A and had smaller and more circular inclusions.

The beneficial effects of shot peening were most evident at low stress levels near the endurance limit of each steel. Shot peening resulted in an increase in the fatigue endurance limit and in the number of cycles to crack initiation at intermediate stress levels. Fading of the compressive residual stresses at high stress levels was most evident for steel C.

For specimens with either surface condition the difference in the fatigue performance between different steels decreased as the mean stress level increased. As well, the scatter between specimens from the same steel decreases at high stress levels. Similarly there was

close agreement between the three specimens tested for each steel during the ramp mean stress level testing.

The results clearly show that acoustic emission detected crack initiation quickly and reliably. The cracks were usually detected in the earliest stages of crack growth, cracks as small as 0.01 mm were discovered. Such early detection of crack initiation revealed the influence of the inclusions and the details of the crack initiation mechanism.

REFERENCES

1. G.E. Dieter, "Mechanical Metallurgy", 3rd ed., McGraw-Hill Inc., New York, 1986.

2. W.A. Wood, "Fracture", John Wiley & Sons Inc., New York, 1959.

3. M.E. Fine and R.O. Ritchie, "Fatigue and Microstructure", American Society for Metals, Metals Park, Ohio, 1979, p 245.

4. C. Laird, "Fatigue and Microsture", American Society for Metals, Metals Park, Ohio, 1979 p149.

5. G.T. Gray III, A.W. Thompson and J.C. Williams, Metall. Trans. A, 16A (1985) 753.

6. A.R. Rosenfield, G.T. Hahn and J.D. Embury, Metall. Trans., 3 (1972) 2797

7. G.T. Gray III, A.W. Thompson J.C. Williams and D.H. Stone, Cdn. Metall. Quarterly, 21 (1982) 73.

8. B.N. Leis, in R.J. Sanford (ed.), "Fracture Mechanics Fifteenth Symposium", ASTM STP 833, American Society for Testing and Materials, Philadelphia,1962 p.449.

9. M. Atkinson, J. Iron Steel Inst., 195 (1960) 64.

10. P.H. Firth, J. Iron Steel Inst., 180 (1955) 26.

11. N.H. Cummings, F.B. Stulen and W.C. Shulte, Proc. ASTM, 58 (1958) 505.

12. Y. Murakami and T. Endo, Int. J. Fracture, 2 (1980) 23.

13. E. Ineson. J. Clayton-Clave and R.J. Taylor. J. Iron Steel Inst., 190 (1958) 227.

14. L.O. Uhrus, Iron Steel Inst. Sp. Rep., 77 (1963) 104.

15. W.E. Duckworth and E. Ineson. Iron Steel Inst. Sp. Rep., 77 (1963) 87.

16. F. DeKazinczy, J. Iron Steel Inst., 208 (1970) 851.

17. P.A. Thornton, J. Mater. Sci., 6 (1971) 347.

18. J. T. Ransom, Trans. ASM, 46 (1954) 1254.

19. J. Gurland and J. Plateau, Trans. ASM, 56 (1963) 443.

20. L.H. Donnell, in "Theodore Von Karman Anniversary volume" Cal. Inst. Tech., Pasadena, (1941) 293.

21. R.H. Edwards, J. Appl. Mech., 18 (1951) 19.

22. J.N. Goodier, J. Appl. Mech. Trans. ASME, 55A (1953) 39.

23. N.M.A Eid and P.F. Thomason, Acta. Metall., 27 (1979) 1239.

24. J. Lankford and F.N. Kusenberger, Metall. Trans., 4 (1973) 553.

25. Y. Murakami, JSME Int. J., series 1, 32 (1989) 167.

26. J.T. Barnby and F.M. Peace, Acta. Metall., 4 (1973) 1351.

27. G. Harkegard. Int J. Fract., 9 (1973) 437.

28. J. Lankford and F.N. Kusenberger, Metall. Trans., 4 (1973) 553.

29. C.G. Chipperfield, D.G. Skinner and S. Marich, IISI Annual Conf., Melbourne, (1981) 223.

30. H Ghonem and J. Kalousek, Eng. Fract. Mech., 30 (1988) 667.

31. A.F. Bowler and K.J. Johnson in S.L. Grassie (ed.), " Mechanics and Fatigue in Wheel/Rail Contact, Proc. 3rd Int. Conf. Contact Mechanics and Wear of Rail/Wheel Systems, Cambridge, U.K., July 22-26, 1990", Elsevier, Amsterdam, 1990, p.1.

32. R. Clayton, M.B.P. Allery and P.J. Botten, Proc. Int. Symp. Contact Mechanics and Wear of Rail/Wheel Systems 1, Vancouver, B.C., July 1982, University of Waterloo Press, Waterloo, Ontario, 1983, p.419.

33. M.N. Bassim, D. Shun, S. Yannacopoulos, M.R. Bayoumi and M.C. Chatervedi, ASM 85th Int. Conf. Surface Modifications Coatings, Toronto, Canada, American Society of Materials, 1985.

34. T.M. Ravitskaya, Problemy Prochnosti, 11 (1974).

35. H. Ghonem, J. Kalousek, D.H. Stone and E.E. Laufer, Proc. 2nd Int. Heavy Haul Railway Conf., ASME, Colorado Springs, Colorado, September 1982, p.339.

36. G.M. Hamilton, Proc. Inst. Mech. Eng., 197C (1983) 53.

37. B.N. Leis and R.C. Rice, Proc. 2nd Int. Heavy Haul Railway Conf., ASME, Colorado Springs, Colorado, September,1982, p.99.

38. D.H. Stone, Cdn. Metall. Quarterly., 21 (1982) 17.

39. F.B. Fletcher and Y.J. Park, Proc. 2nd Int. Heavy Haul Railway Conf., Colorado Springs, Colorado, September 1982, p.199.

40. N.P. Suh, Wear, 25 (1973) 111.

41. P.M. Fegredo, M.T. Shehata, A. Palmer and J. Kalousek, Proc. 7th Int. Conf. Strength of Metals and Alloys, Pergamon Press, Oxford (1985) p 285.

42. G.J. Fowler and A.S. Tetelman, AREA Proc. vol 79 Bulletin 668 (1979) 447.

43. H. Ghonem and J. Kalousek, Wear, 97 (1984) 65.

44. C.G. Chipperfield and D.H. Skinner, Railway Engineering Conf. (1981), Sydney, Australia, (1981) p.12.

45. R.C. Rice, B.N. Leis and M.E. Tuttle, ASTM special technical publication 776, (1982) 132.

46. J.C.Spanner in H.L. Dunnegan and W.F. Hartman (eds.), "Proc. Int. Conf. on Acoustic Emission", American Society Nondestructive Testing, 1981 p.1.

47. H.N.G. Wadley, C.B. Scruby and J.H. Speake, Int. Met. Review No 2, (1980) 41.

48. R.H. Jones, M.A. Friesel and W.W. Gerberich, Metall. Trans. A, 20A (1989) 637.

49. T.F. Drouillard, Nondestructive Testing Handbook, 2nd edition, vol. 5, Acoustic Emission Testing, 1987, p.12.

50. P. Tschelisnig, Int. J. Mat. Prod. Tech., 3 (1988) 267.

51. A.C.E. Sinclair, D.C. Connors and C.L. Formby, Mat. Sci. Eng., 28 (1977) 263.

52. M.N. Bassim,Nondestructive Testing Handbook, 2nd edition, vol. 5, Acoustic Emission Testing, 1987, p.46.

53. M.N. Bassim, J. Acoustic Emission, 4 (1985) s224.

54. M.N. Bassim in K. Yamaguchi, K. Aoki and T. Kishi (eds.), "Progress in Acoustic Emission III, Proc. 8th Int. Acoustic Emission Sym., Tokyo, Japan, October 1986",1986, p.226.

55. I.G. Palmer and P.T. Heald, Mat. Sci. Eng., 11 (1973) 181.

56. H.L. Dunegan, D.O. Harris and C.A. Tatro, Eng. Fract. Mech., 1 (1986) 105.

57. J. Masounave, J. Lanteigne, M.N. Bassim and R. Hay, Eng. Fract. Mech., 8 (1976) 701.

58. H.L. Morton, R.M. Harrington and J.G. Bjeletich, Eng. Fract. Mech., 5 (1973) 691.

59. T.C. Lindley, I.G. Palmer and C.E. Richards, Mat. Sci. Eng., 32 (1978) 1.

60. R.V. Williams, "Acoustic Emission", Adam Hilger Ltd., Bristol,1980.

61. C.W. Corti, P. Cotterill and G.A. Fitzpatrick, Int. Metall. Rev., 19 (1974) 77.

62. G.F Vandervoort, "Metallography: Principles and Practice", McGraw-Hill, New York, (1984), Chapter 6.

62. L.E. Samuels, "Optical Microscopy of Carbon Steels", American Society for Metals, Metals Park, Ohio, (1990).

64. D. Brooksbank and K.W. Andrews, J. Iron Steel Inst, 210 (1972) 246.

65. C.Y. Kung and M.E. Fine, Metall. Trans. A, 10A (1979) 603.

66. G.J. Fowler and A.S. Tetelman,in D.H. Stone and G.G. Knupp (eds.), "Rail Steels-Developments and Use, Denver, Colorado, November 17-18 1976", ASTM STP 664, American Society for Testing and Materials, 1978, p.363

67. J.J. Scutti, R.M. Pelloux and R. Fuquen-Moleno, Fatigue Eng. Mat. Struct., 7 (1984) 121.

68. L.E. Miller and G.C. Smith, J. Iron Steel Inst., 208 (1970) 998.

69. F.B. Stulen. Proc. Sym. Fatigue Aircraft Struct.,Wright Patterson Air Force Base, Ohio, 1959, p.644

70. J.M. Barsom and E.J. Imhof, ASTM special technical publications 121, (1952) 387.

71. D.H. Breen and E.M. Wene, in, "Fatigue and Microstructure, ASM Materials Science Seminar, St. Louis, Missouri, October 14-15 1978", American Society for Metals, Metals Park, Ohio, 1979 p.57.

72. W. Heller, R. Schweitzer and L. Weber, Cdn. Metall. Quat., 21 (1981) 3.

73. E. Epremian and R.F. Mehl, ASTM STP 137, American Society for Testing and Materials, (1953).

74. B.N. Leis, in D.H. Stone and G.G. Knupp (eds.)., "Rail Steels-Developments and Use, Denver, Colorado, November 17-18 1976", ASTM STP 664, American Society for Testing and Materials,1978, p.449